

APR

REPORT DOCUMENTATION PAGE

AFRL-SR-BL-TR-01-

0320

Public reporting burden for this collection of information is estimated to average 1 hour per response, including the time for reviewing instructions, gathering existing data needed, and completing and reviewing this collection of information. Send comments regarding this burden estimate or any other aspect of this collection of information, including suggestions for reducing this burden, to Washington Headquarters Services, Directorate for Information Operations and Reports (0704-0188), 1215 Jefferson Davis Highway, Suite 1204, Arlington, VA 22202-4302, and to the Office of Management and Budget, Paperwork Project Director (0704-0188), 1215 Jefferson Davis Highway, Suite 1204, Arlington, VA 22202-4302. Respondents should be aware that notwithstanding any other provision of law, no person shall be subject to any penalty for failing to comply with a collection of information if it does not have a unique identifier (OMB control number). **PLEASE DO NOT RETURN YOUR FORM TO THE ABOVE ADDRESS.**

1. REPORT DATE (DD-MM-YYYY) 3/31/2001		2. REPORT TYPE Final Technical Report		3. DATES COVERED 8/15/1997 - 12/31/2001	
4. TITLE AND SUBTITLE MEMS-Based Control for Air-Breathing Propulsion				5a. CONTRACT NUMBER	
				5b. GRANT NUMBER F49620-97-1-0526	
				5c. PROGRAM ELEMENT NUMBER	
6. AUTHOR(S) Choon S. Tan, Ph.D, Professor Kenneth Breuer, Professor Thomas Corke, Mr. Jin-Woo Bae Eugene Kang, Ph.D., and Robert Bayt, Ph.D.				5d. PROJECT NUMBER	
				5e. TASK NUMBER	
				5f. WORK UNIT NUMBER	
7. PERFORMING ORGANIZATION NAME(S) AND ADDRESS(ES) Massachusetts Institute of Technology Gas Turbine Lab, 31-267 77 Massachusetts Avenue Cambridge, MA 02139-4307				8. PERFORMING ORGANIZATION REPORT NUMBER	
9. SPONSORING / MONITORING AGENCY NAME(S) AND ADDRESS(ES) AFOSR/NA 801 North Randolph Street Rm 732 Arlington, VA 22203-1977				10. SPONSOR/MONITOR'S ACRONYM(S)	
				11. SPONSOR/MONITOR'S REPORT NUMBER(S)	
12. DISTRIBUTION / AVAILABILITY STATEMENT unlimited					
13. SUPPLEMENTARY NOTES					
14. ABSTRACT This document constitutes a final report on a research program entitled, "MEMS-Based Control for Air-Breathing Propulsion." The overall goal of the program was to demonstrate the active flow control in two areas that could result in improved performance of air-breathing propulsion technologies: tip leakage flows and external jet control.					
15. SUBJECT TERMS air breathing propulsion, MEMS, tip clearance flow, external jet flow					
16. SECURITY CLASSIFICATION OF:			17. LIMITATION OF ABSTRACT	18. NUMBER OF PAGES	19a. NAME OF RESPONSIBLE PERSON Choon S. Tan, P.I.
a. REPORT	b. ABSTRACT	c. THIS PAGE			19b. TELEPHONE NUMBER (include area code) 617-253-7524

*Gas Turbine Laboratory
Department of Aeronautics and Astronautics
Massachusetts Institute of Technology
Cambridge, MA 02139*

A Final Report for
DARPA/AFOSR Grant F49620-97-1-0526

entitled

MEMS-Based Control for Air-Breathing Propulsion

submitted to

Air Force Aerospace Research - OSR
801 North Randolph St., Rm. 732
Arlington, VA 22203-1977

Dr. T. Beutner (AFOSR) and Dr. W. Tang (DARPA)
Contract Monitors

PRINCIPAL
INVESTIGATOR:

Choon S. Tan
Department of Aeronautics and Astronautics
Massachusetts Institute of Technology, Cambridge, MA 02139

CO-INVESTIGATORS:

Kenneth Breuer
Division of Engineering
Brown University, Providence, RI 02912

Thomas Corke
Aerospace and Mechanical Engineering Department
University of Notre Dame, Notre Dame, IN 46556-5684

RESEARCH
ASSISTANTS:

Jinwoo Bae, Eugene Kang, Robert Bayt

March 2001

20010508 101

Overall Summary

This document constitutes a final report on a research program entitled "MEMS-based Control for Air-Breathing Propulsion". The overall goal of the program was to demonstrate the active flow control in two areas that could result in improved performance of air-breathing propulsion technologies: tip leakage flows and external jet control. The tip leakage flows are being explored in a research program based at MIT, while the external jet control is based at Illinois Institute of Technology/University of Notre Dame under the direction of T. Corke. As originally proposed, the two programs are linked by a common use of MEMS technologies for sensors and actuators. Although funded as a single grant, the two programs are functionally and administratively distinct (Illinois Institute of Technology/University of Notre Dame is funded via a subcontract from MIT). While progress was made in the characterization of the active control of compressor tip leakage flow based on the use of synthetic actuator jet/directed synthetic jet and the associated flow processes, no use was made of MEMS-based actuators. For this reason this report is presented as three parts one following the other: the first will be on active control of compressor tip leakage flow, the second will be on measurement of shear stress and temperature using MEMS fabricated sensors, and the third on plasma discharge actuators and their use in external jet control.

Overall Contents

Part I: Active Control of Tip Clearance Flow in Axial Compressors

Part II: Measurement of Shear Stress and Temperature Using MEMS Fabricated Sensors

Part III: External Jet Control

PART I
Active Control of Tip Clearance Flow in Axial Compressors

Jinwoo Bae
MIT Gas Turbine Laboratory

Abstract

Compressor tip clearance flow control schemes are explored using the following types of fluidic actuators: Normal Synthetic Jet (NSJ), Directed Synthetic Jet (DSJ) and Steady Directed Jet (SDJ). These jet actuators are mounted on the casing wall to affect the flow in the endwall region. Measurements show that use of such actuators can lead to change in one or more the following measures that characterize the overall behavior of tip clearance flow: (1) reduction of tip leakage flow rate, (2) mixing enhancement between tip leakage flow and core flow, and (3) increase in streamwise momentum of the flow in the endwall region.

The blockage reduction associated with the use of NSJ is sensitive to the forcing frequency and its pitchwise location, and it is accompanied by an increase in loss. By contrast the use of DSJ and SDJ leads to a reduction in endwall blockage and loss that is relatively insensitive to the forcing frequency. To identify the flow process/processes responsible for the observed sensitivity, time-resolved measurements have been taken without actuation in the endwall region. The measurements show identifiable distinct frequency that appears to scale with the far upstream velocity and blade chord rather than tip clearance size.

To explain the observed frequency, a model-based approach is used. The tip clearance vortex and its image vortex associated with the casing wall form a pair of counter-rotating vortices similar to the trailing vortices downstream of airplane wing. This analogy allows application of the Crow instability theory to determine the most unstable wavelength given the radius of the vortex core and the separation distance between the two vortices. Scaling arguments based on the use of Crow analysis and Rains model of tip leakage vortex core suggest that the most unstable frequency appears to correspond to the observed frequency. The time scale characterizing the instability is shown to be of the order of convective time through the blade passage. It is thus *hypothesized* that the tip clearance flow is most receptive to forcing at a frequency corresponding to the most unstable disturbance associated with the tip leakage vortex.

Contents

List of Figures	7
List of Tables	11
Nomenclature	12
1 Introduction	15
1.1 Background	15
1.2 Technical Objectives	16
1.3 Approach	16
1.4 Organization of Report	16
References	16
2 Experimental Setup	18
2.1 Introduction	18
2.2 Linear Cascade Wind Tunnel	19
2.2.1 Test Section	19
2.2.2 Instrumentations	20
2.2.3 Flow Visualization	21
2.3 Actuator	22
2.3.1 Actuator Design and Fabrication	22
2.3.2 Actuator Performance Characterization	25
References	29
3 Baseline Performance	31
3.1 Effect of Reynolds number	31
3.2 Flow Near Mid-span	32
3.3 Survey of Total Pressure Loss Coefficient	33
3.4 Effect of Tip Clearance Size on Performance	34
3.5 Effect Of Blade-To-Blade Non-Periodicity On Endwall Blockage	37
References	38
4 Time-Average Effects of Actuation	40
4.1 Normal Synthetic Jet Actuator	40
4.1.1 Scaling of NSJ Actuator Amplitude	41
4.1.2 Dependence on Forcing Frequency of NSJ	43
4.1.3 Dependence on Pitchwise Location of NSJ	45
4.1.4 Contribution of Each NSJ Actuator	47

4.1.5	Flow Visualization.....	47
4.1.6	Bulk Flow Process Associated with NSJ Actuation	49
4.2	Directed Synthetic Jet Actuator	50
4.2.1	Dependence on Amplitude of DSJ	51
4.2.2	Dependence on Forcing Frequency of DSJ	52
4.2.3	Dependence on Pitchwise Location of DSJ.....	53
4.2.4	Contribution of Each DSJ Actuator.....	53
4.2.5	Comparison between DSJ and SDJ	54
4.2.6	Return on Actuator Flow Power.....	55
4.3	Summary.....	57
	References	58
5	Unsteadiness in Tip Clearance Vortex	60
5.1	Introduction.....	60
5.2	Time-resolved Measurements.....	60
5.3	Vortex Instability	62
5.4	Application to Tip Clearance Vortex	64
5.5	Unsteadiness at Various Axial Locations	70
5.6	Summary.....	71
	References	72
6	Overall Summary and Conclusions.....	73

List of Figures

Figure 2.1	Effect of tip clearance on endwall flow structure. Trailing edge total pressure loss coefficient ω contours of cantilevered stator with (a) moving wall, skewed boundary layer, and clearance; (b) stationary wall, skewed boundary layer, and clearance; (c) stationary wall, collateral boundary layer, and clearance; (d) stationary wall, collateral boundary layer, and no clearance. CFD simulation (Khaïd [2.5]).	18
Figure 2.2	Schematic of cascade wind tunnel test section.	20
Figure 2.3	Schematic of synthetic jet actuator used in cascade rig. Configuration of Normal Synthetic Jet actuator with slit.	23
Figure 2.4	Schematic of DSJ actuator mounted on casing wall.	24
Figure 2.5	Schematic of Directed Synthetic Jet (DSJ) actuator mounted on casing wall showing the direction of the jet.	24
Figure 2.6	Amplitude/frequency response of NSJ actuator: (a) comparing pre- and post-calibration on linear scale abscissa; (b) calibration taken over larger frequency range shown on log scale abscissa. Actuator slit size $d = 0.25\text{mm}$. V_{pp} is peak-to-peak driving voltage. Data of two different membranes.	26
Figure 2.7	Comparison between measured and simulated impulse responses of voice coil and membrane system.	27
Figure 2.8	Amplitude/frequency response of DSJ actuator.	28
Figure 2.9	Time-trace of DSJ: (a) velocity; (b) momentum. Ensemble-average of 20 cycles.	28
Figure 2.10	Calibration of Steady Directed Jet (SDJ) actuator.	29
Figure 3.1	Contours of total pressure loss coefficient with various Reynolds numbers. 3%C tip clearance.	32
Figure 3.2	Reynolds number dependence and critical Reynolds number.	32
Figure 3.3	Mid-span C_p distribution. Comparison between measurements on center blade and CFD prediction using MISES [3.1].	33
Figure 3.4	Contours of total pressure loss coefficient, ω measured 5%C downstream of trailing edge plane.	34
Figure 3.5	Endwall blockage measured 5%C downstream of trailing edge plane vs. tip clearance size.	35
Figure 3.6	Static pressure measured 5%C downstream of trailing edge plane using six pressure taps on endwall.	36
Figure 3.7	Mass-average endwall total pressure loss coefficient vs. tip clearance size.	36
Figure 3.8	Stream thrust-average total pressure loss coefficient vs. tip clearance size.	37

Figure 3.9	Measurements with non-periodic tip clearances compared with measurements with uniform tip clearances: (a) endwall blockage; (b) mass-average endwall loss.	38
Figure 4.1	Contours of ω measured 5% C downstream of T.E. plane: (a) baseline without actuation, $\tau = 3\%C$; (b) NSJ directly over blade tip (0% pitch), $C_{\mu \tau} = 0.88$, $F_C^- = 1.0$; (c) NSJ over vortex core (25% pitch), $C_{\mu \tau} = 0.88$, $F_C^- = 1.0$. Arrows indicate locations of NSJ slits.	40
Figure 4.2	Exit static pressure with and without NSJ actuation. \square : NSJ directly over blade tip (0% pitch), $C_{\mu \tau} = 0.88$, $F_C^- = 1.0$; \triangleleft : NSJ over vortex core (25% pitch), $C_{\mu \tau} = 0.88$, $F_C^- = 1.0$.	41
Figure 4.3	Magnitude of leakage jet velocity leaving tip clearance.	42
Figure 4.4	Tip clearance-related blockage vs. NSJ actuator amplitude. Actuator near vortex core. $F_C^- = 1.0$.	42
Figure 4.5	Contours of ω measured 5% C downstream of T.E. plane: (a) baseline without actuation, $\tau = 2\%C$; (b) NSJ over vortex core (25% pitch), $C_{\mu \tau} = 0.44$, $F_C^- = 1.0$; (c) NSJ over vortex core, $C_{\mu \tau} = 1.32$, $F_C^- = 1.0$.	43
Figure 4.6	Endwall blockage vs. $C_{\mu \tau}$ of NSJ directly over blade tip. Data sets taken for two upstream velocities. $\tau = 3\%C$, $F_C^- = 1.0$.	43
Figure 4.7	Frequency dependence of blockage reduction with NSJ actuator over vortex core: (a) using clearance size τ , (b) using blade chord C as length scale.	44
Figure 4.8	Frequency dependence of blockage reduction with NSJ actuator over blade tip: (a) using clearance size τ , (b) using blade chord C as length scale.	45
Figure 4.9	Endwall blockage vs. pitchwise location of NSJ actuator. $C_{\mu \tau} = 0.88$ and $F_C^- = 1.0$.	46
Figure 4.10	Endwall total pressure loss coefficient vs. pitchwise location of NSJ actuator: (a) mass-average ω ; (b) stream thrust-average (or fully mixed-out) ω .	46
Figure 4.11	Contribution of each NSJ actuator placed directly over blade tip. All data taken at $F_C^- = 1.0$.	47
Figure 4.12	Images from flow visualization and computer-processed intensity contour lines: (a) baseline without actuation ($\tau = 3\%C$); (b) with NSJ actuation over blade tip ($F_C^- = 1.0$ and $C_{\mu \tau} = 0.88$).	48
Figure 4.13	Average magnitude of gradients of intensity in flow visualization images indicating mixing level.	49
Figure 4.14	Contours of ω measured 5% C downstream of T.E. plane: (a) baseline without actuation, $\tau = 3\%C$; (b) DSJ directly over blade PS (-0.04 pitch), $C_{\mu \tau} = 0.88$, $F_C^- = 1.0$. Arrows indicate locations of DSJ holes.	51
Figure 4.15	Exit static pressure with and without NSJ actuation. \triangleleft : DSJ directly over blade PS (-0.04 pitch), $C_{\mu \tau} = 0.88$, $F_C^- = 1.0$.	51

Figure 4.16 Comparison between DSJ (placed near pressure surface of blade) and NSJ (placed near vortex core). $\tau = 3\%C$. Both actuators at $F_c^- = 1.0$.	52
Figure 4.17 Frequency dependence of blockage reduction with DSJ over pressure surface of blade. $\tau = 3\%C$.	52
Figure 4.18 Endwall blockage vs. pitchwise location of DSJ actuator.	53
Figure 4.19 Endwall total pressure loss coefficient vs. pitchwise location of DSJ actuator: (a) mass-average ω (b) stream thrust-average (or fully mixed-out) ω .	53
Figure 4.20 Contribution of each DSJ actuator placed over blade PS. $F_c^- = 1.0$.	54
Figure 4.21 Comparison between DSJ and SDJ (Steady Directed Jet). Holes of both actuators placed over pressure surface of blade. $\tau = 3\%C$. DSJ at $F_c^- = 1.0$.	55
Figure 4.22 Return on injected flow power of directed jet actuation at $\bar{C}_{\mu,\tau} = 0.25$.	56
Figure 4.23 Predicted return on actuator input: (a) as function of relative angle between jet and main flow; (b) as function of velocity ratio for fixed momentum injection.	57
Figure 5.1 Frequency contents of velocity measured with hot-wire sensor placed $5\%C$ downstream of blade exit plane between center of vortex core and casing wall. Data taken without actuation.	61
Figure 5.2 Forced response measured $5\%C$ downstream of T.E. plane with NSJ over blade tip. $C_{\mu,\tau} = 0.88$.	62
Figure 5.3 Instability of trailing vortices visualized by smoke [5.2]. View from chase airplane.	62
Figure 5.4 Schematic of trailing vortex instability.	63
Figure 5.5 Dissipation time vs. forcing frequency of trailing vortices in flight test (data from Chevalier [5.2]).	64
Figure 5.6 Schematic of tip clearance vortex and its image against casing wall creating a pair of counter-rotating vortices similar to trailing vortices.	64
Figure 5.7 Tip clearance vortex core estimated using Rains [5.4] model and location of maximum loss coefficient. Total pressure loss coefficient contour measured near T.E. plane.	66
Figure 5.8 Amplification rate vs. wave number for $R_c/b = 0.36$.	67
Figure 5.9 Most unstable wave number β_{max} predicted for fixed R_c/b .	67
Figure 5.10 Contour plot of most rapidly growing wavelength λ/C as function of vortex core radius and separation distance. Symbols are estimations for three tip clearance sizes as labeled.	68
Figure 5.11 Comparison between measured frequency content and predicted frequency.	68
Figure 5.12 Vortex core radius R_c and separation distance b for two blade chord lengths. Both with $3\%C$ clearance.	69
Figure 5.13 Dimensional frequency vs. reduced frequency using blade chord length.	69

Figure 5.14 Variations along chord: (a) variations in R_t/C and b/C as function of x/C ; (b) most unstable frequency F_c^- predicted using local approximations.....	70
Figure 5.15 Time-resolved measurements at various axial locations: (a) locations of hot-wire sensor; (b) power spectral density at each location.....	71
Figure 16 Schematic of Thermal Shear sensor/temperature sensor design. The sensor element is mounted on a thin membrane, which covers a vacuum cavity.....	77
Figure 17: Shear Stress and Temperature Sensor Process Flow.	78
Figure 18. Optical Microscope photo of shear stress sensors. The white line is the exposed platinum of the sensing resistor due to the gold being etched away. The light colored circle is the 1500-Å nitride membrane over the vacuum cavity. The left frame shows a single sensor while the right frame shows an array of three two-dimensional sensors, each of which enable a directional measurement of shear.....	80
Figure 19. Optical micrograph of a fabricated temperature sensor. The sensing resistor (10 microns wide) is oriented horizontally. The two leads from the bottom supply a small (fixed) current. The leads above are at a floating potential and used to measure voltage drop across the sensor resistor which changes as the sensor resistance changes with temperature.....	81
Figure 20: Voltage-Current behavior of hotwire sensors (5 μm x 100 μm long) sensor on a vacuum cavity. The positive curvature indicates self-heating due to Ohmic losses.....	81
Figure 21: Infrared image of sensor operating at 336 milliVolts and 7 milliamps in still air, which represents a resistive overheat of 1.4. The image indicates that the sensor becomes much hotter than the surrounding substrate, and there is no perceptible temperature rise in the leads.....	82
Figure 22: Power spectrum of Shear Sensor measured in a fully turbulent boundary layer. Note t' - high signal-to-noise ratio achieved and the good frequency response of the sensor.....	83

List of Tables

Table 2.1	Summary of cascade design parameters.....	20
Table 2.2	Dimensions of synthetic jet actuator.	25
Table 4.1	Effects of each flow process and their combined effects on tip clearance-related blockage and loss explaining observations with NSJ actuator over blade tip.	50

Nomenclature

Symbols

A_b	Blocked area due to blockage
$A_{b,2D}$	Blocked area related to boundary layers on blade surfaces
$A_{b,ew}$	Endwall blocked area
$A_{b,tip}$	Tip clearance-related blocked area
A_{ex}	Blade passage exit area = $h \times s$
C	Blade chord
C_D	Discharge coefficient = $Q / (A \sqrt{2 \Delta P / \rho})$
C_P	Static pressure coefficient = $(P - P_\infty) / q_\infty$
f	Frequency (Hz)
h	Span (blade height)
I	Intensity of smoke image in gray scale (white = 0, black = 1 in images)
L	Effective acoustic length of neck in actuator
Q	Flow rate = AU
q_∞	Far upstream reference dynamic head = $0.5 \rho U_\infty^2$
Re_C	Reynolds number = $U_\infty C / \nu$
s	Pitch (spacing between blades)
U	Flow velocity
U_a	Axial flow velocity
$U_{a, edge}$	Edge axial flow velocity
U_L	Core leakage velocity leaving clearance gap
U_J	Center velocity of actuator jet leaving actuator slit (or hole)
$U_{J, peak}$	Peak center velocity of synthetic jet leaving actuator slit (or hole)
U_∞	Reference flow velocity far upstream
V_{pp}	Peak-to-peak voltage
β_{in}	Cascade inlet flow angle
β_{ex}	Cascade exit flow angle
β_r	Reduced frequency = $2\pi f \tau U_L$ or $2\pi f \tau U_\infty$ (in cascade)
F_C^*	Reduced frequency = fC / U_∞ (in cascade)
d	Actuator slit size

θ	Momentum thickness of shear layer
$C_{\mu, \tau}$	Momentum coefficient = $(\rho U_j^2 \delta) / (\rho U_\infty^2 \tau)$ or $(\rho U_{j, peak}^2 A_j) / (\rho U_\infty^2 \tau C)$ (in cascade)
$\overline{C}_{\mu, \tau}$	Time-average momentum coefficient = $\overline{(\rho U_j^2 A_j)} / (\rho U_\infty^2 \tau C)$ (in cascade)
τ	Tip clearance size
ω	Total pressure loss coefficient = $(P_{t, \infty} - P_t) / q_\infty$
$\overline{\omega}_{en}^m$	Mass-average endwall total pressure loss coefficient
$\overline{\omega}_{en}^s$	Stream thrust-average endwall total pressure loss coefficient
X_0	Baseline quantity of X (usually means case without actuation)
\mathcal{E}	EMF
B	Magnitude of magnetic field
L	Total length of coil
v	Velocity of coil assembly
ω_n	Natural frequency (rad/sec)
f_n	Natural frequency (Hz)
f_H	Helmholtz frequency (Hz)
Q	Quality factor = $1/(2\zeta)$
ζ	Damping ratio
K	Constant
A_{neck}	Effective neck area
L_{neck}	Effective neck length
V_{cavity}	Volume of cavity
a	Speed of sound
A_j	Jet area
t	Time (sec)
T	Period (sec)
P_t	Total pressure
$P_{t, \infty}$	Far upstream reference total pressure
x	Axial location from L.E. plane
χ	Chordwise location from L.E. plane
y	Pitchwise location
U_x	Axial velocity
$U_{x, edge}$	Edge axial velocity

δ^*	Displacement thickness
$C_{p, ex}$	Exit static pressure coefficient measured 5%C downstream of T.E. plane
Π	Flow power
η_J	Return on Actuator Flow Power Input

Acronyms

I.D.	Inner Diameter
O.D.	Outer Diameter
CFD	Computational Fluid Dynamics
NSJ	Normal Synthetic Jet
DSJ	Directed Synthetic Jet
SDJ	Steady Directed Jet
L.E.	Leading Edge of blade
T.E.	Trailing Edge of blade
SLPM	Standard Liters Per Minute
FS	Full Scale
PS	Pressure Surface (or Side)
SS	Suction Surface (or Side)

1 Introduction

1.1 Background

The finiteness of compressor tip clearance causes a leakage of gas across the blade tip from the pressure surface to the suction surface; this tip leakage flow interacts with the primary gas stream as well as the wall boundary layer. The tip leakage flow dominates the aerothermodynamic behavior of endwall flow and the blade-to-blade flow in the tip regions; as such it has a strong impact on pressure rise capability, compressor efficiency and stability. The influence of tip leakage flow manifests itself in two manners: one in terms of fluid dynamic blockage that effectively reduces the flow area and the other a thermodynamic effect in that the work done in the tip region is different than that in the free stream. Measurements from a low speed multistage compressor (Smith [1.1]) showed that when the tip clearance was increased from the baseline value of 1.38 to 2.8 per cent of span, the peak efficiency reduced by 1.5 point (and the peak pressure rise by 9.7 percent) and the operability range reduced from 17.5 to 9.7 percent (a reduction in stall margin). Likewise from measurements in high speed multistage compressor (Cumpsty [1.2]), not only do the efficiency and pressure ratio deteriorate with increased tip clearance (it should be noted that the loss/gain in efficiency is not monotonic with increase/decrease in tip clearance; for tip clearance below a threshold value, the efficiency can deteriorate), the surge line moves considerably to the right so that the compressor would surge at higher mass flows. All these measured effects are highly detrimental to the operability of compressor. Furthermore in multistage compressor environment changes in tip clearance would generate additional blockage and loss, say in the front stage; this would alter the matching of the downstream stages. Likewise the alteration in the performance of a specific stage due to changes in tip clearance could influence the aerodynamic matching with the upstream stage.

Compressors often operate with tip clearances that are larger than aerodynamically desirable due to changes in tip clearance during operations and limitations in manufacturing tolerances. Consequently, there is a strong motivation to look for means to relieve the stringent requirement on tight tip clearance. Thus of engineering interest is the development of effective means of managing compressor tip clearance flow to: (i) minimize its impact on performance, (ii) desensitize compressor performance to tip clearance changes, or (iii) improve compressor performance. A potential technique for accomplishing either one or two of these is active tip clearance flow control. This report describes a research program that explores the use of fluidic actuators and their characterization to affect the behavior of the tip clearance flow to benefit the compressor performance.

1.2 Technical Objectives

The overall goal is to demonstrate the use of fluidic actuators to implement active tip leakage flow control to result in improved compressor performance. The specific objectives are:

- (1) Identify aspects of tip clearance flow that can be leveraged upon through active flow control to benefit compressor performance.
- (2) Design, develop and characterize the actuators to provide the desired actuations on tip leakage flow.
- (3) Demonstrate the effectiveness of actuators developed in (2) to control tip leakage flow in a low speed compressor cascade rig.
- (4) Identify and characterize the change in flow process/processes due to actuations on tip clearance flow.

1.3 Approach

The approach mainly consists of designing and implementing experimental investigations in the MIT Gas Turbine Laboratory Low-Speed Cascade Rig Facility. Two sets of experiments have been implemented: the first is baseline experiments for delineating the flow features and performance on the compressor cascade rig with tip clearance changes but no flow control; the second set is experiments with the use of flow control using three different types of flow actuators. The three types of actuators used were Normal Synthetic Jet (NSJ), Directed Synthetic Jet (DSJ) and Steady Directed Jet (SDJ). Data consists of flow visualizations using smoke and measurements using pressure as well as hot wire probes. Computations using standard flow solvers and flow modeling are used to help in the design of experiments and interpretation of experimental measurements and observations.

1.4 Organization of Report

This part of the report is arranged as follows: we first describe the experimental setup followed by a delineation of the baseline performance of the cascade tunnel. Experimental results to elucidate the time-average effects of the synthetic jets and their effectiveness on the behavior of the tip clearance flow are presented next. We then discuss the unsteady measurements and the development of a hypothetical flow model to explain the observed flow unsteadiness in compressor tip leakage flow. We end this part of the report with a section on summary and conclusions.

References

- [1.1] Smith, L. H., Jr., "The Effect of Tip Clearance on the Peak Pressure Rise of Axial-flow Fans and Compressors", ASME Symposium on Stall, 1958, pp.149-152.
- [1.2] Cumpsty, N. A., "Compressor Aerodynamics", Longman Group 1989.

- [1.3] Koch, C. C., "Stalling Pressure Rise Capability of Axial Flow Compressors", ASME J. Eng. Power, 1981, vol.103, pp.645-656.
- [1.4] Wisler, D. C., "Loss Reduction in Axial-flow Compressors Through Low-speed Model Testing", ASME J. Eng. Gas Turbines and Power, 1985, vol.107, pp.354-363
- [1.5] Khalid, S. A., "The Effects of Tip Clearance on Axial Compressor Pressure Rise", Ph.D. thesis, MIT, February 1995.
- [1.6] Storer, J. A. and Cumpsty, N. A., "An Approximate Analysis and Prediction Method for Tip Clearance Loss in Axial Compressors", ASME Paper, 93-GT-140.

2 Experimental Setup

2.1 Introduction

To investigate the effect of the proposed actuation schemes on the tip clearance flow in axial compressors, a linear cascade has been designed and fabricated in a low-speed wind tunnel at MIT. Because of the cost-effectiveness and experimental simplicity versus rotating rigs, cascade tunnels have been used by many investigators to study tip clearance flows (Storer and Cumpsty [2.1], Heyes *et al.* [2.2], Bindon [2.3], and Saathoff and Stark [2.4]). Khalid [2.5] pointed out the dominant role of the tip clearance on endwall flow structure by using a computational method eliminating different physical effects one at a time as shown in Figure 2.1(a) – (d). The relative motion of the casing wall or the endwall boundary layer skew results in minor changes in the endwall flow field. The major elements are the loaded blades with tip clearances. Thus the use of a linear compressor cascade rig for investigating the

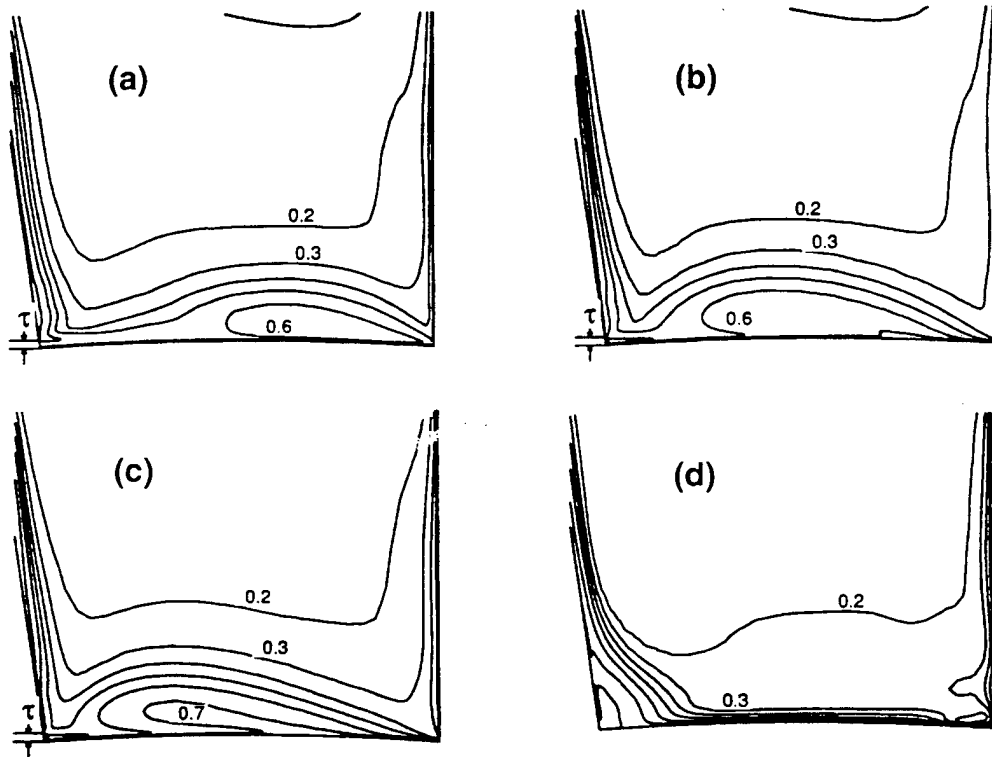


Figure 2.1 Effect of tip clearance on endwall flow structure. Trailing edge total pressure loss coefficient ω contours of cantilevered stator with (a) moving wall, skewed boundary layer, and clearance; (b) stationary wall, skewed boundary layer, and clearance; (c) stationary wall, collateral boundary layer, and clearance; (d) stationary wall, collateral boundary layer, and no clearance. CFD simulation (Khalid [2.5]).

response of tip leakage flow to various actuations can be reasonably justified before considering the use of rotating rig. In this section we describe the MIT Gas Turbine Laboratory linear cascade facility and its modification for experiments that are designed to assess the utility and effectiveness of actuating the tip clearance flow based on NSJ, DSJ and SDJ.

2.2 Linear Cascade Wind Tunnel

2.2.1 Test Section

Table 2.1 summarizes the design parameters of the cascade test section. The design is intended to be representative of a moderately loaded rotor tip section in a modern aero-engine compressor. The schematic of the cascade test section is shown in Figure 2.2. The inlet of the test section is attached to a $0.30\text{m} \times 0.30\text{m}$ contraction exit of a wooden wind tunnel settling chamber. The walls of the test section are made out of 9.5mm thick Plexiglass®. Five slots of the blade contour are cut on the bottom wall, where the roots of the blades are, using a numerically controlled water jet machine. The blades are inserted into the test section from the bottom and held by brackets that are underneath the bottom wall. Blades are cast out of epoxy in a numerically machined aluminum mold for two reasons: to produce blades with identical shape and to embed hypodermic tubes (with O.D. 0.90mm and I.D. 0.66mm) in them for blade surface static pressure measurements. Two blades are instrumented with 14 static pressure taps each, one at mid-span and the other near tip ($1.5\%C$ from the blade tip). All the blades are interchangeable and three central blades in the test section are cantilevered at the roots to allow variable tip clearances. A 7mm wide transition strip made out of 50-grit sandpaper is glued on the suction surface of each blade at $42\%C$ from the leading edge to operate at low wind speed without laminar separation as will be discussed in section 3.1. The outlet screen pressurizes the test section eliminating the need for a suction pump to remove wall boundary layers. With the pressurized test section, boundary layers are bled to the atmospheric pressure through slots. There are bleed slots on the top and bottom walls near the inlet of the test section shown in the schematic to get fresh endwall boundary layers. The periodicity is achieved by adjusting the bleed ports on the sidewalls. The jet actuator is attached to the endwall as shown in Figure 2.2 and sits in a slot machined through the casing wall. The detailed description of the jet actuator is given in section 2.3. The angle of the two exit sidewalls downstream of the blades is set by the mid-span exit flow angle as obtained from MISES [2.6], which has been widely used for analyzing flow in cascade as well as for designing cascade blade sections.

Table 2.1 Summary of cascade design parameters.

Airfoil	G.E. E ³ rotor B tip section
Chord, C	0.190m
Pitch, s	0.177m
Span, h	0.305m
Camber	30.7°
Stagger	56.9°
Reynolds number	$\geq 1.0 \times 10^5$
Inlet flow angle, β_{in}	62.7°
Exit flow angle, β_{ex}	51.8°
Diffusion factor	0.40

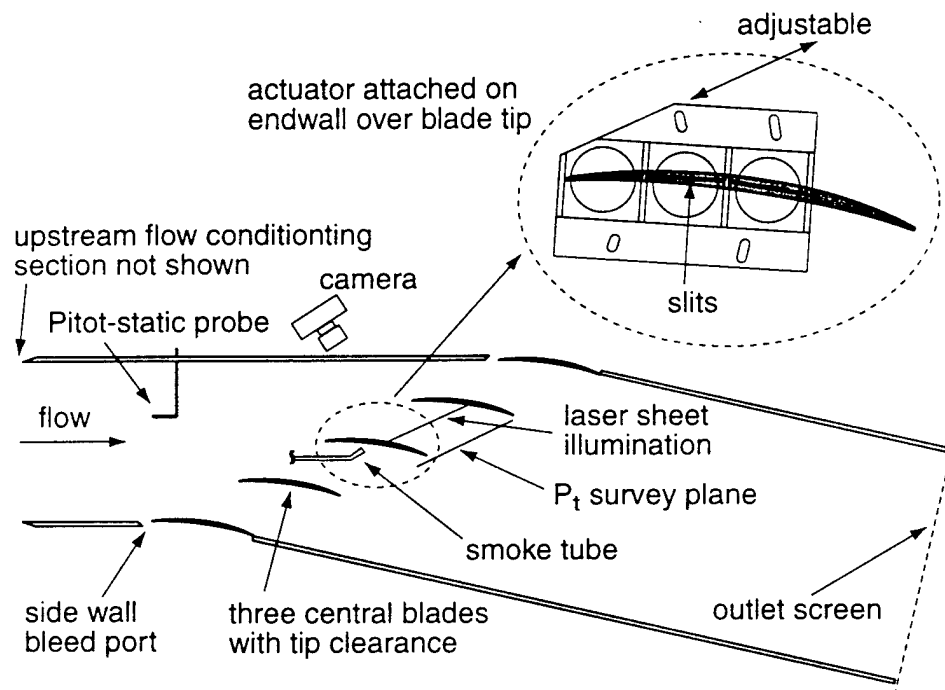


Figure 2.2 Schematic of cascade wind tunnel test section.

2.2.2 Instrumentations

All the data are taken using an Intel® Pentium® II 266MHz PC running on Microsoft® Windows NT® 4.0. The PC is equipped with a data acquisition card (PCI-6071E) manufactured by National Instruments™. The data acquisition board has 1.25MS/sec maximum sampling rate, 12-bit resolution, and 32 differential channels for A/D conversion.

The static pressure distribution on blade surfaces is measured using blades instrumented with static pressure taps described earlier. The tubes embedded in the blade as well as other pressure sensing probes described in the following are connected to pressure transducers via Tygon® tubes. A 3.2mm outer diameter Pitot-static probe manufactured by United Sensor is used to measure far upstream reference conditions about $2.1C$ upstream of the blade leading edge plane. The static pressure rise across the blade passage is measured by averaging six equally spaced static pressure taps drilled onto the casing endwall along the line $5\%C$ downstream of the trailing edge plane of the third blade passage from the bottom in Figure 2.2.

To assess the effects of the actuation on the time-average performance of the compressor cascade, the total pressure is surveyed using a Kiel probe in the survey plane, $5\%C$ downstream of the trailing edge plane as shown in Figure 2.2. The Kiel probe with 3.2mm outer diameter head manufactured by United Sensor is attached to a three-axis TSI® traverse table model 9400, which has 0.01mm position resolution with built-in backlash compensation loop. The Kiel probe measures the total pressure within 1% error up to $\pm 48^\circ$ yaw angle and $\pm 45^\circ$ pitch angle of the flow. It allows total pressure measurements without rotating or aligning the probe with the local flow direction. The traversing is programmed and performed automatically over the survey area (1 pitch \times 0.5 span) with a mesh size of 19 (pitchwise) \times 13 (spanwise).

Two Setra pressure transducers Model 239 with 0 – 2.5"WC (or 623 Pa) are used to measure differential pressures. One is dedicated to measure the far upstream reference dynamic head from the Pitot-static probe. The other is used to measure either the total pressure loss coefficient, ω or the static pressure coefficient, C_p . The Setra pressure transducers have $\pm 0.14\%$ FS accuracy.

Along with time-average measurements, unsteady measurements are also taken to study the mechanism of the actuation in detail. A DANTEC single $5\mu\text{m}$ thick hot-wire (probe type 55 P11) with DANTEC CTA bridge 56C17 is used to take unsteady measurements. The hot-wire is held by a holder made out of a 1.27cm diameter Al tube, which is attached to the traverse table that positions the hot-wire. The holder extends about 17cm upstream to minimize the interference. The signal from the hot-wire anemometer is filtered through an anti-aliasing low-pass filter (Frequency Devices 901F) before sampled by the data acquisition card. The hot-wire anemometer is also used in characterizing the jet actuators as described in subsection 2.3.2.

2.2.3 Flow Visualization

Flow visualization has been used to interrogate the changes in the behavior of the tip clearance flow with actuation. The primary interest is the change in mixing level of the leakage jet with main flow due to actuation.

The setup for the flow visualization is shown in Figure 2.2. The interrogation plane is 55°C from the leading edge and is parallel to the leading edge plane. A cylindrical lens is used to fan a beam from a He-Ne LASER illuminating the plane through the bottom wall of the test section. The LASER rated Class III-b is a product of Melles Griot with 15mW maximum output at 632.8nm. The actual output is about 7mW. Flow is seeded with smoke generated by burning incense sticks in a small separate chamber. Regulated and metered shop air is fed to the chamber. The outlet of the smoke chamber is connected to a metal tube (with O.D. of 6.4mm, labeled as "smoke tube" in Figure 2.2) releasing the smoke in the test section. The flattened exit of the tube is placed near the entrance of the tip clearance on the pressure side and is directed parallel to the LASER sheet as shown in Figure 2.2 as the local leakage jet is approximately in the same direction. The flow rate of the shop air into the smoke chamber is set such that the velocity at the exit of the tube is the same as the far upstream velocity so as to be more or less isokinetic with the wind tunnel flow. By placing the tube on the pressure side of the tip gap, the leakage jet is marked with the smoke. Acceleration near the entrance of the clearance attenuates the disturbance caused by the smoke tube.

A Nikon FM2 35mm camera is placed outside the test section as shown in Figure 2.2. Kodak TMAX P3200 films are used at the shutter speed of 2 (0.5sec exposure) with f-stop of 2.8, *i.e.* fully opened aperture. Processed images only provide time-average flow structures due to the long exposure time.

2.3 Actuator

2.3.1 Actuator Design and Fabrication

Since the actuator amplitude and the bandwidth requirements for the tip clearance flow control is not clearly known in advance, the general design guideline for the jet actuator is to maximize both the amplitude and bandwidth in hope of achieving enough control authority. The actuator requirements for the boundary layer separation control (Lorber *et al.* [2.7], McCormick [2.8], Seifert *et al.* [2.9]) do not necessarily guarantee success in tip clearance flow control. To maximize both the amplitude and bandwidth, two design guidelines are set: the first is to allow maximum stroke of the voice coil for a given area ratio and the second is to minimize the cavity volume for given geometrical restrictions to raise the Helmholtz resonance frequency (Dowling and Ffowcs Williams [2.10]) as high as possible.

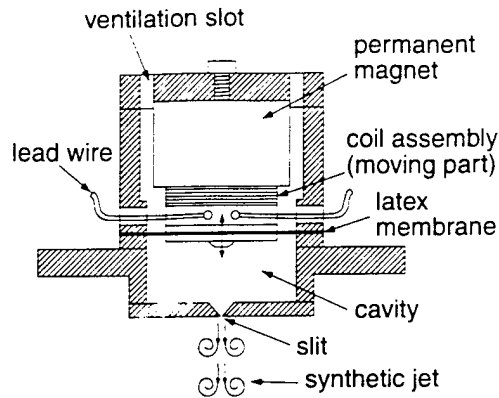


Figure 2.3 Schematic of synthetic jet actuator used in cascade rig. Configuration of Normal Synthetic Jet actuator with slit.

The schematic of the actuator used in the cascade is shown in Figure 2.3. This actuator is widely known as synthetic jet actuator (Amitay *et al.* [2.11], Smith *et al.* [2.12]) and it consists of a vibrating membrane, a cavity, and a slit (in case of Normal Synthetic Jet or NSJ) or holes (in case of Directed Synthetic Jet or DSJ). There are three isolated synthetic jet actuators inline in the direction normal to Figure 2.3. Note that the backside of the membrane is open to the atmosphere as the static pressure in the wind tunnel test section is small enough (the difference is about 1% of atmospheric pressure) that the back pressurization is not necessary (See Figure 2.2 and Figure 2.5 for a top view of the installed actuator and Figure 2.4 for a side view). The Normal Synthetic Jet actuator has three straight slits that are shaped to approximately follow the camberline of the blade (Figure 2.2) while the Directed Synthetic Jet actuator has four tilted holes per actuator (12 holes total) that are directed approximately to the chordwise direction and tilted by 25° from the casing wall (Figure 2.4 and Figure 2.5). The actuator covers first 70% C from the leading edge because most of the benefit associated with actuation is expected to be attained near the leading edge (Khalid *et al.* [2.13]). To study the dependence on pitchwise location of the actuator, the casing wall with the actuator has been made adjustable in the pitchwise direction as indicated in Figure 2.2 and Figure 2.5. The dimensions of the actuator are summarized in Table 2.2.

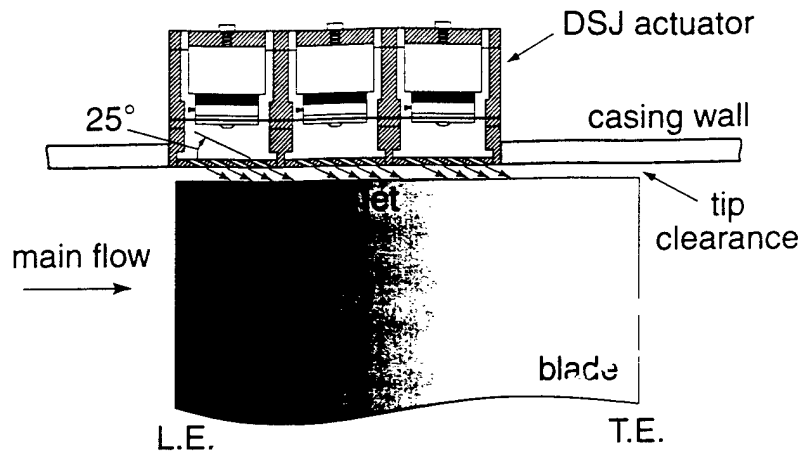


Figure 2.4 Schematic of DSJ actuator mounted on casing wall.

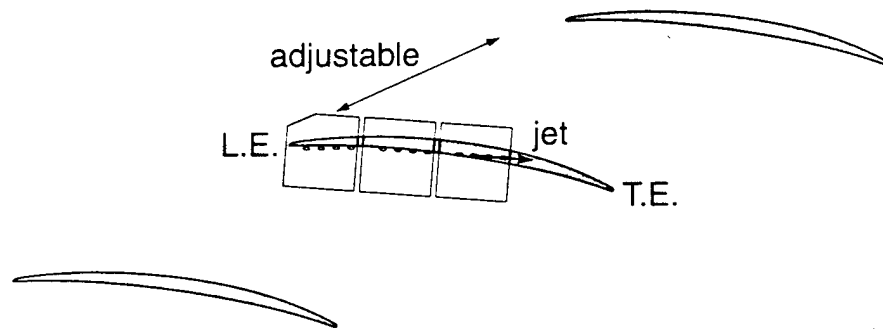


Figure 2.5 Schematic of Directed Synthetic Jet (DSJ) actuator mounted on casing wall showing the direction of the jet.

Because of compact geometry requirements, compact and rugged BEI Kimco voice coil actuators (LA13-12-000A) are used to drive the membrane. The voice coil actuator has 15.5N peak force, ± 3.18 mm stroke, and 14gram coil assembly. To allow for maximum excursion of the voice coil, 0.51mm thick latex sheet is used for the membrane. The latex membrane has two functions: the first is to provide sealing of the cavity and the second is to position the coil assembly in the center relative to the permanent magnet. The membrane is pre-stretched around a wooden frame and holes on the membrane for fastening screws are die-cut. It is then sandwiched and fastened on to the Al housing shown in Figure 2.3 with hatches and also on to the coil assembly between two disks that are 2.6cm in diameter. The membrane is finally freed from the wooden frame. The pre-stretch is necessary to avoid wrinkles on the membrane while tightening screws. Sinusoidal signal generated with a WAVETEK function generator model 29 is amplified with Yorkville AP4040 audio amplifiers and then fed to the voice coil actuator.

Table 2.2 Dimensions of synthetic jet actuator.

External length	136.5mm
External width	47.6mm/85.7mm (including mounting flanges)
External height	56.1mm
Cavity volume per actuator	$1.52 \times 10^4 \text{mm}^3$
Slit/Hole plate thickness	3.18mm
Slit width (NSJ)	0.254mm
Slit area per actuator (NSJ)	10.5mm^2
Hole diameter (DSJ)	1.59mm
Hole length (DSJ)	7.51mm
Hole area per actuator (DSJ)	7.92mm^2

For Steady Directed Jet (SDJ) actuation, the housing of the voice coil actuator and membrane is replaced with a plenum that supplies regulated shop air to the 12 holes on the plates. The flow rate into the plenum is regulated using a pressure regulator and a needle valve and is measured using a Teledyne Electronic Technologies HFM-201 flow meter with a range of 0 – 300 SLPM of air and 0 – 5V output.

2.3.2 Actuator Performance Characterization

The amplitude/frequency response of the actuator (NSJ and DSJ) is characterized by measuring the jet velocity at the exit of the slit or the hole with a DANTEC hot-wire anemometer. The measurements are carried out on a separate test bench. The hot-wire is positioned using a manual X-Y-Z axis precision positioning stage that is isolated from the test bench that holds the actuator. The measured response of the NSJ actuator is shown in Figure 2.6. The peak-to-peak driving voltages of the voice coil are labeled in the figure. The peak center jet velocity, $U_{j, peak}$ on the vertical axis is determined from an ensemble-average of 20 jet velocity cycles measured at the center of the jet. The error bar in Figure 2.6(a) represents an estimated 95% confidence interval of the velocity measurement. Using a linear interpolation of the measurement, an input voltage for the cascade actuation experiment is calculated for a desired jet velocity $U_{j, peak}$ at a desired frequency f within the envelope that is defined by the maximum input voltage to the voice coil. Since the total pressure of the actuator jet is much higher than the static pressure variation in the cascade test section, it is assumed that the actuator performance remains unchanged during the wind tunnel testing. A post-calibration of the actuator taken after a usage about 50 hours on the cascade experiment shows no significant changes in the actuator performance as shown in Figure 2.6(a). However, the membrane has to be replaced from time to time, because it breaks along the sandwiched edges after being used for more than about 50 hours. There are membrane-to-membrane variations in the

response because the amount of pre-stretch has not been controlled precisely. Therefore, a new amplitude/frequency response is measured every time the membrane is replaced.

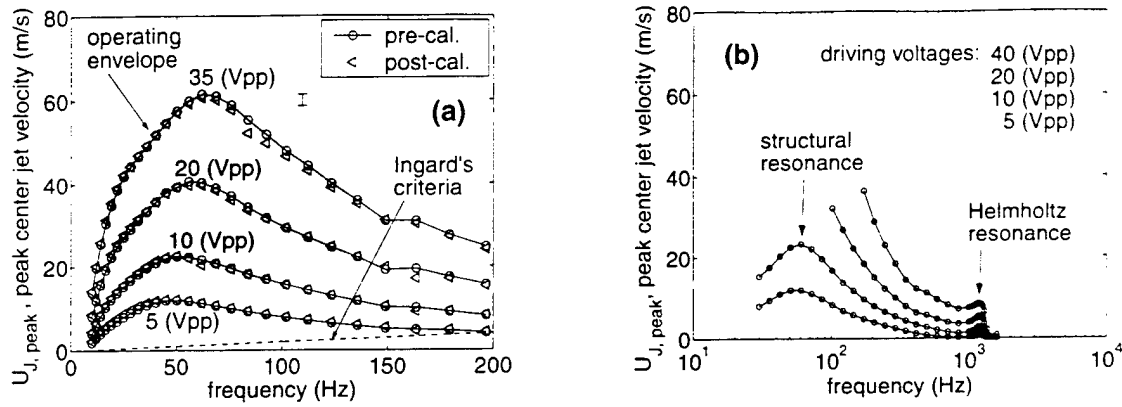


Figure 2.6 Amplitude/frequency response of NSJ actuator: (a) comparing pre- and post-calibration on linear scale abscissa; (b) calibration taken over larger frequency range shown on log scale abscissa. Actuator slit size $d = 0.25\text{mm}$. Vpp is peak-to-peak driving voltage. Data of two different membranes.

The structural resonance frequency of the voice coil and membrane system is measured using an impulse test without cavity and slit/hole plates. The coil assembly is tapped with a hammer and the back EMF ($\mathcal{E} = BLv$ where B is the magnitude of the magnetic field, L is the total length of coil, and v is the velocity of the coil assembly) generated by the movement of the voice coil is recorded. The measured time trace is compared to a simulated time trace that is based on the standard second-order model:

$$H(s) = \frac{K}{s^2 + \frac{\omega_n}{Q}s + \omega_n^2}$$

The simulated time trace with the natural frequency, $f_n = \omega_n/(2\pi) = 54.7\text{Hz}^\dagger$ and the quality factor, $Q = 1/(2\zeta) = 4.4$ matches the measurement well as shown in Figure 2.7. The peak near 55Hz in the actuator calibration shown in Figure 2.6(a) and (b) thus corresponds to the structural resonance. Note the frequency of the peak increases (by about 15Hz) as the driving voltage increases. The shift is due to the added stiffness associated with the compliance of the air in the cavity. The built-in high-pass filter in the audio amplifier with cutoff frequency of 20Hz results in the roll-off of the actuator jet velocity below the cutoff frequency as shown in Figure 2.6(a).

[†] As mentioned above, the structural resonance frequency f_n varies slightly depending on the amount of pre-stretch applied to the membrane.

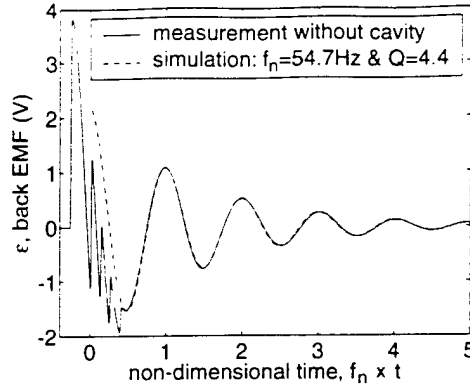


Figure 2.7 Comparison between measured and simulated impulse responses of voice coil and membrane system.

The Helmholtz resonance frequency, f_H [2.10] is

$$f_H = \frac{a}{2\pi} \sqrt{\frac{A_{neck}}{L_{neck} \cdot V_{cavity}}}$$

where a is the speed of the sound, A_{neck} is the area of the neck (slit or holes), L_{neck} is the length of the neck, and V_{cavity} is the volume of the cavity (See Figure 2.3). Assuming that the thickness of the slit plate is the effective length of the neck, the predicted Helmholtz frequency, f_H is 800Hz based on Table 2.2. However, the second peak in the measured actuator response exists at around 1200Hz as shown in Figure 2.6(b). This is possibly because the chamfered slit reduces the effective length of the neck. In fact, the predicted Helmholtz resonance frequency becomes 1130Hz when the neck length is substituted by a half of the slit plate thickness. Above the Helmholtz resonance peak, the actuator response rolls off quickly to zero. It turns out that the Helmholtz resonance frequency is high enough to allow bandwidth necessary for the cascade experiments. The gray shaded area in Figure 2.6(a) is the operating envelope of the actuator used in the cascade experiments.

Ingard [2.14] identified different operating regimes of synthetic jets. At sufficiently high levels of excitation, the amplitude of the particle displacement in the neck exceeds the length of the neck. The dividing line is

$$U_{J, peak} = 2\pi f L_{neck}$$

as plotted in Figure 2.6(a) with a dashed line. The actuator operates well above the line meaning that it is in the acoustic streaming regime that generates discrete vortices.

Figure 2.8 shows amplitude/frequency response of DSJ actuator. It is similar to that of NSJ shown above with a peak near the structural resonance frequency. Ensemble-average time-traces of DSJ velocity and momentum over a period are shown in Figure 2.9. A directed jet is formed during an injection stroke, while ingestion from all direction is created during a suction stroke. It is only the injection stroke that

contributes to the directed momentum. Therefore the time-average momentum of DSJ is determined excluding the suction stroke and is

$$\overline{(\rho U_J^2 A_J)} = 0.28 \times (\rho U_{J,peak}^2 A_J)$$

as indicated in Figure 2.9(b). The time-average momentum is used to compare DSJ with Steady Directed Jet (SDJ).

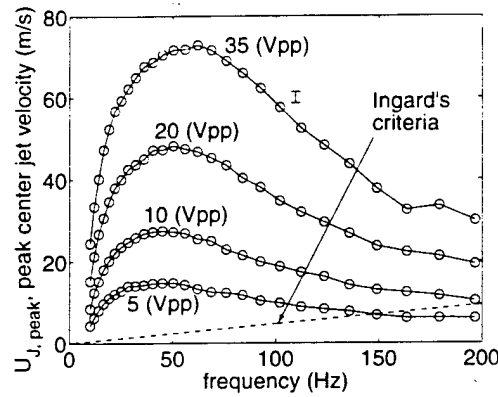


Figure 2.8 Amplitude/frequency response of DSJ actuator.

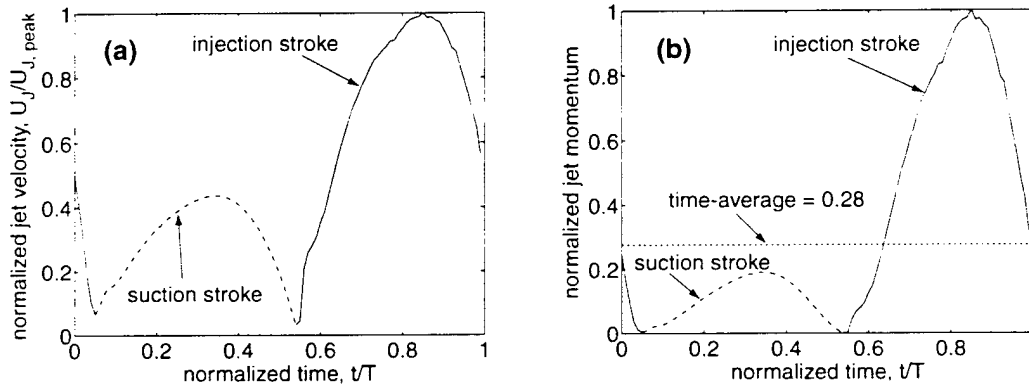


Figure 2.9 Time-trace of DSJ: (a) velocity; (b) momentum. Ensemble-average of 20 cycles.

The calibration of the Steady Directed Jet (SDJ) actuator is shown in Figure 2.10. The jet velocity is again measured with a hot-wire placed at the exit of the actuator hole. A desired jet velocity for the cascade experiment is achieved by setting the flow rate (or the voltage readout of the flow meter) based on the least square fit calibration line in Figure 2.10.

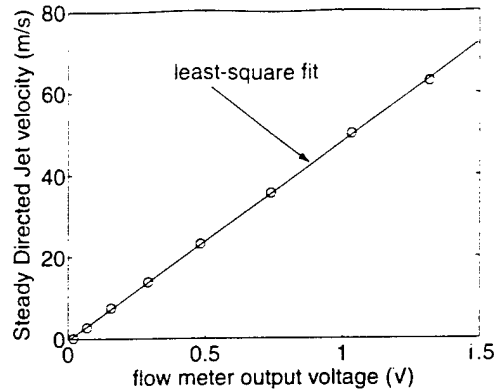


Figure 2.10 Calibration of Steady Directed Jet (SDJ) actuator.

References

- [2.1] Storer, J. A. and Cumpsty, N. A., "Tip Leakage Flow in Axial Compressors", ASME Paper No. 90-GT-127, 1990.
- [2.2] Heyes, F. J. G., Hodson, H. P., and Dailey, G. M., "The Effect of Blade Tip Geometry on the Tip Leakage Flow in Axial Turbine Cascades", J. of Turbomachinery, July 1992, pp.643-651.
- [2.3] Bindon, J. P., "The Measurement and Formation of Tip Clearance Loss", J. of Turbomachinery, July 1989, pp.257-263.
- [2.4] Saathoff, H. and Stark, U., "Endwall Boundary Layer Separation in a High-Stagger Compressor Cascade and a Single-stage Axial-Flow Low-Speed Compressor", Forschung im Ingenieurwesen, Vol. 65 Issue 8, 2000, pp. 217-216, Springer.
- [2.5] Khalid, S. A., "The Effect of Tip Clearance on Axial Compressor Pressure Rise", Gas Turbine Laboratory, Massachusetts Institute of Technology, Revised version of Ph.D. Thesis, May 1995.
- [2.6] Drela, M. and Youngren, H., "A User's Guide to MISES 2.1", MIT Computational Aerospace Science Laboratory, 1995.
- [2.7] Lorber, P. F., McCormick, D. C., Anderson, T. J., Wake, B. E., MacMartin, D. G., Pollack, M. J., Corke, T. C., and Breuer, K. S., "Rotorcraft Retreating Blade Stall Control", AIAA 2000-2475, 2000.
- [2.8] McCormick, D. C., "Boundary Layer Separation Control with Directed Synthetic Jets", AIAA 2000-0519.
- [2.9] Seifert, A., Bachar, T., Koss, D., Shepshelovich, M., and Wagnanski, I., "Oscillatory Blowing: A Tool to Delay Boundary-Layer Separation", AIAA 93-0440, 1993.
- [2.10] Dowling, A. P. and Ffowcs Williams, J. E., "Sound and Sources of Sound", Ellis Horwood Limited, 1983.
- [2.11] Amitay, M., Honohan, A., Trautmann, M., and Glezer, A., "Modification of the Aerodynamic Characteristics of Bluff Bodies Using Fluidic Actuators", AIAA 97-2004, 1997.
- [2.12] Smith, D. R., Amitay, M., Kibens, V., Parekh, D., and Glezer, A., "Modification of Lifting Body Aerodynamics Using Synthetic Jet Actuators", AIAA 98-0209, 1998.

- [2.13] Khalid, S. A., Khalsa, A. S., Waitz, I. A., Tan, C. S., Greitzer, E. M., Cumpsty, N. A., Adamczyk, J. J., and Marble, F. E.. "Endwall Blockage in Axial Compressors", ASME Paper No. 98-GT-188.
- [2.14] Ingard, U., "On the Theory and Design of Acoustic Resonator", J. of the Acoustical Society of America, Vol. 25, No. 6, November 1953.

3 Baseline Performance

The cascade performance without actuation has to be characterized before implementing any flow control to determine if the cascade behaves as designed and to assess how sensitive the performance is to the tip clearance size. Thus the measurements presented in this section would serve as the baseline results to which those from experiments with flow control (discussed in the next section) can be compared for assessing the utility of proposed flow control strategies.

3.1 Effect of Reynolds number

It is desirable to operate the cascade wind tunnel at a speed that is as low as possible so that the amplitude and bandwidth requirement of the actuator is minimized. However, the Reynolds number of the cascade needs to be above the critical Reynolds number to ensure Reynolds number independent results. Surveys of the total pressure loss coefficient have been carried out at various Reynolds numbers by varying the upstream flow velocity. The contours of the total pressure loss coefficients,

$$\omega = \frac{P_{t,\infty} - P_t}{q_\infty}$$

measured with the Kiel probe 5%*C* downstream of the trailing edge plane are shown in Figure 3.1(a) – (e). The tip clearance is 3%*C*. The survey area is 1 pitch \times 0.5 span. The interval between contour lines is 10% of far upstream reference dynamic head ($0.1q_\infty$). The uncertainty in ω is ± 0.034 with 95% confidence. At $Re_c = 50,000$ (Figure 3.1(a)), the flow on the blade surface is not fully attached due to a laminar separation causing a thick blade wake with large total pressure loss and blockage. The design blade loading is not established and the small pressure difference across the blade results in the tip clearance vortex that is smaller and closer to the blade suction surface. As the Reynolds number increases, the boundary layer on the blade surface becomes healthy and the contour of the total pressure loss coefficient becomes insensitive to the Reynolds number. Integrated flow blockage is computed[†] and plotted against the Reynolds number as shown in Figure 3.2. The cascade flow is Reynolds number independent when $Re_c \geq 100,000$. Therefore, all the quantitative measurements presented in the following have been done above the critical Reynolds number.

[†] Section 3.4 describes how the blockage is computed.

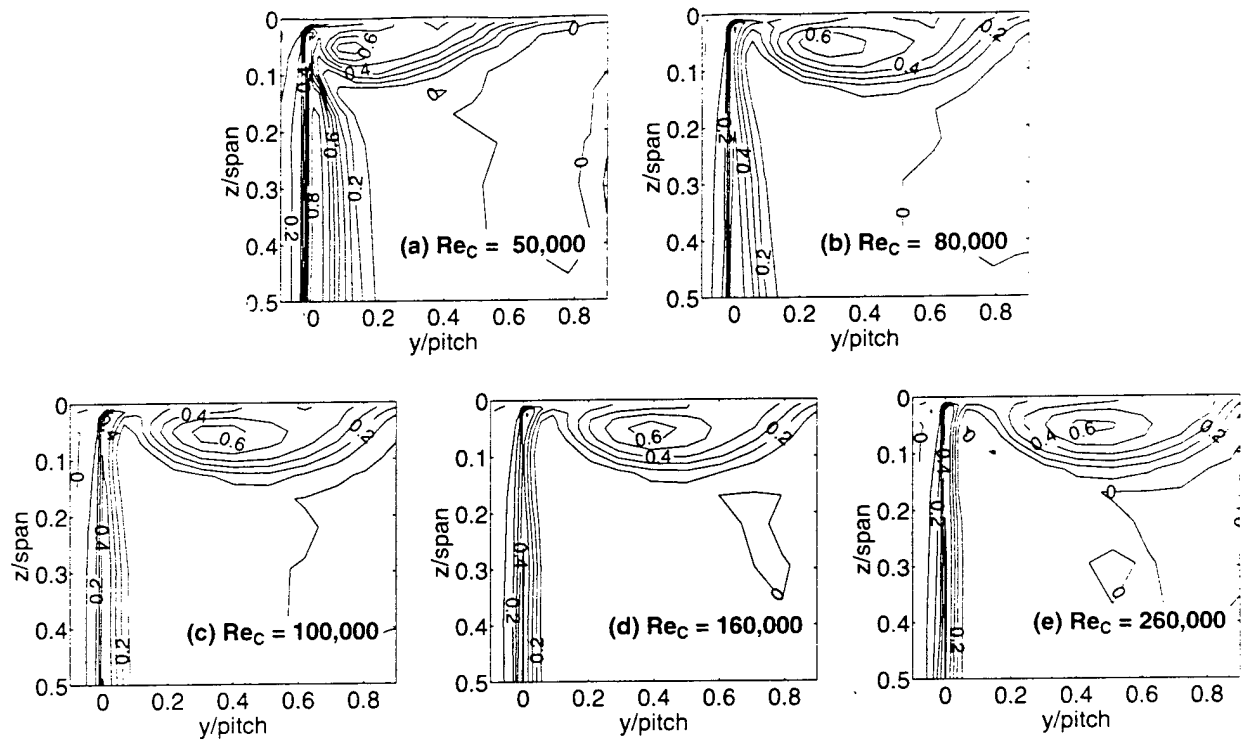


Figure 3.1 Contours of total pressure loss coefficient with various Reynolds numbers. 3% C tip clearance.

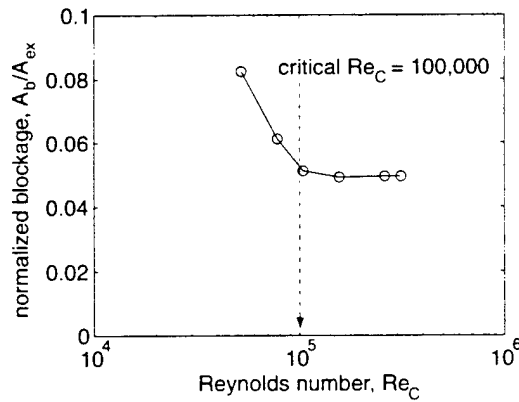


Figure 3.2 Reynolds number dependence and critical Reynolds number.

3.2 Flow Near Mid-span

The cascade is tuned by adjusting the upstream sidewall bleed ports and the downstream sidewall angle to achieve near blade-to-blade periodicity and design loading. The measured static pressure along mid-span on the center blade is compared with computed result using MISES [3.1] as shown in Figure 3.3. The error bar in the figure is the uncertainty in C_p measurement with 95% confidence. There is good agreement between measurements and MISES prediction. It confirms that the cascade has been set up

correctly according to the design as summarized in Table 2.1. The difference in the mid-span static pressure distribution with 0% C and 3% C clearances is negligible, *i.e.* the mid-span loading remains the same.

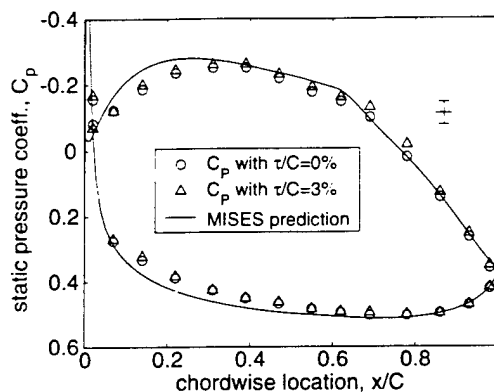


Figure 3.3 Mid-span C_p distribution. Comparison between measurements on center blade and CFD prediction using MISES [3.1].

3.3 Survey of Total Pressure Loss Coefficient

Figure 3.4(a) – (e) show the contour plots of the total pressure loss coefficient, ω without actuation for various tip clearance sizes: $\tau = 0, 1, 2, 3$, and 4% C respectively. The contour plot with 0% C clearance (Figure 3.4(a)) shows that the endwall boundary layer remains close to the casing wall. As the tip clearance increases, the area of the low total pressure (or momentum) fluid in the endwall region increases. With tip clearance the low total pressure area extends from both the suction surface as well as the endwall. The pitchwise location of the tip clearance vortex core remains more or less the same regardless of the tip clearance gap as was shown by Chen *et al.* [3.3].

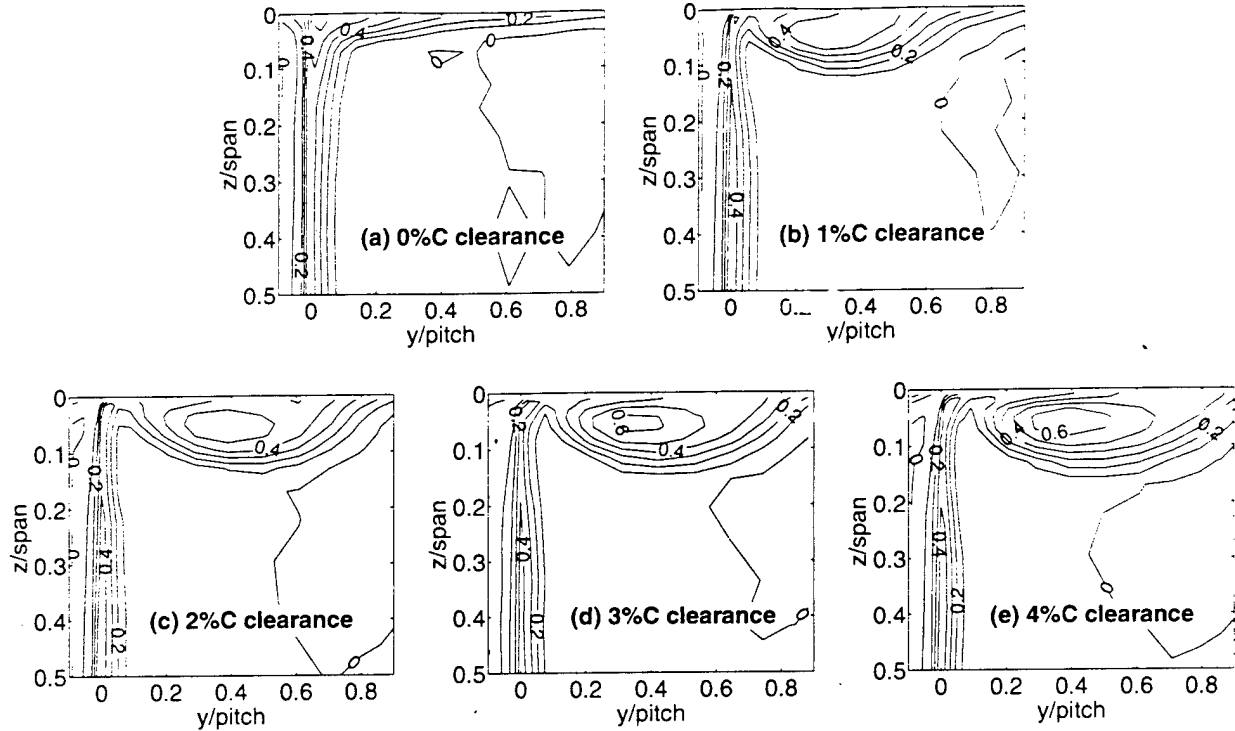


Figure 3.4 Contours of total pressure loss coefficient, ω measured 5%C downstream of trailing edge plane.

3.4 Effect of Tip Clearance Size on Performance

To quantify the effect of tip clearance size on pressure rise and loss, the endwall blockage, static pressure rise, mass-average total pressure loss, and stream thrust-average total pressure loss are plotted against tip clearance size.

Figure 3.5 shows the endwall flow blockage vs. tip clearance. Flow blockage is a three-dimensional extension of the displacement thickness concept and is defined as follows:

$$A_b = \int \left(1 - \frac{U_x}{U_{x,edge}} \right) dA$$

The integration is done only over the defect region, whose edge is defined as $\omega = 0.05$ in this study. To compute the blockage from the total pressure loss coefficient survey data in Figure 3.4, it is assumed that in the surveyed plane the static pressure is uniform and equal to the exit static pressure measured with the taps on the casing wall and the flow is unidirectional in the direction of the mass-average exit flow angle near mid-span predicted by MISES. The axial velocity in the plane is then:

$$U_x = U_\infty \sqrt{(1 - \omega - C_{P,ex})} \cos \beta_{ex}$$

The endwall blockage is computed by subtracting the blockage associated with the blade surface boundary layers from the total blockage:

$$A_{b,ew} = A_b - \left(\delta^* \times \frac{h}{2} \right)$$

where δ^* is the displacement thickness of the blade wake near mid-span and h is the length of the blade span. The endwall blockage shown in Figure 3.5 is normalized by the exit area, $A_{ex} = s \times h$. The uncertainty introduced by the assumption and the measurement error is estimated for 3% C clearance and the uncertainty bound with 95% confidence level is shown in Figure 3.5. The solid line is the least-square fit of the data points. The endwall blockage is recognized to increase linearly with tip clearance (Khalid *et al.* [3.4]).

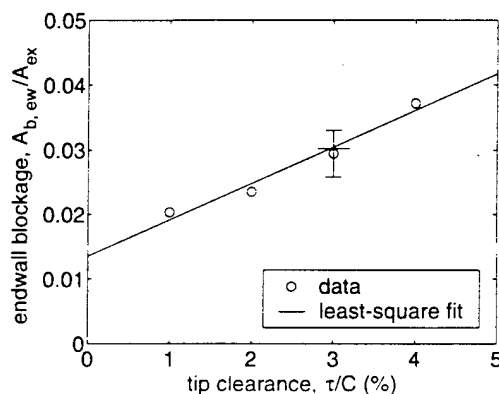


Figure 3.5 Endwall blockage measured 5% C downstream of trailing edge plane vs. tip clearance size.

Figure 3.6 shows the exit static pressure measured using the six pressure taps on the casing wall 5% C downstream of the trailing edge plane. Again the solid line is the least-square fit of the data. The dashed line is an estimation based on the least-square fit of the blockage measurements assuming one-dimensional diffuser analogy:

$$C_{p,ex} = 1 - \{1 - (C_{p,ex})_{\tau=0}\} \cdot \left\{1 - \left(\frac{A_{b,ew}}{A_{ex}}\right)_{\tau=0}\right\}^2 \bigg/ \left(1 - \frac{A_{b,ew}}{A_{ex}}\right)^2$$

Increased endwall blockage with larger tip clearance results in reduced static pressure rise as expected. However, the uncertainty in the measurement is larger than the quantities of interest as indicated by the error bar in Figure 3.6. Therefore, the endwall blockage is chosen over the exit static pressure as a measure of pressure rise capability.

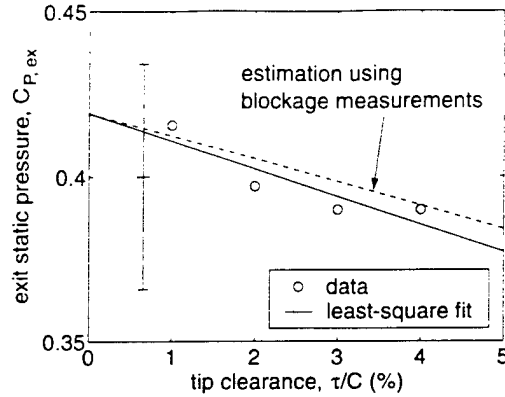


Figure 3.6 Static pressure measured 5% C downstream of trailing edge plane using six pressure taps on endwall.

The mass-average endwall total pressure loss coefficient is computed from the Kiel probe measurements under the same assumptions as in the blockage calculation. Figure 3.7 shows the mass-average endwall total pressure loss coefficient plotted for various tip clearance sizes. The mass-average total pressure loss coefficient is a measure of the total pressure loss incurred from the far upstream reference state to the averaging plane and is defined as follows:

$$\bar{\omega}^m = \frac{\int \omega U_x dA}{\int U_x dA}$$

The two-dimensional profile loss associated with blade wake is subtracted from the mass-average total pressure loss coefficient, $\bar{\omega}^m$ to get the mass-average endwall total pressure loss coefficient, $\bar{\omega}_{ew}^m$. Again the estimated uncertainty with 95% confidence level is shown in the figure with an error bar. It is recognized that the loss due to the tip clearance flow increases linearly with tip clearance for a fixed mid-span loading (Storer and Cumpsty [3.5]). The solid line in Figure 3.7 is a least-square fit of the data.

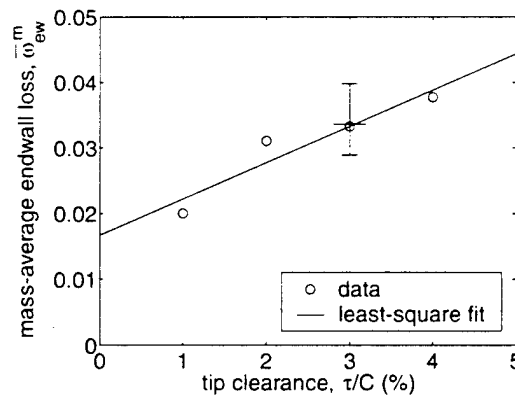


Figure 3.7 Mass-average endwall total pressure loss coefficient vs. tip clearance size.

Figure 3.8 shows the stream thrust-average (or fully mixed-out) endwall total pressure loss coefficient vs. tip clearance. The stream thrust-average endwall loss is calculated by hypothetically mixing out the flow in the surveyed area (excluding the blade wake) to a uniform state in a constant area duct while conserving mass and momentum. The flow field is again estimated under the same assumptions made in the blockage calculation. Note that the stream thrust-average endwall loss is larger than the mass-average endwall loss shown in Figure 3.7 since it includes the additional mixed-out loss from the surveyed plane to the hypothetical uniform state. Storer and Cumpsty [3.5] proposed an analytical model based on a control volume analysis to predict the total pressure loss due to the tip leakage flow. The model is applied to the current cascade and the result is shown in Figure 3.8. The model only accounts for the loss due to the tip leakage flow, which is assumed to be zero for no clearance. The endwall loss with zero clearance in the measurement is due to the endwall boundary layer. Therefore, the intercept of the dashed line with the ordinate is anchored to the intercept of the least-square fit line. The measurement and the prediction are in good agreement justifying the assumptions made in the calculation of the stream thrust-average loss from the total pressure measurements.

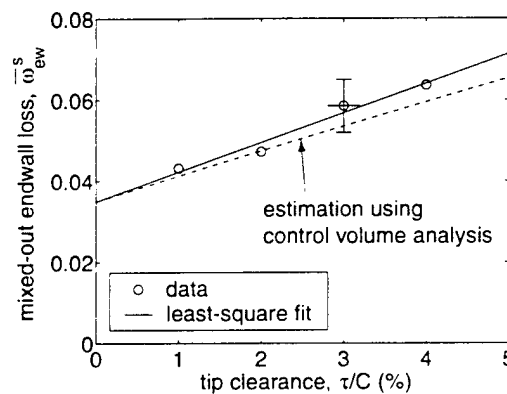


Figure 3.8 Stream thrust-average total pressure loss coefficient vs. tip clearance size.

In summary, the tip clearance-related endwall blockage, mass-average loss, and stream thrust-average (mixed out) loss all increase linearly with tip clearance; this has the implication that for a fixed mid-span loading the leakage flow rate is proportional to the tip clearance size (Storer and Cumpsty [3.5]). The results of Figure 3.5 through Figure 3.8 are the baseline results to which those from the experiments with flow control can be contrasted to identify the bulk flow process responsible for the measured changes in flow blockage with actuations. These aspects will be described in Section 4.

3.5 Effect Of Blade-To-Blade Non-Periodicity On Endwall Blockage

We have only used one set of actuators to affect the endwall flow of the third passage from the bottom in Figure 2.2; thus there is a need to examine the effect of blade-to-blade non-periodicity. This is done

through setting the tip clearances of the three central blades to be different from one another. Non-uniform tip clearances would generate blade-to-blade non-periodicity, as the endwall blockage in each blade passage can be different from the other. Two cases have been tested. In the first case, the tip clearance of the center blade are set to $1\%C$ and those of two adjacent blades are set to $3\%C$. Measured blockage and loss of the third blade passage are compared with the case wherein all three central blades have uniform tip clearance of $1\%C$. In the second case, the tip clearance of the center blade are set to $4\%C$ and those of two adjacent blades are set to $2\%C$. Measured blockage and loss of the third blade passage are now compared with the case wherein all three central blades have uniform tip clearance of $4\%C$. The results of the above two cases are shown in Figure 3.9. Both cases match the uniform tip clearance case well within the uncertainty. In other words, 50 – 70% blade-to-blade variations of the tip clearance size and related blockage and loss do not affect the measurement significantly. The results suggest that the effect of the tip clearance is limited within one blade pitch (or spacing) in the current cascade.

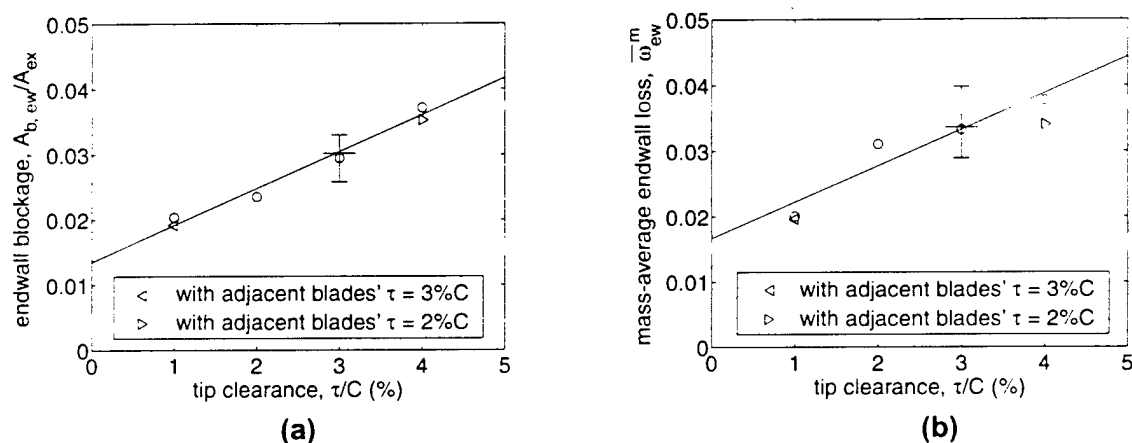


Figure 3.9 Measurements with non-periodic tip clearances compared with measurements with uniform tip clearances: (a) endwall blockage; (b) mass-average endwall loss.

References

- [3.1] Drela, M. and Youngren, H., "A User's Guide to MISES 2.1", MIT Computational Aerospace Science Laboratory, 1995.
- [3.2] Greitzer, E. M., "Internal Flows in Turbomachines", Class Notes, MIT Course No. 16.540, Spring 1996.
- [3.3] Chen, G. T., Greitzer, E. M., Tan, C. S., and Marble, F. E., "Similarity Analysis of Compressor Tip Clearance Flow Structure", ASME Paper No. 90-GT-153.

- [3.4] Khalid, S. A., Khalsa, A. S., Waitz, I. A., Tan, C. S., Greitzer, E. M., Cumpsty, N. A., Adameczyk, J. J., and Marble, F. E., "Endwall Blockage in Axial Compressors", ASME Paper No. 98-GT-188.
- [3.5] Storer, J. A. and Cumpsty, N. A., "An Approximate Analysis and Prediction Method for Tip Clearance Loss in Axial Compressors", ASME Paper No. 93-GT-140.

4 Time-Average Effects of Actuation

In this section, the effects of actuations on the time average change in tip clearance-related blockage and loss are determined. Specifically we examine the influence of four parameters: these are the actuator type (NSJ, DSJ, or SDJ), the pitchwise location of the actuator on the casing relative to blade tip location, the amplitude of actuation, and frequency at which the actuation is applied. Parametric dependence (of the change in tip clearance blockage and loss) on the actuation amplitude and frequency is explored and discussed. The bulk flow processes responsible for the observed change in the blockage and loss are identified as well.

4.1 Normal Synthetic Jet Actuator

Discussions on the effect of the NSJ actuation are presented in this section. Figure 4.1(b) and (c) show the contour plots of ω taken with two pitchwise locations of the actuator: (b) directly over the blade tip and (c) approximately over the vortex core^s as indicated by the arrows. There is noticeable change in the contours for both locations compared to the baseline (a). As shown in Figure 4.2, the exit static pressure measurement indicates an increase in $C_{p, ex}$ with NSJ actuation, although it is only a qualitative comparison due to the large uncertainty in the measurement. Figure 4.1 and Figure 4.2 thus show that the tip clearance flow does respond to the NSJ actuation resulting in a change in the endwall flow field and the exit static pressure.

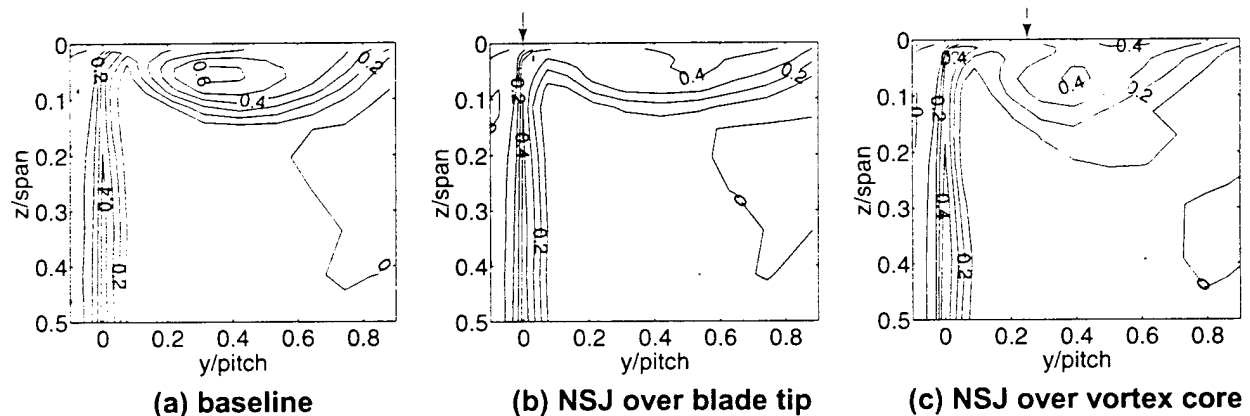


Figure 4.1 Contours of ω measured 5% C downstream of T.E. plane: (a) baseline without actuation, $\tau = 3\%C$; (b) NSJ directly over blade tip (0% pitch), $C_{\mu, \tau} = 0.88$, $F_C^+ = 1.0$; (c) NSJ over vortex core (25% pitch), $C_{\mu, \tau} = 0.88$, $F_C^+ = 1.0$. Arrows indicate locations of NSJ slits.

^s The actuator covers 70% C from L.E. Therefore, the NSJ slits upstream of the survey plane are approximately over the vortex core, although the arrow projected onto the survey plane appears to be closer to SS than the core.

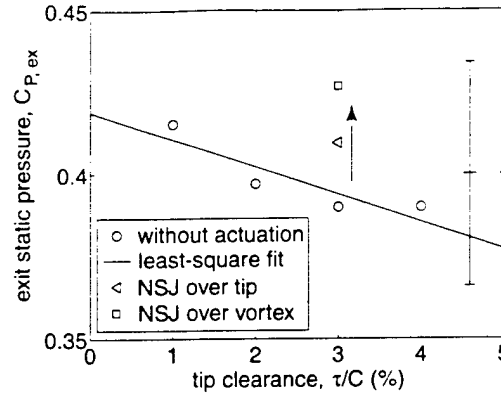


Figure 4.2 Exit static pressure with and without NSJ actuation. \square : NSJ directly over blade tip (0% pitch), $C_{\mu\tau} = 0.88$, $F_c^+ = 1.0$; \triangle : NSJ over vortex core (25% pitch), $C_{\mu\tau} = 0.88$, $F_c^+ = 1.0$.

4.1.1 Scaling of NSJ Actuator Amplitude

The momentum coefficient of the actuator is used as a measure of the actuation amplitude. The momentum of the actuation jet is normalized by the momentum of the leakage flow, which is what one wants to affect. The leakage flow momentum is approximated based on far upstream flow velocity. Although the magnitude of the leakage jet velocity varies over the blade chord, it does scale with U_∞ and is well approximated by U_∞ for different tip clearance sizes as shown in Figure 4.3. The magnitude of the leakage jet velocity in Figure 4.3 has been estimated from the static pressure measurement near the blade tip using a model proposed by Rains [4.4]:

$$U_L = \sqrt{\frac{2(P_{t,\infty} - P_{SS,tip})}{\rho}} = U_\infty \sqrt{1 - C_{P,SS,tip}}$$

where $P_{SS,tip}$ is the static pressure on the suction surface near the blade tip (1.5% C from the tip). It is based on the use of the Bernoulli equation, which assumes ideal flow without loss. Storer and Cumpsty [4.5] showed that its use is in good agreement with their measurements. The momentum coefficient is thus defined as:

$$C_{\mu,\tau} = \frac{\rho U_{J,peak}^2 A_J}{\rho U_\infty^2 \tau C}$$

where we have used the leakage flow momentum to non-dimensionalize the actuator peak momentum.

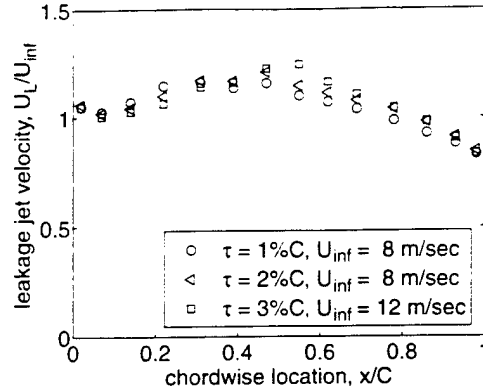


Figure 4.3 Magnitude of leakage jet velocity leaving tip clearance.

Figure 4.4 shows the tip clearance-related blockage versus amplitude (of actuation) for two tip clearances. The NSJ actuator is placed at a pitchwise location $0.25s$ (25% *pitch*) from the camberline of the center blade so that it is approximately over the vortex core. The blockage (mostly dominated by that associated with tip leakage flow) has been normalized by the baseline blockage of each clearance. The data set collapses onto a single curve with the implication that the actuator momentum does scales with the leakage flow momentum as expected. It is to be noted that most of the tip clearance-related blockage can be eliminated using the NSJ actuator at sufficiently high actuator amplitude.

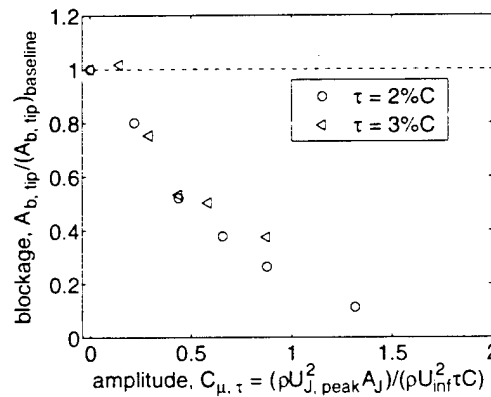


Figure 4.4 Tip clearance-related blockage vs. NSJ actuator amplitude. Actuator near vortex core. $F_C^+ = 1.0$.

The ω contour plots of two data points in Figure 4.4 are shown in Figure 4.5(b) and (c) along with that for the baseline in figure 4.5(a). The endwall region with low total pressure increases while the depth of the P_t defect decreases with NSJ actuation.

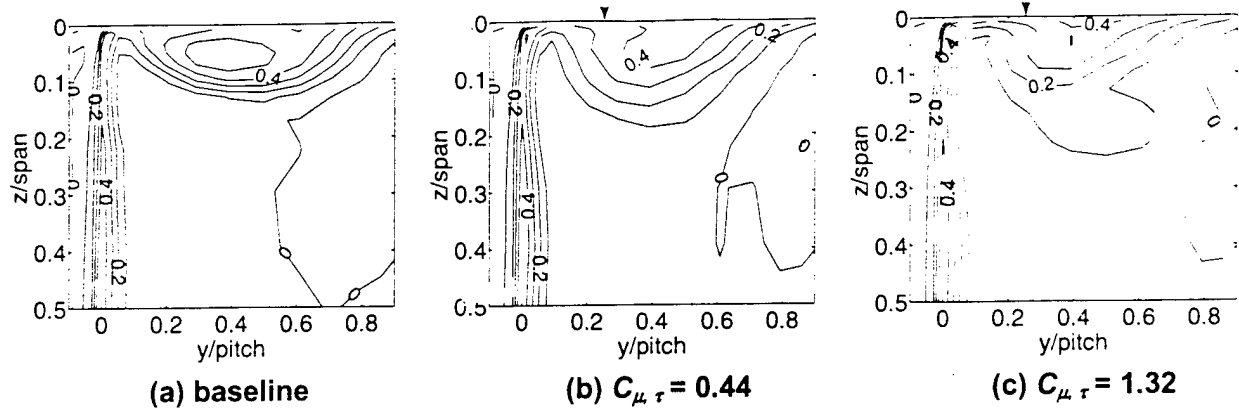


Figure 4.5 Contours of ω measured 5% C downstream of T.E. plane: (a) baseline without actuation, $\tau = 2\%C$; (b) NSJ over vortex core (25% pitch), $C_{\mu\tau} = 0.44$, $F_C^+ = 1.0$; (c) NSJ over vortex core, $C_{\mu\tau} = 1.32$, $F_C^+ = 1.0$.

The endwall blockages taken with two upstream velocities are plotted against the actuator amplitude as shown in Figure 4.6. The two data sets form a single trend when plotted non-dimensionally against $C_{\mu\tau}$ showing that the definition of $C_{\mu\tau}$ appropriately reflect the dependence of the blockage reduction on the far upstream velocity.

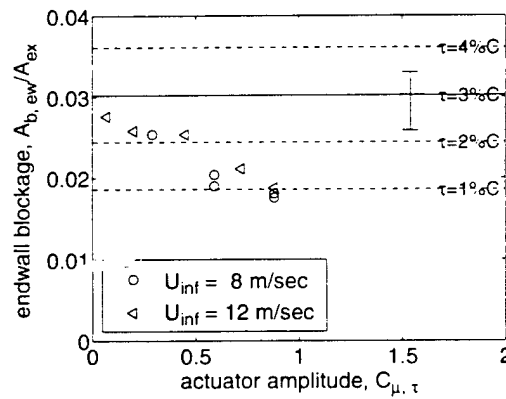


Figure 4.6 Endwall blockage vs. $C_{\mu\tau}$ of NSJ directly over blade tip. Data sets taken for two upstream velocities. $\tau = 3\%C$, $F_C^+ = 1.0$.

4.1.2 Dependence on Forcing Frequency of NSJ

The blockage reduction achieved with the use of NSJ exhibits considerable sensitivity to the forcing frequency as will be seen in the following. Thus we need to first identify/define the reduced frequency parameter that shows how the frequency sensitivity scales. This may indirectly provide the scale that characterizes the flow process which responds to NSJ actuation to results in blockage reduction. It was originally suggested that the observed reduction in blockage is associated with the instability of the shear

layer developed at the blade tip as in the mixing enhancement of two-dimensional wall bounded jets (Katz *et al.* [4.6] and Tsuji *et al.* [4.7]). If that is the case, the frequency should scale with the height of the wall jet or the tip clearance size τ . Figure 4.7 shows the frequency response of the endwall blockage taken with NSJ actuator acting over the vortex core. There are two data sets with two tip clearance sizes. The horizontal lines are the baseline blockages without actuation at each clearance (*i.e.* no actuation on tip clearance flow) determined from Figure 3.5 using least-square fit. In Figure 4.7(a), the tip clearance size τ is used to non-dimensionalize the forcing frequency as follows:

$$\beta_\tau = \frac{2\pi f \tau}{U_\infty}$$

The blockage is the most responsive when forced at $\beta_\tau = 0.05 - 0.25$. However, the troughs of the endwall blockage for the two data sets do not line up vertically as indicated with the dashed line implying that the flow mechanism is not related to the shear layer instability. In Figure 4.7(b), the blade chord length C is used instead of τ to non-dimensionalize the forcing frequency as follows**:

$$F_C^+ = \frac{fC}{U_\infty}$$

The blockage is the most responsive when forced at a reduced frequency F_C^+ of about 0.75. Now, the troughs of the endwall blockage for the two data sets are nearly lined up vertically.

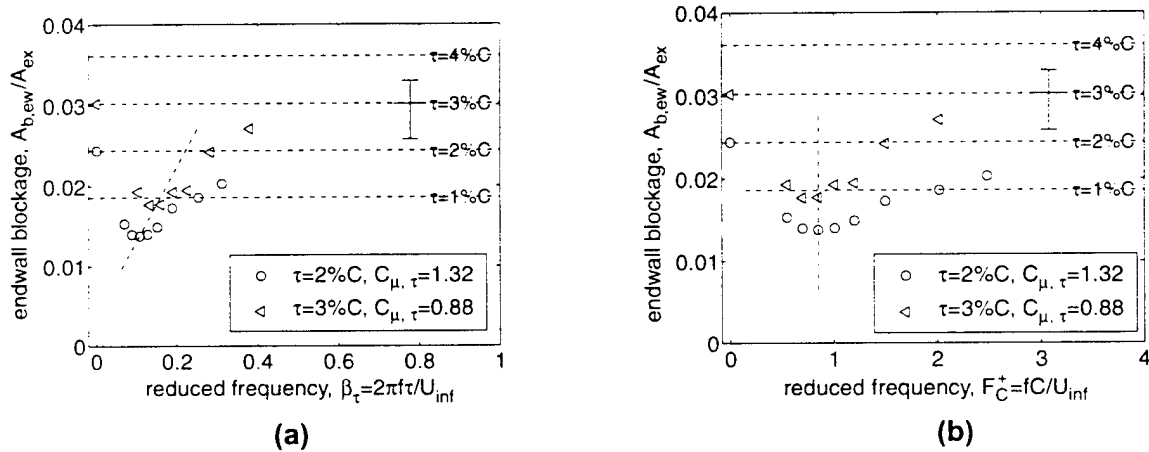


Figure 4.7 Frequency dependence of blockage reduction with NSJ actuator over vortex core: (a) using clearance size τ ; (b) using blade chord C as length scale.

Figure 4.8 shows similar data sets taken with the NSJ actuator acting directly over the blade tip. The data is taken for three tip clearances. Again, the blockage troughs line up vertically at a reduced frequency F_C^+ of about 1.0 when the blade chord length is used to non-dimensionalize the forcing frequency.

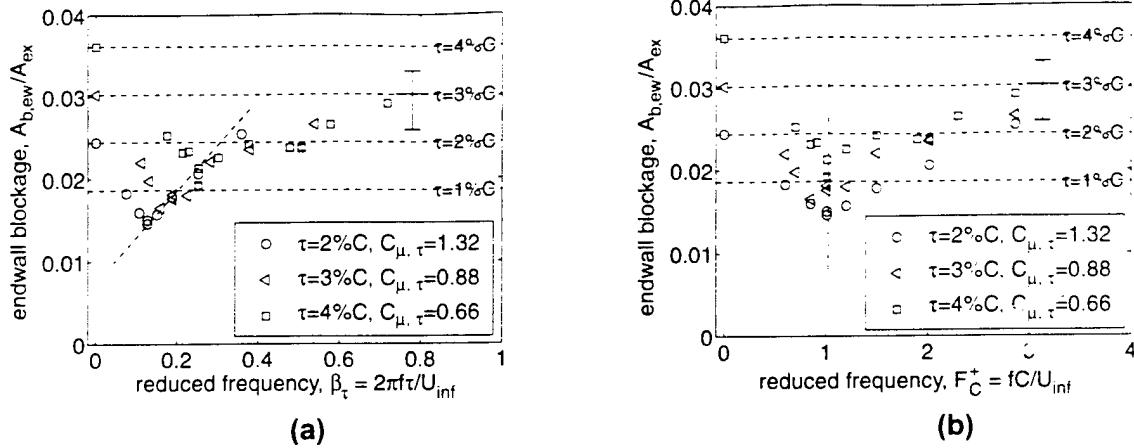


Figure 4.8 Frequency dependence of blockage reduction with NSJ actuator over blade tip: (a) using clearance size τ ; (b) using blade chord C as length scale.

Unlike the tip clearance size, the blade chord length has not been varied to determine its relevance in defining F_C^+ . Therefore, a model-based approach is taken to justify the use of blade chord as the length scale and to explain the flow mechanism that results in the blockage reduction. This will be presented in the next section, namely Section 5.

4.1.3 Dependence on Pitchwise Location of NSJ

As was mentioned in Section 2, the casing wall with the actuator is adjustable in the pitchwise direction. The survey of the total pressure loss coefficient is carried out with various pitchwise NSJ slit locations. Figure 4.9 shows the dependence of the blockage reduction on the pitchwise location of the NSJ actuator. The data in Figure 4.9 are with 3% C clearance and the baseline blockage without actuation is indicated with a solid horizontal line. The locations of the blades are indicated in the bottom of the figure. There are two pitchwise locations where the actuation has the greatest effect on the blockage: one right over the blade tip and the other over the vortex core. The tip clearance-related blockage is reduced by about 66%, which is equivalent to the baseline case with 1% C clearance. Note that the actuator amplitude and frequency are fixed at $C_{\mu, \tau} = 0.88$ and $F_C^+ = 1.0$. The bulk flow process responsible for the blockage reduction will be discussed in subsection 4.1.6.

** The factor of 2π only appears in the definition of β_τ . The above definition of β_τ is typically used in the wall jet stability community, while that of F_C^+ is in the flow separation control community.

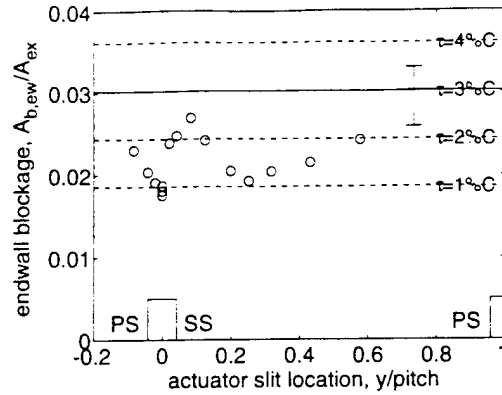


Figure 4.9 Endwall blockage vs. pitchwise location of NSJ actuator. $C_{\mu} \tau = 0.88$ and $F_c^* = 1.0$.

Total pressure loss coefficients with various pitchwise locations of the NSJ are shown in Figure 4.10. Figure 4.10(a) shows that the mass-average loss increases with actuation compared to the baseline (the solid horizontal line) except for the data with the actuator over the blade tip where it remains more or less the same. The mass-average loss is largest at around 0.25 *pitch* where the blockage reduction is locally largest as shown in Figure 4.9. Figure 4.10(b) shows the stream thrust-average (i.e. mixed out) loss vs. the pitchwise location of the NSJ actuator. The stream thrust-average loss remains more or less the same as the baseline when the actuator is away from the blade tip. However, when the actuator is right over the blade, the tip clearance-related stream thrust-average loss is reduced by about 33% so that it is the same as the baseline case with 2%C clearance.

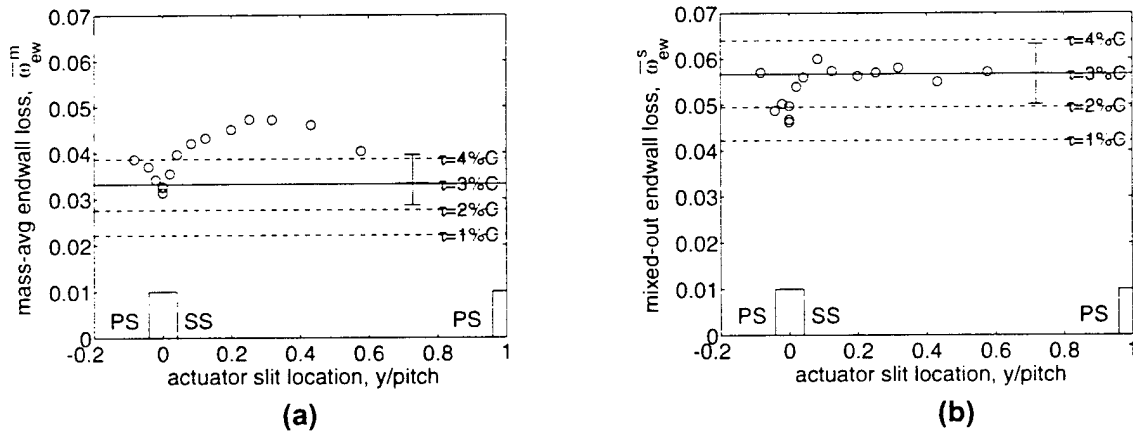


Figure 4.10 Endwall total pressure loss coefficient vs. pitchwise location of NSJ actuator: (a) mass-average ω ; (b) stream thrust-average (or fully mixed-out) ω

4.1.4 Contribution of Each NSJ Actuator

As mentioned earlier, there are three independent NSJ actuators inline as shown in Figure 2.2 and Figure 2.4. The endwall blockage has been measured with one NSJ actuator at a time to examine the contribution of each actuator^{††}, *i.e.* to study whether there is an axial location wherein the NSJ actuation is more effective. Figure 4.11 shows the endwall blockage plotted against the actuator amplitude. None of the three actuators has dominance and the blockage reduction with one actuator is almost the same regardless of the actuator. The amount of the blockage reduction is nearly the same as the case with all three actuators at the same total $C_{\mu \tau}$, although the actuation jet velocities are different. This result points out again the relevance of $C_{\mu \tau}$ in the blockage reduction with the use of NSJ.

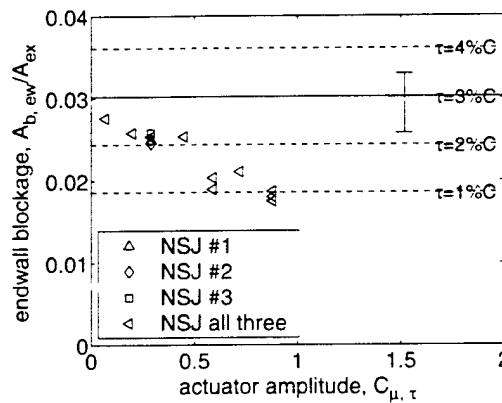


Figure 4.11 Contribution of each NSJ actuator placed directly over blade tip. All data taken at $F_C^+ = 1.0$.

4.1.5 Flow Visualization

The Reynolds number for the flow visualization is set at $Re_C = 80,000$ ($U_\infty = 6\text{m/s}$), which is the minimum Reynolds number without massive laminar separation on the blade suction surface as shown in Figure 3.1(b). Detailed description of the setup for the visualization is in subsection 2.2.3. The primary interest is again to assess whether there is a change in the level of mixing between the leakage jet and the main flow as a result of the NSJ actuation. Two of the resulting images are shown in Figure 4.12. The top of each image is the casing wall and the left-hand side is the suction surface of the blade. Each pixel in the digitized image has an intensity I which spans from 0 (white) to 1 (black or smoke). The contour lines of I are computer-processed and plotted on top of the images. Figure 4.12(a) is the baseline image without actuation. The leakage jet comes in from the clearance gap in the upper-left corner rolling up into a vortex. Most of the smoke is collected in the core region of the vortex. Figure 4.12(b) is with actuation

^{††} The NSJ near L.E. is NSJ #1, and the next one downstream is NSJ #2, and so on.

over blade tip at $F_C^- = 1.0$ and $C_{\mu} \tau = 0.88$. Note that the forcing frequency is the optimum for the blockage reduction as shown in Figure 4.8(b). The smoke is spread out into a relatively more uniform state compared to that of the baseline in Figure 4.12(a); this has the implication that NSJ actuation promotes mixing between the smoke-tagged leakage flow (black) and the untagged blade passage flow (white).

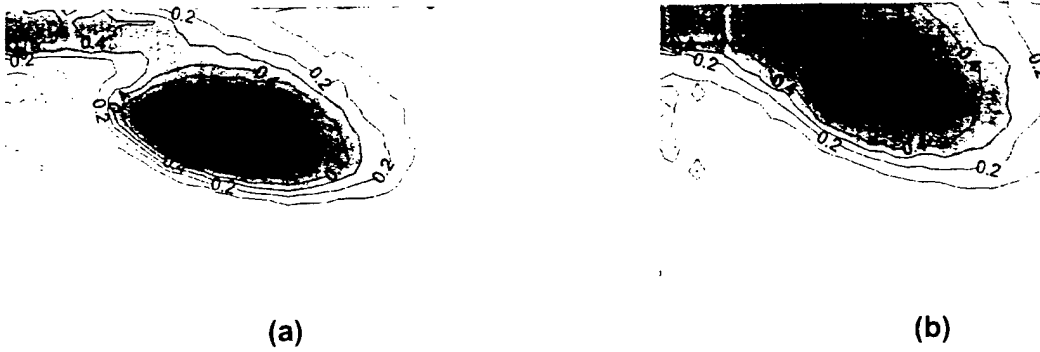


Figure 4.12 Images from flow visualization and computer-processed intensity contour lines: (a) baseline without actuation ($\tau = 3\%C$); (b) with NSJ actuation over blade tip ($F_C^- = 1.0$ and $C_{\mu} \tau = 0.88$).

The intensity in the image is an indication of the concentration of the smoke particles. Since the mass diffusion per unit area is proportional to the concentration gradient, the average magnitude of the concentration (or the intensity in the image) gradient is a good measure of the level of diffusion and hence the level of mixing. The intensity gradient would become zero, if the smoke (or the leakage flow) were fully mixed with the core flow. To quantitatively compare the relative level of mixing at three forcing frequencies, the gradients of the intensity have been processed and the average of their magnitudes are plotted against the forcing frequency as shown in Figure 4.13. The average magnitude of the gradient $\overline{(|\nabla I|)}$ has a dependence on the forcing frequency with the smallest $\overline{(|\nabla I|)}$ at $F_C^- = 1.0$ among three forcing frequencies tested. Although the average intensity \bar{I} of each image is within $\pm 2\%$, there exists up to 30% reduction in $\overline{(|\nabla I|)}$, implying that the mixing is indeed enhanced with the actuation and is greatest approximately at $F_C^- = 1.0$. The enhanced mixing between the low momentum flow in the vortex core and the high momentum flow in the blade passage reduces the streamwise velocity non-uniformity, which worsens with increasing adverse pressure gradient.

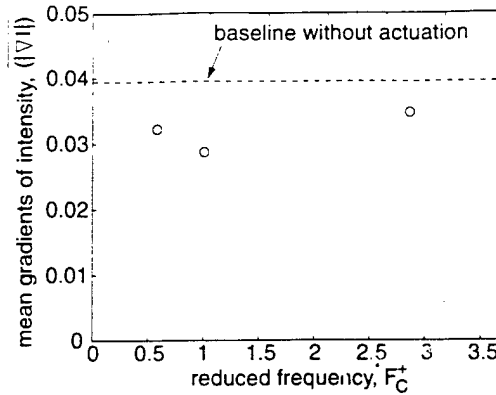


Figure 4.13 Average magnitude of gradients of intensity in flow visualization images indicating mixing level.

4.1.6 Bulk Flow Process Associated with NSJ Actuation

There are two possible bulk flow processes associated with the NSJ actuation responsible for the reduction in the tip clearance-related blockage: leakage flow reduction and mixing enhancement. The strong dependence of the blockage reduction on the forcing frequency excludes the momentum injection as a source because the same time-average momentum results in almost no change in the blockage at frequencies far away from the optimum as shown in Figure 4.7 and Figure 4.8. Since the NSJ actuation does not change the leakage flow rate when placed away from the blade tip (Kang *et al.* [4.8]), the blockage reduction with the actuator over the vortex core is attributed to the mixing enhancement, which decreases the non-uniformity created by the leakage flow. The mixing enhancement shortens the distance required for the flow to become uniform (or fully mixed-out). Consequently, it increases the mass-average loss but not the stream thrust-average loss as the measurement indicates in Figure 4.10.

The blockage reduction with the NSJ actuator over the blade tip is not as straightforward and is a combination of the two flow processes. As observed by Kang *et al.* [4.8] the NSJ actuator can reduce the amount of the leakage flow for a given pressure difference across the blade when it is placed right over the blade tip. One can indirectly quantify the reduction in the leakage flow rate in the cascade experiment from the stream thrust-average loss measurements shown in Figure 4.10(b). As discussed above the mixing enhancement does not change the stream thrust-average loss. The reduction in the stream thrust-average loss with NSJ actuator over the blade tip is thus attributed to the reduction in the leakage flow rate. The analytical model validated against detailed measurements and CFD by Storer and Cumpsty [4.9] suggests that for a fixed mid-span loading the tip clearance-related loss increases linearly with the leakage flow rate. Therefore, the 33% reduction in the tip clearance-related stream thrust-average loss shown in Figure 4.10(b) leads one to conclude that the leakage flow rate is reduced by about 33% due to the NSJ actuation over the blade tip. The 33% reduction in the leakage flow rate results in a 33% reduction of tip

clearance-related blockage and loss, which are proportional to the leakage flow rate, as summarized in the second row of Table 4.1. About half of the blockage reduction is due to the leakage flow reduction.

As described in subsection 4.1.5 on flow visualization, the NSJ actuator over the blade tip brings about the mixing enhancement as well. Therefore, the other half of the blockage reduction is attributed to the mixing enhancement that increases the mass-average loss while maintaining the same stream thrust-average loss as summarized in the third row of Table 4.1. The net effects of the two flow processes on the tip clearance-related blockage, mass-average, and stream thrust-average losses are listed in the last row whereby the blockage and loss measurements with the NSJ actuator over the blade tip (Figure 4.9 and Figure 4.10) are all explained. Note that the net effect on the mass-average loss remains the same as a result of the compensating effect of the tip leakage flow reduction and the mixing enhancement. In summary, both the leakage flow reduction and the mixing enhancement are responsible for the reduction in blockage with NSJ actuator right over the blade tip (along the camberline of the blade), and their contributions are about the same.

Table 4.1 Effects of each flow process and their combined effects on tip clearance-related blockage and loss explaining observations with NSJ actuator over blade tip.

	Blockage	Mass-average loss	Stream thrust-average loss
Leakage flow reduction	↓ Decrease by 33%	↓ Decrease by 33%	↓ Decrease by 33%
Mixing enhancement	↓ Decrease by 33%	↑ Increase by 33%	– Same
Net effect	↓↓ Decrease by 66%	– Same	↓ Decrease by 33%

4.2 Directed Synthetic Jet Actuator

Discussions on the DSJ actuation are presented in this section. Figure 4.14 shows a representative result of DSJ actuation compared with the baseline. The DSJ also brings about substantial changes in the endwall flow as shown in Figure 4.14(b). The exit static pressure measurements indicate an increase in $C_{p,ex}$ with DSJ as shown in Figure 4.15. Again due to the large uncertainty in the measurement, it only provides a qualitative comparison.

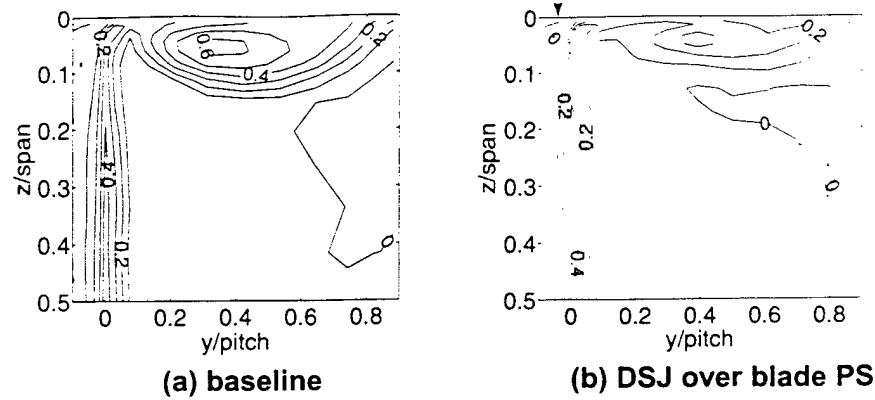


Figure 4.14 Contours of ω measured 5% C downstream of T.E. plane: (a) baseline without actuation, $\tau = 3\%C$; (b) DSJ directly over blade PS (-0.04 pitch), $C_{\mu} \tau = 0.88$, $F_c^+ = 1.0$. Arrows indicate locations of DSJ holes.

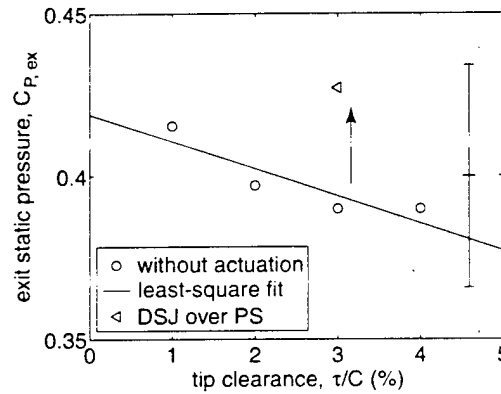


Figure 4.15 Exit static pressure with and without NSJ actuation. \triangle : DSJ directly over blade PS (-0.04 pitch), $C_{\mu} \tau = 0.88$, $F_c^+ = 1.0$.

As in the case of experiments exploring the use of NSJ, the dependence on the amplitude, frequency, and pitchwise location of the DSJ actuator, and the contribution of each actuator (there are three actuators inline as shown in Figure 2.2 and Figure 2.4) are determined and discussed in this section. We also compare the use of SDJ against using DSJ to determine if the unsteady actuations associated with DSJ play any role at all, *i.e.* to find out if steady injection of momentum with the same time-average value as that from DSJ yields similar benefit.

4.2.1 Dependence on Amplitude of DSJ

The response of the endwall blockage against the actuator amplitude is shown in Figure 4.16 for the case where the DSJ actuator is placed near PS of the blade (-0.04 pitch) and for the situation where the NSJ actuator is placed near the vortex core. The forcing frequency is $F_c^+ = 1.0$ for both. Note that the DSJ

actuator is about twice as effective as the NSJ actuator in reducing the endwall blockage for a given amplitude $C_{\mu, \tau}$ and the DSJ actuation has the potential to eliminate most of the endwall blockage – not only the endwall blockage associated with the tip clearance but also that associated with the endwall boundary layer. Therefore, the DSJ is more effective than the NSJ in reducing the endwall blockage.

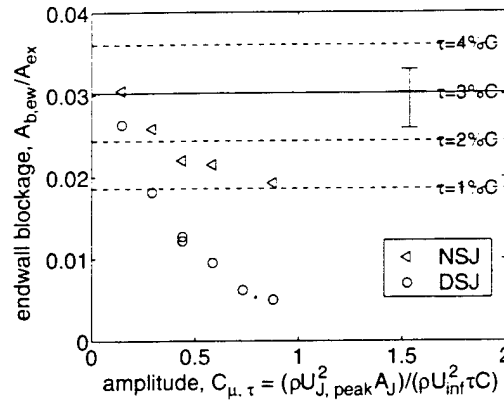


Figure 4.16 Comparison between DSJ (placed near pressure surface of blade) and NSJ (placed near vortex core). $\tau = 3\%C$. Both actuators at $F_C^+ = 1.0$.

4.2.2 Dependence on Forcing Frequency of DSJ

As shown in Figure 4.17, the blockage reduction with DSJ is not as sensitive to the frequency as is the case with the NSJ. The variations in the data taken at two Reynolds numbers are not larger than the measurement uncertainty interval and there is no significant trend in the frequency response. It suggests that the change in the flow process with the use of the DSJ is different from that of the NSJ, which exhibits strong sensitivity to the forcing frequency. It appears that the time-average momentum is more important than the unsteadiness in reducing the blockage with the use of the DSJ. More details on the flow process will be discussed further in subsection 4.2.5.

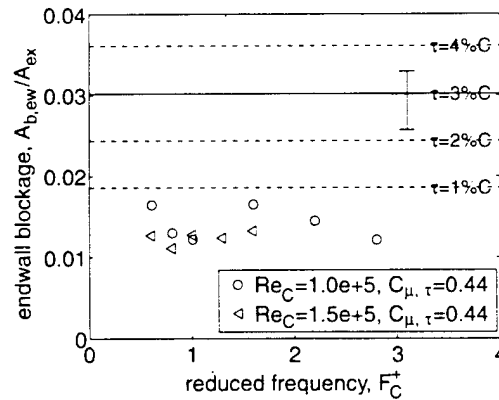


Figure 4.17 Frequency dependence of blockage reduction with DSJ over pressure surface of blade. $\tau = 3\%C$.

4.2.3 Dependence on Pitchwise Location of DSJ

Figure 4.18 shows the endwall blockage vs. the pitchwise location of the DSJ actuator. The actuator frequency and the amplitude are fixed at $F_C^+ = 1.0$ and $C_{\mu, \tau} = 0.88$. A substantial reduction in the endwall blockage is achieved when the DSJ are located near PS of the blade (-0.04 *pitch*) or the tip clearance vortex core.

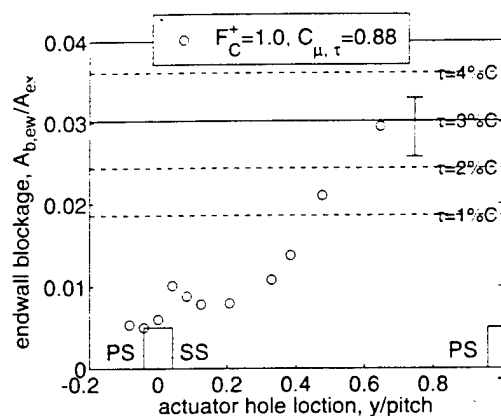


Figure 4.18 Endwall blockage vs. pitchwise location of DSJ actuator.

Figure 4.19 shows mass-average and stream thrust-average total pressure loss coefficients. Unlike NSJ, the DSJ reduces both of them significantly from the baseline with DSJ located from -0.08 *pitch* to about 0.5 *pitch*.

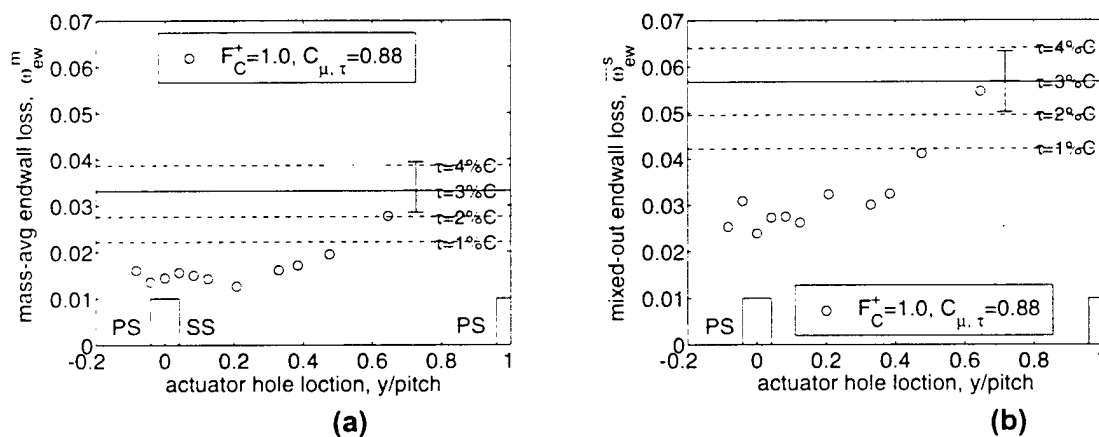


Figure 4.19 Endwall total pressure loss coefficient vs. pitchwise location of DSJ actuator: (a) mass-average ω ; (b) stream thrust-average (or fully mixed-out) ω

4.2.4 Contribution of Each DSJ Actuator

As with the use of NSJ, the endwall blockage has been measured with one DSJ actuator at a time to examine the contribution of each actuator. Figure 4.20 shows the endwall blockage plotted against the

actuator amplitude. None of the three DSJ actuators has dominance and the blockage reduction with one actuator is almost the same regardless of the actuator. The amount of the blockage reduction is nearly the same as the case with all three actuators at the same total $C_{\mu} \tau$, which is 0.29. The individual operation of DSJ essentially shows the same result as that of NSJ.

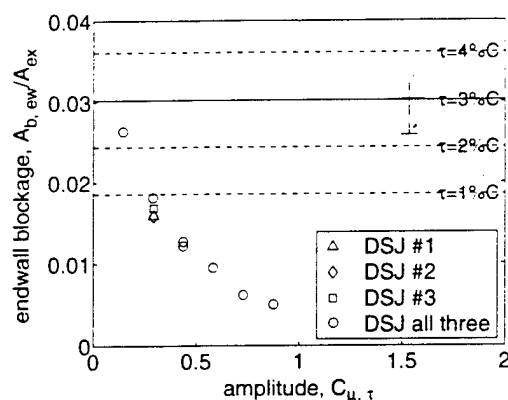


Figure 4.20 Contribution of each DSJ actuator placed over blade PS. $F_c^+ = 1.0$.

4.2.5 Comparison between DSJ and SDJ

The measurements with the DSJ actuation presented above have revealed two aspects, which support the hypothesis (or the intention of DSJ) that the momentum injection is mainly responsible for the observed blockage reduction with the use of DSJ. The first is that the blockage reduction is not sensitive to the actuation frequency and the second is that the DSJ reduces both blockage and loss in the endwall region. SDJ (Steady Directed Jet) experiments have been carried out to confirm the hypothesis by proving that it is the time-average momentum of the directed jet that determines the amount of the blockage reduction. Figure 4.21 shows the comparison between DSJ and SDJ. Note that $C_{\mu} \tau$ of the DSJ has been time-averaged as shown in Figure 2.9(b). The data collapses onto a single curve verifying that the time-average $C_{\mu} \tau$ is important and the unsteadiness is not in reducing the blockage.

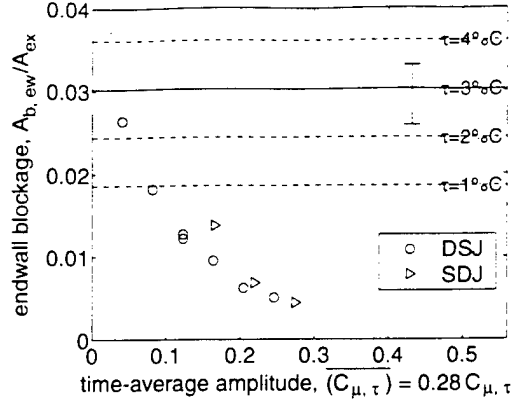


Figure 4.21 Comparison between DSJ and SDJ (Steady Directed Jet). Holes of both actuators placed over pressure surface of blade. $\tau = 3\%C$. DSJ at $F_c^+ = 1.0$.

4.2.6 Return on Actuator Flow Power

As presented above, all three actuators (NSJ, DSJ, and SDJ) are capable of mitigating the endwall blockage associated with tip leakage flow. In other words, all of them can enhance the pressure rise capability or the performance. Another important aspect of the tip leakage flow is again the loss that it incurs. The NSJ actuation appears not to have reduced the mass-average total pressure loss as measured 5%*C* downstream of T.E. plane, while the DSJ and SDJ does. To determine whether the reduction in endwall loss with the use of directed jets results in an improvement of the overall efficiency, the reduction in the endwall flow power deficit should be compared with the flow power added by the actuator. The endwall flow power deficit is:

$$\Pi_{deficit} = \frac{\dot{m}_{in}}{\rho} (P_{t,\infty} - \bar{P}_t^m) = \frac{\dot{m}_{in} q_\infty \bar{\omega}_{ew}^m}{\rho} = Q_{in} q_\infty \bar{\omega}_{ew}^m = U_\infty \cos \beta_{in} \frac{h_s}{2} q_\infty \bar{\omega}_{ew}^m$$

and the flow power added by the directed jets is:

$$\Pi_J = \overline{(Q_J q_J)} = \frac{1}{2} \rho A_J \bar{U_J^3} = \frac{1}{2} \rho A_J (0.26 \times U_{J,peak}^3)$$

The power added by the DSJ needs to be time-averaged as shown above. The factor of 0.26 in the above equation is from the time-averaging of the DSJ injection cycle (similar to that in Figure 2.9). Now the return on flow power added by the actuation, η_J is:

$$\eta_J = \frac{\Delta \Pi_{deficit}}{\Pi_J} \times 100 = \frac{(\Pi_{deficit})_{baseline} - (\Pi_{deficit})_{control}}{\Pi_J} \times 100 (\%)$$

Figure 4.22 shows the values of η_J for DSJ and SDJ at $\bar{C}_{\mu,\tau} = 0.25$. Only about 15% of the flow power added by the DSJ is utilized, while about 30% of the flow power added by the SDJ is utilized in increasing the flow power measured 5%*C* downstream of the T.E. plane (or equivalently in reducing the mass-average total pressure loss) and the remainder is lost. The difference in η_J of DSJ and SDJ is

because the flow power scales with the cube of the jet velocity. The cyclic DSJ has a peak jet velocity that is about twice the steady jet velocity for the same time-average momentum coefficient. The amount of the reduction in $\Pi_{deficit}$ is the same for both the DSJ and the SDJ at given time-average momentum coefficient. Therefore, a higher Π_j of DSJ for the same $\Delta\Pi_{deficit}$ results in a lower η_j compared to SDJ.

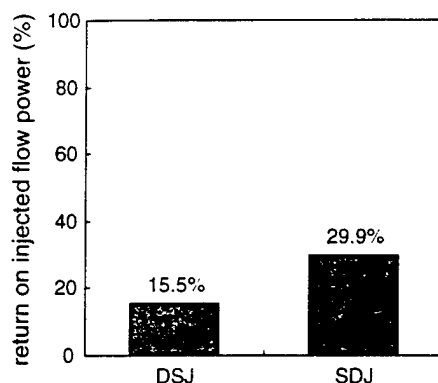


Figure 4.22 Return on injected flow power of directed jet actuation at $\bar{C}_{\mu,\tau} = 0.25$.

Even for SDJ, η_j is unsatisfactorily low, when compared to the boundary layer separation control wherein active control achieves about 1600% return on the input electrical power to the actuator [4.2]. In other words, the actuation benefits from great leverage in boundary layer separation control. The return on invested power that is well below 100% in the current tip leakage flow control suggests that there is no amplified benefit of which one can take advantage of at least with the schemes considered in this study. Therefore, one can only try to minimize the loss of the injected flow power to raise η_j close to 100% – hence minimizing the penalty in overall efficiency with the use of actuation – while achieving the reduction in the flow blockage. Let's examine why the return on injected flow power is so low with the use of directed jets. Part of the loss is due to the relative angle between the directed jet and the main flow. Assuming the component of the jet normal to the main flow is completely lost, the component in the main flow direction or the usage of the jet decreases with the relative angle as shown in Figure 4.23(a). The directed jet is inclined by 25° relative to the casing wall as shown in Figure 2.4. Assuming a relative angle of 30° , only about 13% of the flow power is lost, which yields η_j of 87% implying that the relative angle is not the major source of the flow power loss of the directed jets. Another source of the loss is in the mixing process of the high velocity jet with the passage flow. At $\bar{C}_{\mu,\tau}$ of 0.25, for example, $U_{j, peak}$ of DSJ is about 6.3 times U_∞ and U_j of SDJ is about 3.4 times U_∞ . Loss that incurs due to the mixing between two streams of flow with different magnitude of the velocities can be estimated using a simple control volume analysis. The control volume analysis assumes a fully mixed-out condition at the outlet and hence gives the upper bound of the mixing loss that can incur. As shown in Figure 4.14(b), the total pressure

survey near the blade exit plane illustrates that the high velocity or high total pressure jet mixes almost completely with the low total pressure endwall flow by the time it reaches the blade exit plane – there is no region of negative ω – implying that the assumption of fully mixed-out condition is reasonable. The return on injected flow power predicted by the model is plotted against the velocity ratio between the jet and the incoming flow as shown in Figure 4.23(b). The momentum coefficient is fixed while the magnitude of the jet velocity is varied in the analysis. Note that η_j decreases quickly from 100% as the velocity ratio increases from 1.0. The velocity ratio between the jet and the low momentum endwall flow that mixes with it is obviously larger than the velocity ratio between the jet and the far upstream flow. With a velocity ratio of 7.0, η_j is only about 25% and the remaining 75% of the flow power is lost in the mixing process explaining most of the observed loss in the injected flow power shown in Figure 4.22.

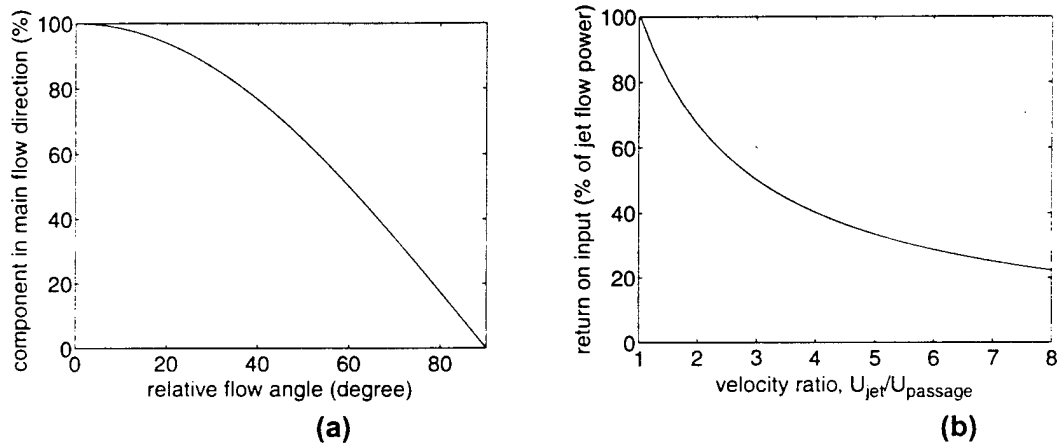


Figure 4.23 Predicted return on actuator input: (a) as function of relative angle between jet and main flow; (b) as function of velocity ratio for fixed momentum injection.

Now it is clear that one can increase the efficiency of the actuation while reducing the blockage by aligning the jet in the streamwise direction and keeping the velocity ratio as low as possible but above one. In other words, for given time-average momentum coefficient, both the direction and the magnitude of the injected jet velocity are very important. The DSJ and SDJ used in the current study may not have been the optimal actuators that one can design; thus this aspect will need to be re-examined.

4.3 Summary

In this section, time-average effects of three types of actuators (namely NSJ, DSJ, and SDJ) on the tip clearance-related blockage and loss have been discussed along with the bulk flow processes responsible for the observed changes in the blockage and loss. The key points made in this section are as follows:

- Use of NSJ (Normal Synthetic Jets) at locations that are directly over the blade tip and tip clearance vortex core is effective in reducing the flow blockage associated with tip clearance flow when actuated at the optimum reduced frequency, whose scaling will be elaborated in Section 5.
- The effect of NSJ on mass-average loss measured near the blade trailing edge plane is minimal with the actuation directly above the blade tip region and increases at other pitchwise locations with the largest increase when the actuation is over the tip clearance vortex core.
- It has been deduced based on the blockage and loss measurements in conjunction with the analysis of flow visualization images that the reduction in blockage is associated with mixing enhancement and tip leakage flow reduction when the NSJ is over the blade tip while it is associated with mixing enhancement only when the NSJ is over the tip clearance vortex core.
- Use of DSJ (Directed Synthetic Jets) is effective in reducing not only the tip clearance-related blockage but also loss. The result is rather insensitive to the frequency compared to the situation with the use of NSJ.
- For a given actuation amplitude (momentum coefficient), DSJ is about twice as effective as NSJ in reducing tip clearance-related blockage.
- It has been concluded that the reduction of tip clearance-related blockage and loss with the use of DSJ is associated with time-average streamwise momentum injection based on the following observations: (1) the blockage reduction is not sensitive to the forcing frequency and (2) the use of SDJ (Steady Directed Jets) demonstrates the same amount of blockage reduction when SDJ momentum coefficient and the DSJ time-average momentum coefficient are the same.
- Only about 15% (for DSJ) to 30% (for SDJ) of the flow power added by directed jet actuation is utilized in reducing the mass-average loss measured near the T.E. plane and the rests are lost mainly due to the mixing process of the high velocity jets – about six (for DSJ) to three (for SDJ) times the far upstream reference velocity.

The above summary implies that the mixing enhancement and the leakage flow reduction schemes with the use of NSJ are not cost effective and it may not be worthy of any further pursuit. The streamwise momentum injection with the use of SDJ is more effective than the above two schemes and should be further explored for potential in not only mitigating the effect of tip clearance flow on performance at design but also on compressor stability while minimizing penalty on efficiency.

References

- [4.1] Lorber, P. F., McCormick, D. C., Anderson, T. J., Wake, B. E., MacMartin, D. G., Pollack, M. J., Corke, T. C., and Breuer, K. S., "Rotorcraft Retreating Blade Stall Control", AIAA 2000-2475, 2000.

- [4.2] McCormick, D. C., "Boundary Layer Separation Control with Directed Synthetic Jets", AIAA 2000-0519.
- [4.3] Seifert, A., Bachar, T., Koss, D., Shepshelovich, M., and Wygnanski, I., "Oscillatory Blowing: A Tool to Delay Boundary-Layer Separation", AIAA 93-0440, 1993.
- [4.4] Rains, D. A., "Tip Clearance Flows in Axial Flow Compressors and Pumps", California Institute of Technology, Hydrodynamics and Mechanical Engineering Laboratories, Report No. 5, 1954.
- [4.5] Storer, J. A. and Cumpsty, N. A., "Tip Leakage Flow in Axial Compressors", ASME Paper No. 90-GT-127, 1990.
- [4.6] Katz, Y., Horev, E., and Wygnanski, I., "The Forced Turbulent Wall Jet", J. Fluid Mech., vol. 242, pp. 577-609, 1992.
- [4.7] Tsuji, Y., Morikawa, Y., Nagatani, T., and Sakou, M., "The Stability of a Two-dimensional Wall Jet", Aeronautical Quarterly, XXVIII, pp. 235-246, November 1977.
- [4.8] Kang, E., Breuer, K. S., and Tan, C. S., "Control of Leakage Flows Using Periodic Excitations", AIAA 2000-2232, 2000.
- [4.9] Storer, J. A. and Cumpsty, N. A., "An Approximate Analysis and Prediction Method for Tip Clearance Loss in Axial Compressors", ASME Paper No. 93-GT-140.

5 Unsteadiness in Tip Clearance Vortex

5.1 Introduction

As was described and discussed in Section 4.0, there exists an optimum frequency for the blockage reduction with the use of NSJ actuation, which scales with upstream velocity but not with tip clearance size. On a tentative basis, blade chord length was used as a length scale. The bulk flow process identified in the previous chapter is that the mixing between the low streamwise momentum flow in the vortex core and the high momentum main flow is promoted when the NSJ is operated at the optimum frequency. What has not been discussed is why the mixing enhancement takes place at that frequency and what sets the frequency. Increased mixing is a result of increased momentum transport/transfer, and the increase can be attributed to unsteadiness in the flow. In other words, the sensitivity of the blockage reduction to the forcing frequency is because the tip clearance vortex is more receptive at certain frequency than others resulting in higher unsteadiness and hence in enhanced mixing due to increased momentum transport/transfer. Therefore, one can hypothesize that there could be a natural frequency of the tip clearance vortex at which it is more receptive to NSJ actuation because of resonance. To test the hypothesis, time-resolved measurements have been taken using the hot-wire anemometer described in subsection 2.2.2. The time-resolved measurements are discussed in the following section. The issue of what sets this observed frequency is addressed by using a model-based approach, which is described in section 5.4.

5.2 Time-resolved Measurements

To examine the existence of a dominant frequency in the tip clearance vortex, time-resolved measurements have been taken using a hot-wire sensor placed $5\%C$ downstream of blade trailing edge plane. The RMS fluctuation level of the velocity trace measured near mid-span (i.e. far away from the vortex) is about two orders of magnitude smaller than that measured near the vortex core showing the presence of large unsteadiness in the vortex even without actuation. The RMS fluctuation level in the endwall region is about 25 – 40% of time-average value. The frequency content of the velocity trace measured near the vortex core does exhibit a peak. The peak in the frequency content is most identifiable in the data taken with the hot-wire sensor placed between the center of the vortex core and the casing wall. To examine how the frequency of the peak scales, the frequency contents of eight velocity traces taken with three clearances, two upstream velocities, and two hot-wire orientations are plotted against different normalizations of measured frequency. They are shown in Figure 5.1(a) – (c). The two upstream velocities create two peaks when plotted against dimensional frequency (as shown in Figure 5.1(a)) indicating that they need to be normalized by the upstream velocity. The peaks do not line up (or

collapse) when the tip clearance size is used as shown in Figure 5.1(b). When the chord is used instead, the peaks line up (or collapse) at around $F_C^- = 0.75$ as shown in Figure 5.1(c).

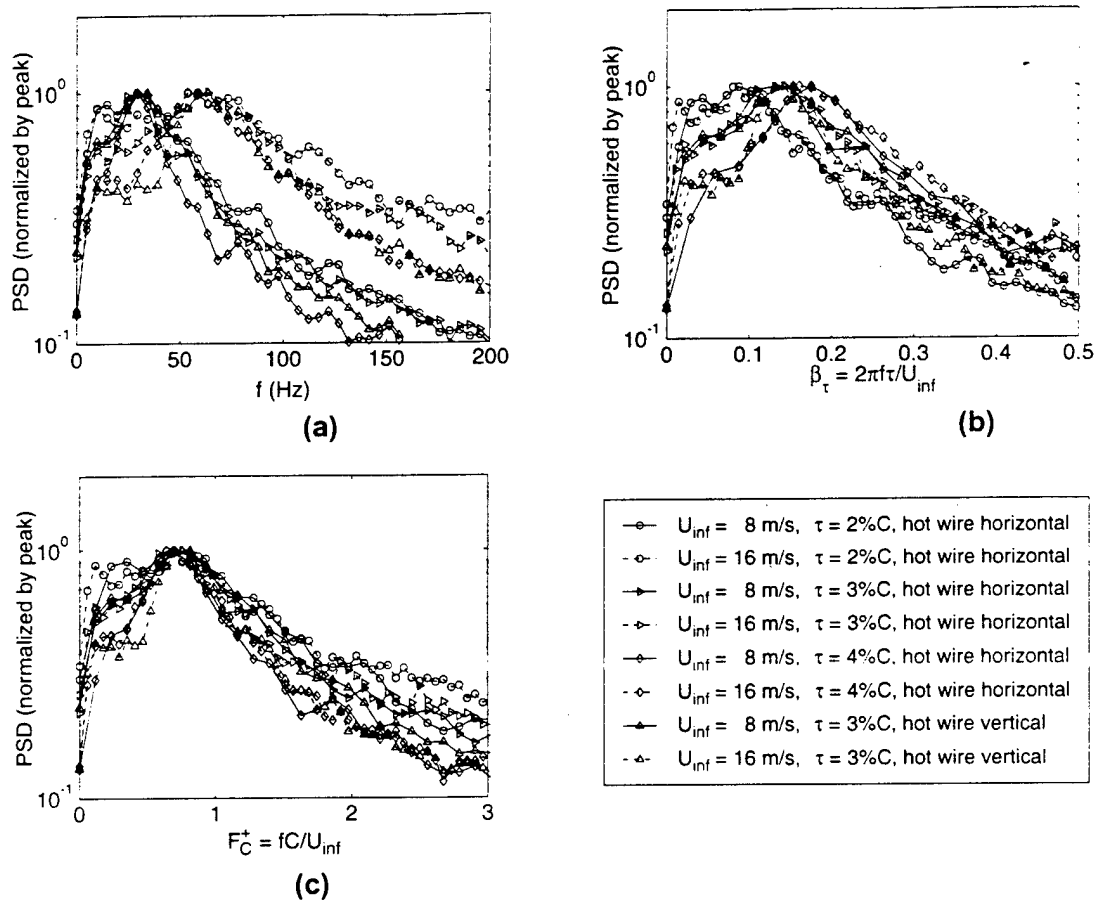


Figure 5.1 Frequency contents of velocity measured with hot-wire sensor placed $5\%C$ downstream of blade exit plane between center of vortex core and casing wall. Data taken without actuation.

To examine the response of the tip clearance vortex to NSJ actuation, hot-wire measurements have been taken near the blade exit plane with forcing. Figure 5.2 shows the responses measured at seven discrete forcing frequencies in both the endwall region and the mid-span region. There exists a strong response in the endwall region with a peak at around $F_C^- = 0.75$ showing that the effect of actuation is not limited to the clearance region. Note that the amplitude in the endwall region is a few orders of magnitude higher than that in mid-span region.

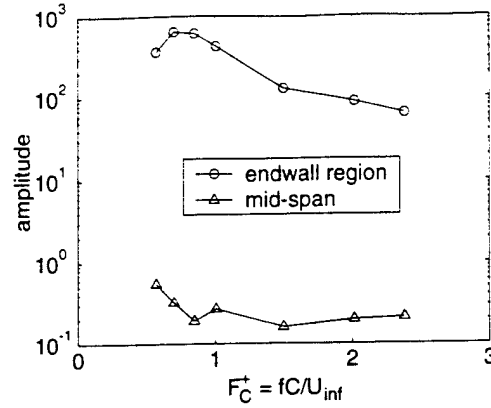


Figure 5.2 Forced response measured 5% C downstream of T.E. plane with NSJ over blade tip. $C_{\mu\tau} = 0.88$.

5.3 Vortex Instability

Before attempting to explain the source of this identifiable flow unsteadiness in the tip leakage vortex, we will first revisit the topic of Crow instability [5.1] associated with trailing vortices of wings. As a by-product of the lift generated by a finite wing, a pair of trailing vortices is created at wing tips to connect to the starting vortex. Their motions become visible either by moisture condensing in their cores or smoke generated near the wing tips. As shown in Figure 5.3, the trailing vortices usually exhibit a symmetric and nearly sinusoidal motion, until they dissipate eventually.



Figure 5.3 Instability of trailing vortices visualized by smoke [5.2]. View from chase airplane.

The theory by Crow [5.1] accounts for the instability during the early stages of the growth and predicts the most unstable (or rapidly growing) wavelength for given vortex core radius, R_c , and separation between the two vortices, b (See Figure 5.4). The analysis begins with the kinematic relation between vorticity and velocity in an incompressible fluid, namely the Biot-Savart law:

$$\vec{u}_n = \sum_{m=1}^2 \Gamma_m \int_{-\infty}^{\infty} \frac{d\vec{l}_m \times \vec{r}_{mn}}{4\pi |\vec{r}_{mn}|^3}$$

Vorticity-transport theorem combined with a couple of kinematic relations accounting for displacements close the dynamic problem resulting in a self-contained description of the vortices as they evolve in their induced field. Assuming solutions of exponential form:

$$\bar{r}(x, t) = \hat{r} \times e^{at + ikx}$$

and upon linearization, it becomes an eigenvalue problem. Now for a given wave number k , one can calculate a growth rate a . The wave number that corresponds to the maximum growth rate is the most rapidly growing mode. The corresponding wavelength $\lambda = 2\pi/k$ depends only on the radius of vortex core, R_c , and the separation, b .

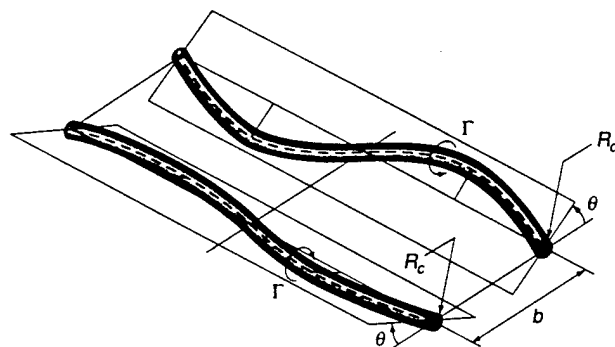


Figure 5.4 Schematic of trailing vortex instability.

Chevalier [5.2] carried out a series of flight tests with tip vortices visualized by smoke generated near wing tips as shown in Figure 5.3. One of his tests is a forced response test of the wing tip vortices by putting the airplane in a pitching motion at certain frequency. The optimum frequency to dissipate the trailing vortices was estimated by dividing the flight speed by the most unstable wavelength. The measured time for the trailing vortices to dissipate is plotted against the forcing frequency in Figure 5.5. The dissipation time is reduced by 50% when forced at the calculated optimum frequency. This experiment shows that the mixing of the wing tip trailing vortices can be enhanced substantially by forcing them at the optimum frequency.

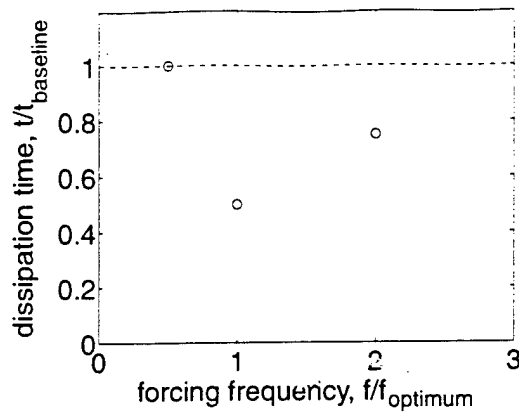


Figure 5.5 Dissipation time vs. forcing frequency of trailing vortices in flight test (data from Chevalier [5.2]).

5.4 Application to Tip Clearance Vortex

As shown in Figure 5.6, the casing wall creates a mirror image of the tip clearance vortex resulting in a similar configuration as the trailing vortices. Once the radius of vortex core R_c and the separation b are estimated, the Crow's instability analysis can be applied to this counter-rotating vortex pair to calculate the most rapidly growing wavelength.

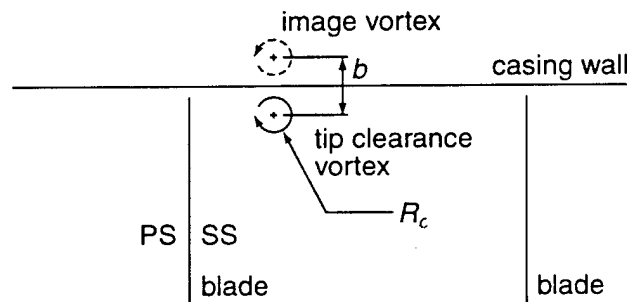


Figure 5.6 Schematic of tip clearance vortex and its image against casing wall creating a pair of counter-rotating vortices similar to trailing vortices.

There also exist other image vortices due to solid surfaces other than the casing wall. However, the image associated with the casing wall is considered since the separation distance of other image vortices are larger except near leading edge where the separation distance of the image associated with the blade surface is comparable to that of the one associated with the casing wall. As will be shown later, the instability or the peak in the frequency content does not develop until the vortex reaches near the blade exit plane. Therefore, the effect of the image associated with the blade surface is assumed to be less important than the one associated with the casing wall in predicting the instability and not considered in the following analysis.

The center of the tip clearance vortex is assumed to be located where the maximum total pressure loss coefficient is, which is marked as + in Figure 5.7. Crook [5.3] pointed out that based on his CFD simulations the low total pressure center locates the vortex center with an error that is considerably smaller than the distance between the vortex center and the casing wall even with a significant radial non-uniformity in the incoming total pressure profile. The separation distance, b is twice the distance between the center of vortex and the casing wall.

The radius of the vortex core R_c is estimated using a formula given by Rains [5.4], which is revisited in the following. As for slender bodies in external aerodynamics, he modeled the roll-up process of the tip clearance flow from the point of view of a two-dimensional unsteady flow. By assuming inviscid flow and a constant pressure difference along the chord, he computed the motion of the discontinuity surface or the sheet of vorticity as a function of non-dimensional time, t^* , which is

$$t^* = \frac{\chi}{\tau} \sqrt{(\Delta C_p)}$$

where χ is the streamwise distance and $\overline{(\Delta C_p)}$ is the chordwise average loading. The non-dimensional radius of the vortex core is a function of t^* only, i.e. $R_c^* = f(t^*)$. Numerical calculations showed that $f(t^*)$ is well approximated by $0.14(t^*)^{0.85}$ or

$$\frac{R_c}{\tau} = 0.14 \times \left(\frac{\chi}{\tau} \sqrt{(\Delta C_p)} \right)^{0.85}$$

Thus the radius of the vortex core becomes

$$R_c = 0.14 \times \chi^{0.85} \tau^{0.15} \overline{(\Delta C_p)}^{0.425}$$

To calculate R_c , χ is approximated by the distance along the chord and $\overline{(\Delta C_p)}$ is estimated near mid-span. The axial views of the resulting vortex core radii for three clearances are shown in Figure 5.7(a) – (c). The elongation in pitchwise direction is due to the relative angle between the vortex trajectory and the total pressure survey plane, which is assumed to be the same as the exit flow angle, 51.8°. The view angle does not skew the vortex core in spanwise direction as illustrated in Figure 5.7(b).

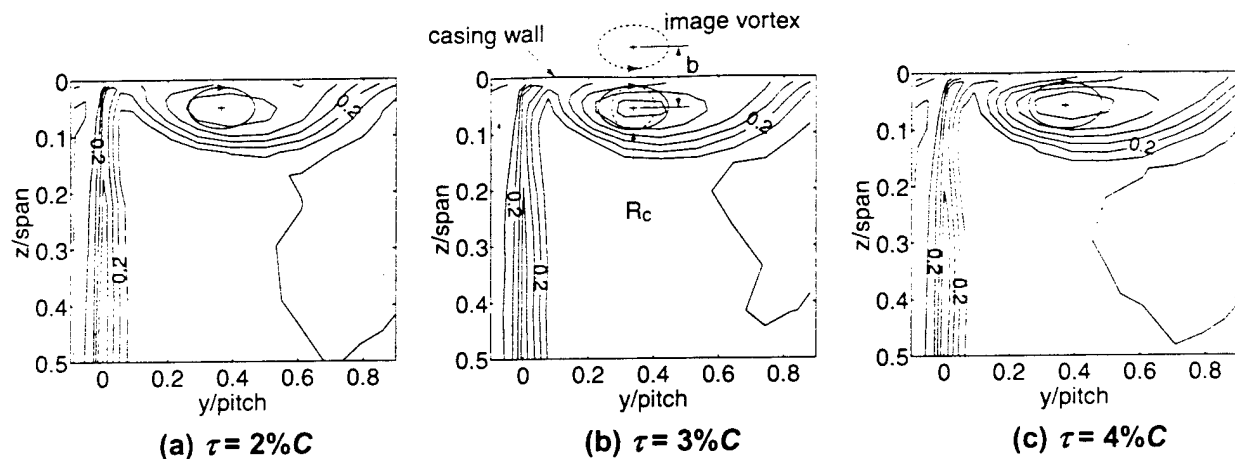


Figure 5.7 Tip clearance vortex core estimated using Rains [5.4] model and location of maximum loss coefficient. Total pressure loss coefficient contour measured near T.E. plane.

The Crow's instability analysis can now be applied to this counter-rotating vortex pair to calculate the most rapidly growing wavelength λ using R_c and b as inputs to the calculation. Figure 5.8 shows one of the resulting dispersion relations between non-dimensional wave number β and amplification rate α . The most rapidly growing wave number^{**} β_{max} , which is a function of the ratio R_c/b only, is determined as illustrated in Figure 5.8. The calculation is repeated for R_c/b ranging from 0 to 0.5 and the resulting relation between the most unstable wave number β_{max} and R_c/b is shown in Figure 5.9. R_c/b is estimated to be about 0.1 (Crow [5.1]) for trailing vortices behind an elliptically loaded wing, while it is estimated to be about 0.36 for the tip clearance vortex and its image associated with the casing wall of the current cascade. The theory cannot apply to vortices so thick that R_c/b is close to 0.5 as pointed out by Crow [5.1]. Although the value of R_c/b of the current cascade tip clearance vortex is higher than that of the trailing vortices by factor of 3.6 and therefore is closer to 0.5, it appears to be adequate for prediction of the instability associated with the tip clearance vortex of the current cascade.

^{**} The Crow's model predicts three modes: symmetric long wave, symmetric short wave, and asymmetric mode. The symmetric long wave is the physical mode that actually occurs. Therefore, the other two modes are not considered here.

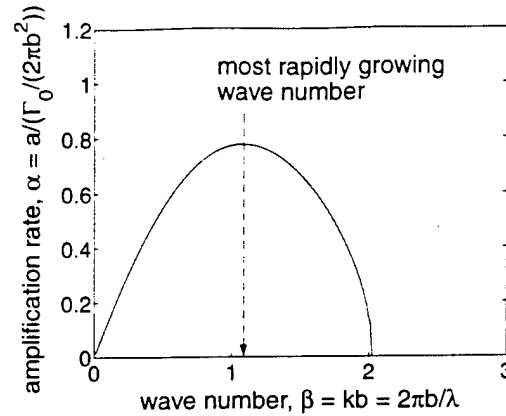


Figure 5.8 Amplification rate vs. wave number for $R_c/b = 0.36$.

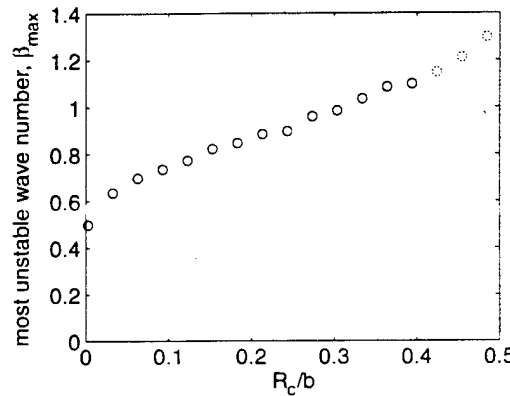


Figure 5.9 Most unstable wave number β_{max} predicted for fixed R_c/b .

Once the most rapidly growing wavelength is given, the characteristic frequency can be estimated by assuming that the wavy pattern convects downstream at a speed that is equal to the magnitude of the far upstream flow velocity (as the flight velocity was used in predicting the optimum frequency in Figure 5.5). The phase velocity divided by the wavelength gives the characteristic frequency. Thus, the most unstable frequency is:

$$f = U_{\infty} / \lambda.$$

The same steps are repeated for three tip clearance sizes (2%, 3%, and 4% C) and the resulting R_c/C and b/C are plotted on contours of the most rapidly growing wave length λ/C as shown in Figure 5.10. The characteristic wavelength is insensitive to the tip clearance size – both R_c/C and b/C are insensitive to the tip clearance size – and turns out to be almost the blade chord length for all three cases. The resulting characteristic frequencies for three clearances are compared with the measurements as shown in Figure 5.11. The predicted frequencies are close to the peaks of the measured power spectral density when

plotted in the same dimensionless frequency axis, and are also insensitive to the tip clearance size. *e.g.* F_C^+ decreases by only about 18% when τ/C increases by 100% (from 2‰C to 4‰C).

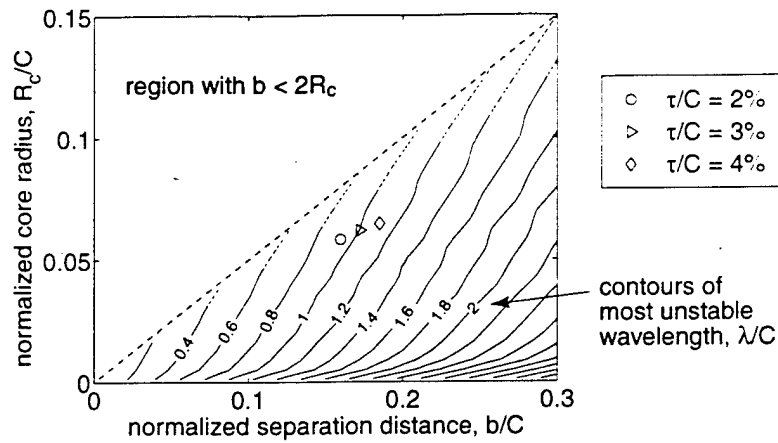


Figure 5.10 Contour plot of most rapidly growing wavelength λ/C as function of vortex core radius and separation distance. Symbols are estimations for three tip clearance sizes as labeled.

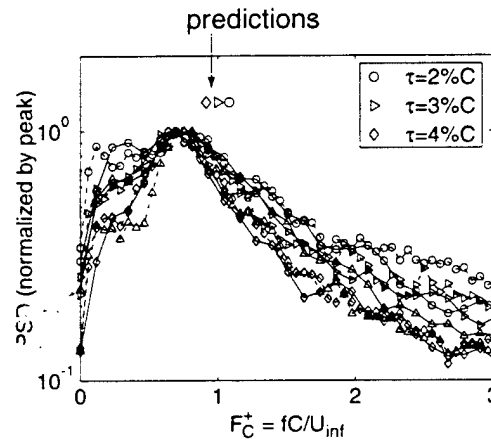


Figure 5.11 Comparison between measured frequency content and predicted frequency.

To examine the relevance of blade chord length as the length scale that sets the frequency of the vortex unsteadiness, a thought experiment is carried out as follows. Figure 5.12 shows the tip clearance vortex and its image vortex for two blade chord lengths: (a) geometry of the current cascade with $C = 0.190\text{m}$ and (b) exit plane of an imaginary compressor with $C = 0.380\text{m}$, *i.e.* with chord length twice that of the current cascade. Since the endwall structure scales with blade chord length for the same clearance to chord ratio as pointed out by Storer [5.5], the radius of the vortex core R_c and the separation distance b would scale with C as illustrated in the figure. Therefore, the wavelength λ as well as the frequency f should scale with C

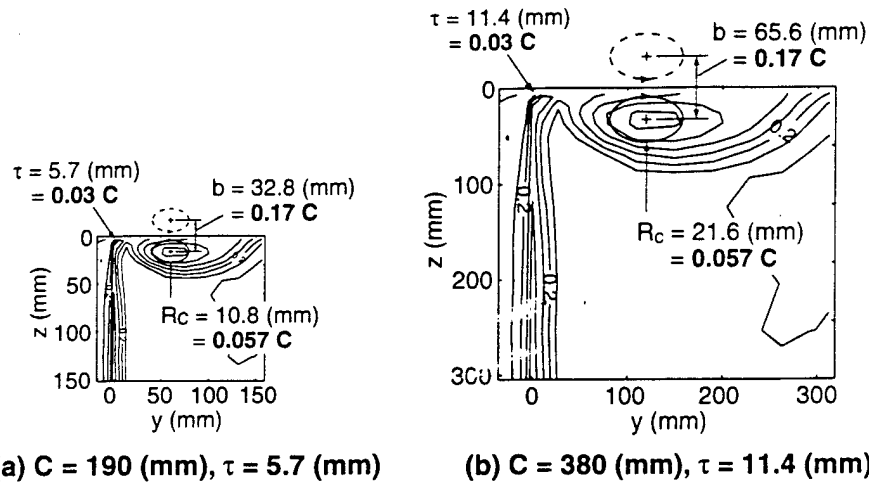


Figure 5.12 Vortex core radius R_c and separation distance b for two blade chord lengths. Both with 3% C clearance.

Figure 5.13 shows the result of the stability calculation carried out for the above two geometries. The far upstream velocity is the same for both cases and is 10m/sec. The dimensional frequency f is 50% smaller for 380mm-chord. However, the frequency collapses on to a single reduced frequency based on C illustrating the relevance of the chord length.

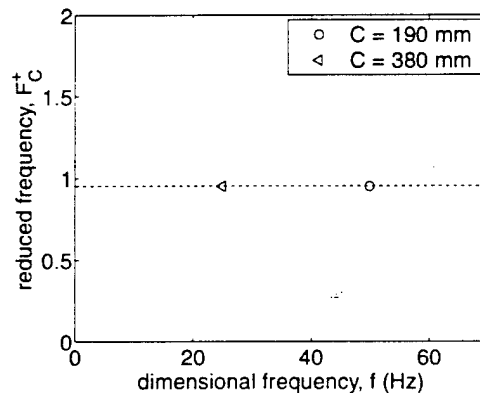


Figure 5.13 Dimensional frequency vs. reduced frequency using blade chord length.

In applying Crow's analysis in the axial plane near the trailing edge of the blades, we have made an approximation that the most unstable frequency is set by the local tip vortex core size and the local characteristics. Now it is to be noted that the tip vortex core radius and the separation distance increase as one proceeds downstream while Crow's theory applies to the situation where the vortex core radius and the separation distance are invariant with downstream distance. The degree of the variations in the local characteristics along the streamwise location is addressed in the following section.

5.5 Unsteadiness at Various Axial Locations

As mentioned above, R_c and b increase as one proceeds downstream. Effect of this variation on the characteristic frequency is discussed in the following. The radius of the vortex core, R_c/C (estimated using Rains' model) and the separation distance, b/C (estimated assuming linear increase from $2\pi C$ to b/C estimated in Figure 5.7(b)) are plotted against the distance along the chord, χ/C as shown in Figure 5.14(a). The rate of increase in R_c/C and b/C along χ/C is on the order of 10^{-1} . The most unstable wavelength and hence the frequency can be estimated at each location, χ/C on local basis as described in section 5.4. The result is shown in Figure 5.14(b). The characteristic frequency is predicted to decrease as one proceeds downstream, e.g. F_c^- drops by about 30% over $0.5C$.

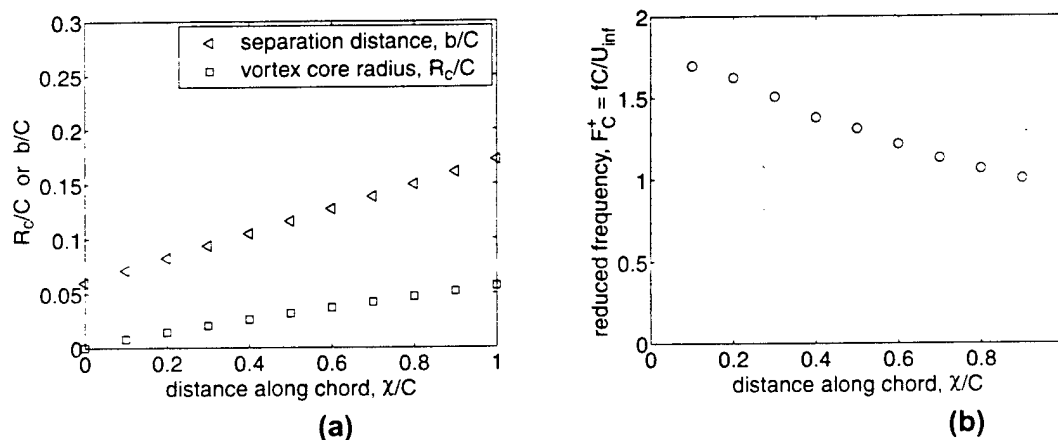


Figure 5.14 Variations along chord: (a) variations in R_c/C and b/C as function of χ/C ; (b) most unstable frequency F_c^+ predicted using local approximations.

Time-resolved measurements have been taken at various axial locations shown in Figure 5.15(a) using the hot-wire sensor, which is placed near the casing wall (approximately between the vortex core and the casing wall). The power spectral density at each location is shown in Figure 5.15(b). There is no dominant peak in the frequency content until about $\chi/C = 0.94$. The peak grows downstream, which is conjectured to be an evidence of the development of the instability. Figure 5.15(b) also shows that the reduced frequency drops by about 30% over $0.5C$ as predicted by the model. However, the radius of the vortex core and the separation distance are expected to asymptote further downstream of the blade exit plane as pointed out by Rains [5.4] and Chen *et al.* [5.6], and so is the reduced frequency.

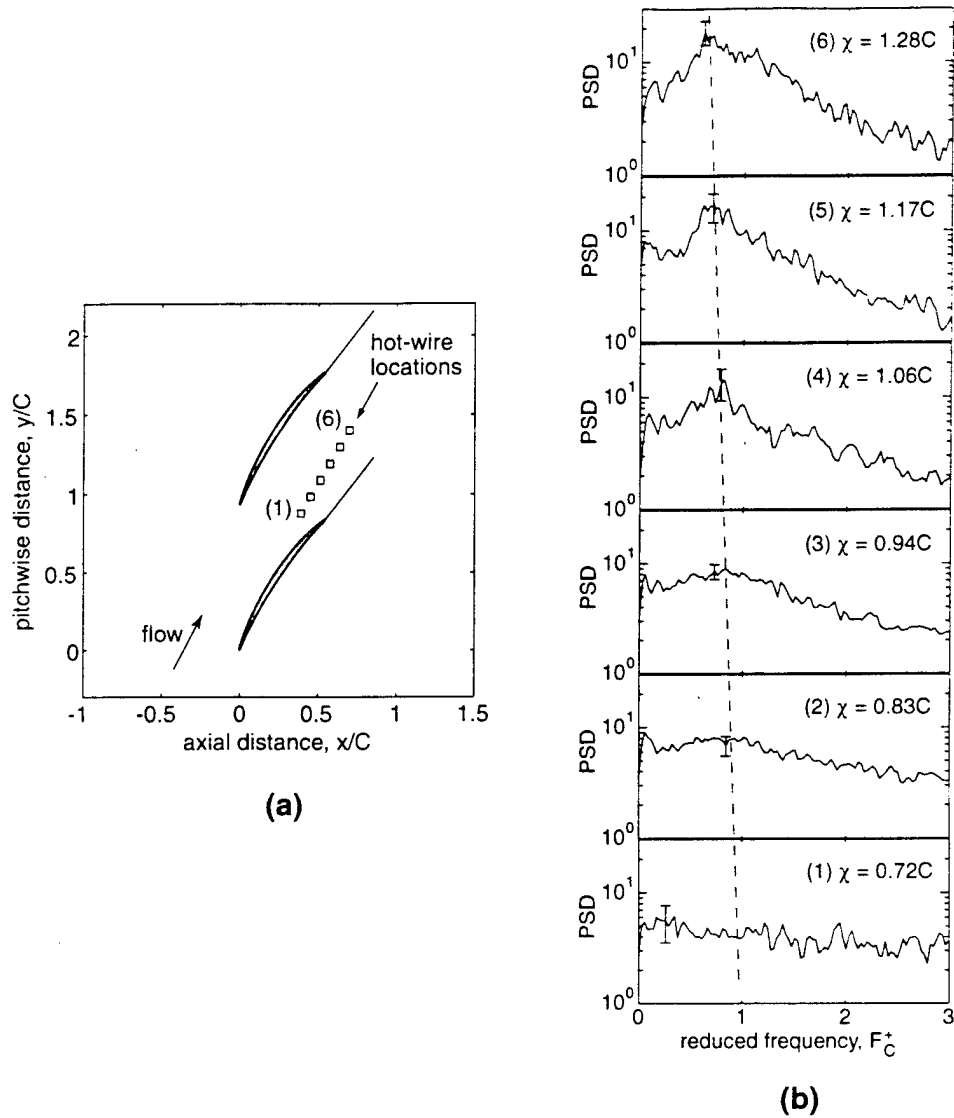


Figure 5.15 Time-resolved measurements at various axial locations: (a) locations of hot-wire sensor; (b) power spectral density at each location.

5.6 Summary

In this section, the results of the unsteady measurements in tip clearance vortex have been presented. The data showed that there exist a peak in the frequency content and it scales with upstream velocity but not with the tip clearance size. To explain the observations, the model-based approach has been taken. Two parallel counter-rotating line vortices are unstable because small displacements amplify due to the mutual induction [5.1] as is often seen as a wavy pattern of airplane's trailing vortices, whose wavelength corresponds to the most rapidly growing mode predicted by Crow's theory [5.1]. In the case of tip clearance vortex, the casing wall creates a mirror image of the vortex resulting in a similar configuration

as the trailing vortices. The most unstable wavelength can be predicted for the tip clearance vortex applying the same theory. Assuming that the vortex convects downstream at the far upstream velocity, one can predict the characteristic frequency of the unsteadiness. The predicted frequencies for three different tip clearance sizes are about the same as the observed frequency and show the unimportance of the tip clearance size in determining the characteristic frequency. Furthermore, the wavelength predicted by the model scales with the blade chord length warranting the use of the blade chord to non-dimensionalize the frequency. The frequency dependence of the blockage reduction with the use of NSJ actuation is because of the existence of natural mode of instability associated with tip clearance flow configuration. When forced by the NSJ actuator near the frequency at which the natural mode becomes unstable, the mixing between the tip clearance vortex and the main flow is promoted resulting in the observed endwall blockage reduction.

References

- [5.1] Crow, S. C., "Stability Theory for a Pair of Trailing Vortices", AIAA Paper No. 70-53, January 1970.
- [5.2] Chevalier, H., "Flight Test Studies of the Formation and Dissipation of Trailing Vortices", J. Aircraft, Vol. 10, No. 1, January 1973.
- [5.3] Crook, A. J., "Numerical Investigation of Endwall/Casing Treatment Flow Phenomena", GTL Report #200, MIT Gas Turbine Laboratory, December 1989.
- [5.4] Rains, D. A., "Tip Clearance Flows in Axial Flow Compressors and Pumps", California Institute of Technology, Hydrodynamics and Mechanical Engineering Laboratories, Report No. 5.
- [5.5] Storer, J. A., "Tip Clearance Flow in Axial Compressors", Ph.D. Dissertation, University of Cambridge, January 1991.
- [5.6] Chen, G. T., Greitzer, E. M., Tan, C. S., and Marble, F. E., "Similarity Analysis of Compressor Tip Clearance Flow Structure", ASME Paper No. 90-GT-153.

6 Overall Summary and Conclusions

Experiments have been conducted to demonstrate that the use of NSJ (Normal Synthetic Jet) at locations directly over the blade tip and tip vortex core is effective in reducing the flow blockage if actuation is at a reduced frequency of between 0.75 and 1 based on blade chord. The effect of NSJ on loss with the actuation directed above the blade tip region is minimal and in the situation where the actuation is directed at the tip vortex core the loss increases. We deduced that the reduction in blockage is associated with mixing enhancement and tip leakage flow reduction when the NSJ actuation is at the blade tip while it is associated with mixing enhancement only when NSJ actuation is directed at tip vortex core.

It was *hypothesized* that the reduced frequency at which NSJ actuation is the most effective could be related to an instability of a vortex pair consisting of tip leakage vortex and its image associated with tip casing. This is analogous to Crow instability associated with the pair of trailing vortices downstream of wing. Scaling arguments based on the use of Crow's analysis and Rains' model of tip leakage vortex core suggested that the most unstable frequency does correspond to the observed frequency.

However, the experiments that we have carried out only involve changes in tip clearance size but not the blade chord. So it is stretching to argue that the definition of reduced frequency based on blade chord is the one to be used. To mitigate this concern we use the Crow's analysis in conjunction with the Rains' model for tip leakage vortex core for the situations with different blade chords. When the computed unstable frequencies are made dimensionless based on the blade chord and the through flow velocity, they collapse onto a single curve. (Again it is to be noted that the tip vortex core increases in size as one proceeds downstream while Crow's theory applies to the situation where the vortex core size is invariant with downstream distance. Thus in using Crow's analysis here, we have made an approximation that the most unstable frequency is set by the local tip vortex core size and the local characteristics).

Likewise a similar set of experiments has been implemented to show that the use of DSJ (directed synthetic jet) is effective in reducing blockage as well as loss. The result is rather insensitive to the frequency of actuations. The use of DSJ actuation mainly involves momentum injection that is responsible for the observed blockage reduction and loss. To show that this is the case we have also carried out experiments with steady injection of directed jet (SDJ). The results are the same as the time-average results from the use of direct synthetic jets with the same time-average momentum coefficient.

Analysis and calculations have also been carried out to show that only about 15% (for DSJ) to 30% (for SDJ) of the flow power added by directed jet actuation is utilized in reducing the mass-average loss measured near the T.E. plane and the rest is lost mainly due to the mixing between the core flow and the high velocity jets – about six (for DSJ) to three (for SDJ) times the far upstream reference velocity. However the efficiency of the actuation can be increased while reducing the blockage by aligning the jet

in the streamwise direction and keeping the velocity ratio as low as possible but above one. Thus for a given time-average momentum coefficient, both the direction and the magnitude of the injected jet velocity are important and could potentially be tailored to achieve optimum results. The DSJ and SDJ used in the current study may not have been the optimal actuators that one can design; thus this aspect will need to be re-examined.

In conclusion we offer the following remarks:

- The use of NSJ (Normal Synthetic Jet) is not cost effective and it is not worthy of any further pursuit.
- Directed jets are effective and should be further explored for potential in not only mitigating the effect of tip leakage flow on performance at design but also on compressor stability.
- The suggestion that tip leakage flow system in turbo machinery has an instability behavior analogous to Crow instability is new and it may explain some of the observed measured and computed unsteady results associated with tip leakage flow in the multi-blade row environment.

PART II

MEASUREMENT OF SHEAR STRESS AND TEMPERATURE USING MEMS FABRICATED SENSORS

K. Breuer

Brown University

INTRODUCTION

The research program originally intended to integrate MEMS sensors and actuators into the active control program. This was not ultimately achieved for the primary reason that the original budget was cut in the third year. However, MEMS sensors were successfully fabricated and tested. The following section describes that part of the effort. Much of this section is derived from a paper presented at the ASME Winter Annual Meeting in Anaheim, November 1999.

BACKGROUND

Measurement of shear stress and temperature in complex flows is of great importance and interest. The desire for high-performance, low cost sensors with high bandwidth has motivated the use of MEMS processes for fabricating small, low-cost shear sensors. Two approaches in MEMS Shear sensors have been pursued. The first uses a floating element sensor (Schmidt *et al.* 1988, Padmanabhan *et al.* 1995, Pan *et al.* 1995). This has many benefits, including the fact that the measurement is a direct one and not reliant on indirect correlations between shear and some other phenomena – usually heat transfer coefficients. However, these techniques are also typically complex and require fabrication of somewhat complex mechanical devices and accurate transductions of small motions. The second, more common approach is to use the familiar techniques of thermal anemometry, in which the shear is related to the convective cooling of a heated element. This technique, while reliant on the convective properties of the flow, benefits from its simplicity, its lack of moving parts and relatively good sensitivity. Examples of MEMS devices fabricated along these lines have typically used polysilicon as the sensing element (Lui *et al.* 1994; Kälvesten *et al.* 1996). This

choice of materials stems from polysilicon's ease of processing, but has some difficulties, namely a relatively low temperature coefficient of resistivity and a high resistance of the sensing element, which leads to high noise and difficulties with stability when driving in constant temperature mode. Motivated by these issues, we report on the design of a thermal shear sensor using Platinum as the sensing element.

SENSOR DESIGN

Hot film sensors are particularly sensitive to parasitic losses to the underlying substrate, which severely limit their frequency cutoff and can induce non-uniform phase response. Reducing the communication of the hot film sensor element to the supporting substrate minimizes these problems.

With this as a guide, the design of the sensor is illustrated in Figure 16, and is based on a number of design goals:

- Minimize the thermal mass of the sensor to maintain a high frequency response. This requires that the sensor element be small and (more importantly) that the sensor be thermally isolated from the substrate.
- Keep sensor resistance relatively low (to keep noise down and to allow for standard circuitry)

These goals are accomplished by depositing the Platinum sensor film on a thin Silicon nitride membrane (1500-Å) suspended over a "deep" (20 micron) evacuated cavity as shown in Figure 16. The vacuum cavity eliminates direct conduction to the substrate while the thin membrane limits the thermal conduction path through the membrane. The electrical connections are achieved using the sensor metal and a second layer of gold, which serves to minimize the lead resistance.

Our control strategy was designed to exploit the special condition when the initial shear layer frequency is related to the column mode frequency. This makes use of the natural shear layer amplification mechanism to carry the energy in a narrow band through a succession of pairings, to the final column mode frequency. Thus the most amplified region for the column mode, 4-5 diameters downstream, can be efficiently excited by actuators located at the jet exit.

The excitation also has as an extra parameter which is the azimuthal mode number. As illustrated in Eq[4], this offers another degree of freedom to select a broader band of frequencies and remain within the range of the most amplified Strouhal number.

2 Experimental Approach

The experiments were broken into two parts:

1. A study of the concept of open-loop and closed-loop excitation of the jet which couples the shear layer and column modes. This was done with an azimuthal array of miniature speakers, following the setup used by Corke and Kusek (1993).
2. A study of the ability to excite helical modes in a jet using phased plasma actuators. This is seen as the ultimate extension of the laboratory setup to full scale applications. The advantages of these actuators are that they can be easily scaled up in size, and that they have no moving parts.

Figure 1. shows the basic concept for the approach and signal processing concept for actuation which couples the shear layer and column modes. In the top schematic in the figure, sensors are located near the end of the potential core, where they would be most sensitive to velocity fluctuations associated with the jet column instability mode. The sensors are spaced apart in flow direction by an amount corresponding to one-half the wavelength of the column mode. The time series from these two sensors are combined (subtracted) in order to remove incoherent fluctuations not associated with the column mode. Other sensors placed near the exit of the jet, are used to monitor the initial shear layer instability. These sensors are spaced in the azimuthal direction so that phase measurements can determine the azimuthal mode number. The azimuthal angle of 30° shown in the schematic would resolve azimuthal mode numbers of up to 6.

The lower part of Figure 1 shows a block schematic of the processing steps that are used to take the sensor outputs and construct the actuator inputs. These start with the pair of sensors near the end of the potential core. The output from these are differenced to produce a time series which is representative of the column mode. This principle frequency is then f_c , which we presume to be related to the shear layer frequency, f_s , as $f_c \simeq f_s/2^n$, where n is an integer between 1 and 3. The closest value of n is determined by comparing $f_s = 2^n f_c$ with the shear layer frequency measured with the sensors placed near the jet exit. The actuator input signal is then constructed from the column mode time series whose frequency, when multiplied by 2^n , most closely corresponds to the shear layer frequency. That signal goes through a parallel network of variable gain amplifiers corresponding to each speaker around the jet exit perimeter. The gain settings control the azimuthal mode number that are excited.

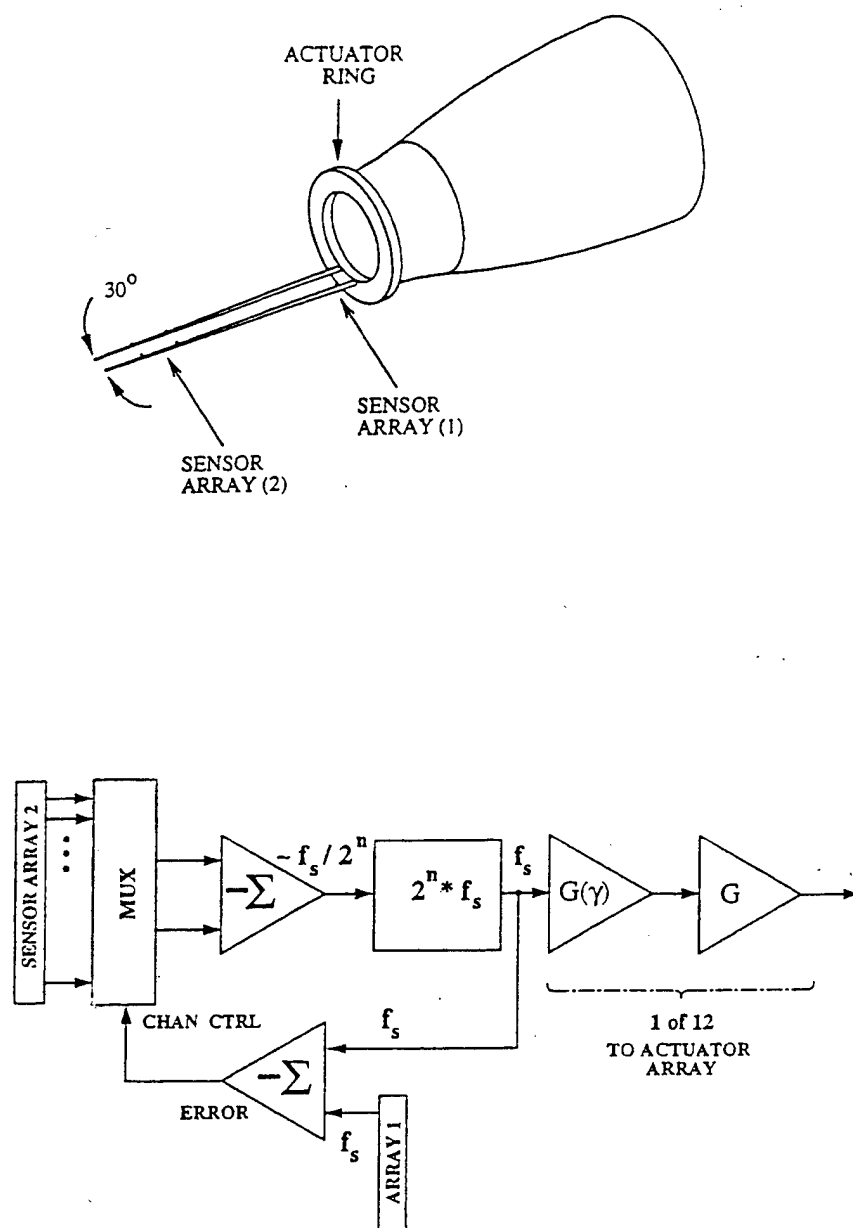


Figure 1: Concept overview of arrangement to produce disturbances which couple shear layer and column modes.

The approach is designed to produce pairs of helical modes with equal/opposite wave angles (or equal plus/minus mode numbers, m). The sum of two helical waves of opposite sense around the jet results in a standing wave pattern corresponding to

$$\underbrace{A \cos(m\gamma)}_{G\gamma} \sin(\omega_s t) \quad (5)$$

where $\omega_s = 2\pi f_s$ is the shear layer frequency, and $\cos(m\gamma)$ is the azimuthal amplifier gain, $G\gamma$ needed to excite mode numbers $\pm m$.

An example of the ideal and measured amplitude in the shear layer corresponding to azimuthal amplifier gain settings designed to excite $m = 0$ and $m = \pm 1$ is shown in Figure 2. This approach applies to any type of azimuthal actuator (speakers or plasma). $G\gamma$ can be set manually, or be part of the feedback control similar to what was done by Ahn (1994).

One of the issues in the approach shown in Figure 1 is the optimum placement and spacing of the pair of sensors located near the end of the potential core. This is addressed in the results in Figure 3. This corresponds to measurements on the axial centerline of jet at $Re_D = 70,000$. The nozzle is the same as that used in the previous work of Corke & Kusek (1993). The exit diameter is 2 inches (5.08 cm) so that the centerline exit velocity is approximately $Re_D/1000$ feet per second. Based on $S_t = fD/U_j = 0.44$, the column mode frequency is approximately 180Hz.

The top plot corresponds to the streamwise development of the amplitude of streamwise fluctuations at the column mode frequency. This shows a peak at $x/D \simeq 4$. This is consistent with past measurements and indicates the optimum streamwise location to monitor the velocity fluctuations associated with the column mode.

The lower plot shows the effect of different spacings between two sensors on the amplitude of the difference signal at the column mode frequency. The streamwise location of the sensors is at $x/D \simeq 4$. This indicates that the optimum spacing is between 4 to 5cm. This spacing corresponds to a phase speed of approximately $0.8U_j$, which is consistent with past experiments. Based on this phase speed, the optimum spacing between the sensors can be adjusted for different jet velocities.

A more developed instrumentation schematic which was used to test the concept in Figure 1, is shown in Figure 4. This shows two optimally placed hot-wire sensors near the end of the potential core. The output of the sensors was proportional to the streamwise velocity fluctuations. These were band-pass filtered about the column mode frequency and differenced to produce a time series which was predominantly representative of the velocity fluctuations associated with the jet column mode.

Our objective was to produce a time series to the actuator which was a combination of the column mode and shear layer frequencies, but which was centered near the most amplified frequency of the shear layer. To accomplish this, an amplitude modulation circuit was used whereby the modulation input corresponded to the column mode time series, and the higher frequency carrier signal was near the shear layer frequency, and satisfied the constraint that $f_s = 2^n f_c$. The effect of the selection of n will be presented in forthcoming figures.

The effect of the amplitude modulation is to produce a time series with a center frequency at the carrier frequency, f_s in our case, and with side-band frequencies corresponding to the sum and difference of the modulation frequency, f_c in our case. Therefore this accomplishes our objective.

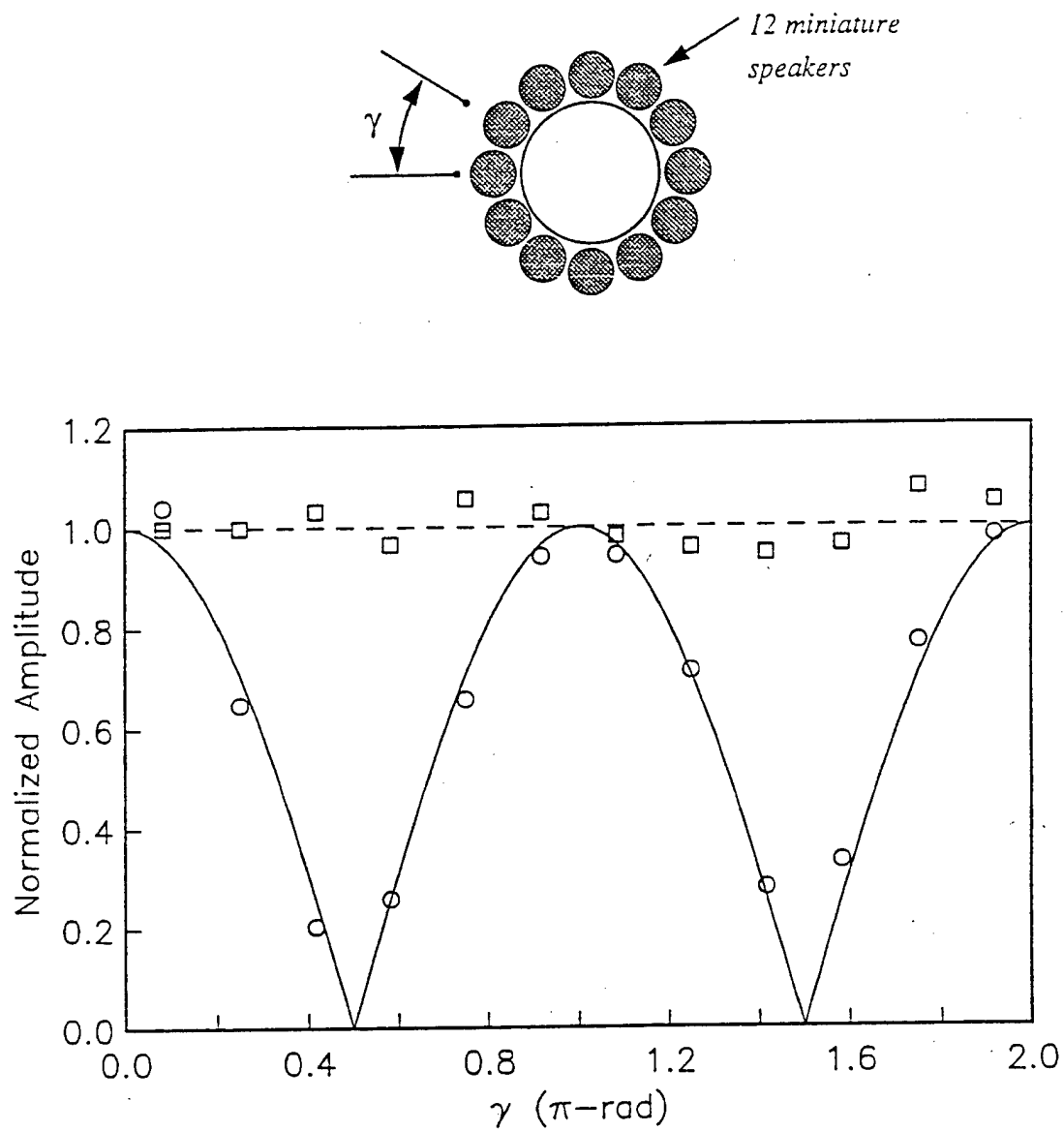


Figure 2: Ideal (curves) and measured (symbols) amplitude of streamwise velocity fluctuations corresponding to $m = 0$ and $m = \pm 1$ excited modes.

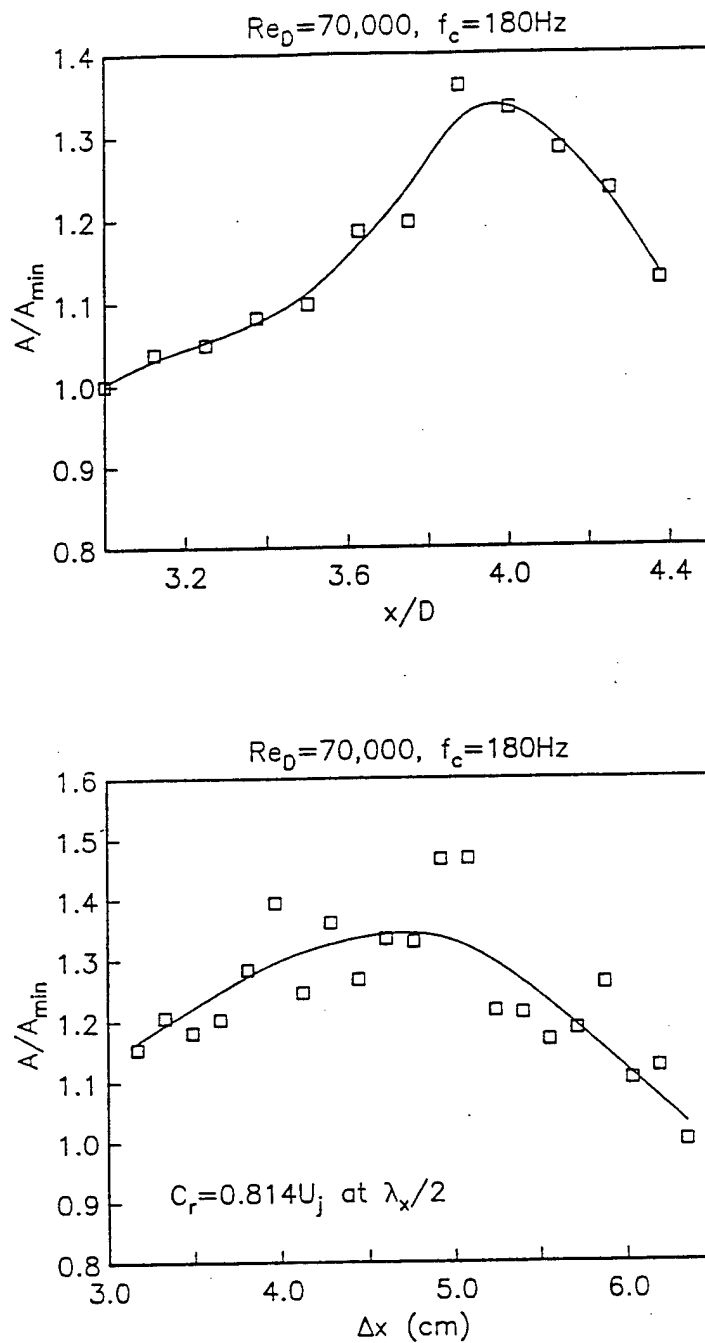


Figure 3: Effect of streamwise location and spacing of sensors on the measured amplitude of streamwise velocity fluctuations associated with the column mode.

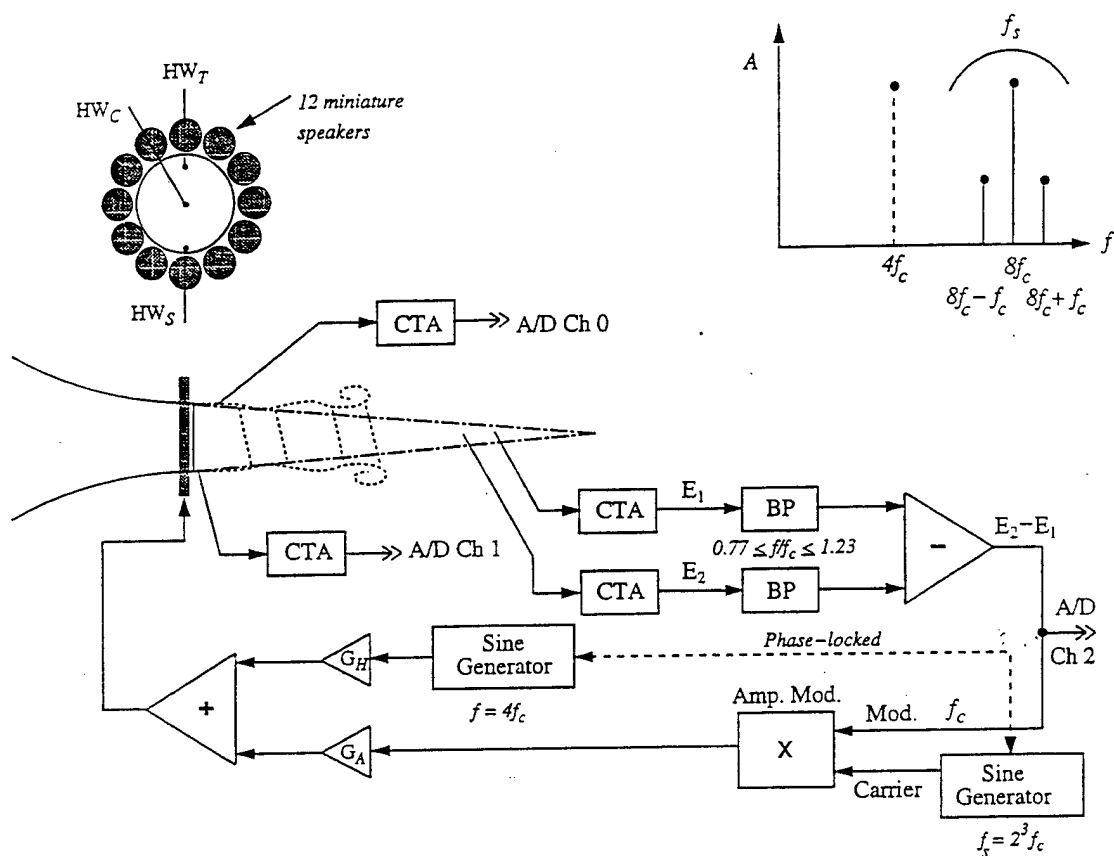


Figure 4: Instrumentation schematic used in feedback arrangement to couple shear layer and column modes in the jet.

In this schematic, the carrier time series was supplied by a sine wave generator. This was necessary to investigate different values of n . The amplitude modulated time series was gained and sent to each of the speakers. In this case the azimuthal amplitude was constant so that the excited mode was axisymmetric, and the gain was indicated as G_A . In some instances, a second sine wave was used to excite helical modes. This was generated by a second sine generator which was phase locked with the other generator. In these cases the frequency used was the subharmonic of the shear layer frequency in order to produce a helical mode subharmonic resonance.

The response of the shear layer was monitored by two hot-wire sensors which were placed in the linear growth region of the shear layer and 180° degrees apart in the azimuthal direction. The time series from these two hot-wires as well as the difference time series from the column mode sensors were digitally sampled and recorded for later processing.

The effect of different values of the exponent n is embodied in the results plotted in Figure 5. In this experiment, the maximum amplitude in a narrow band near $S_t = 0.44$, the frequency with the maximum amplitude, and the coherence between velocity fluctuations measured in the shear layer at the exit of the jet and on the centerline at $x/D = 4$, are recorded as the carrier frequency in the schematic in Figure 4 was varied.

For $Re_D = 70,000$ in this case, the column frequency at $S_t = 0.44$ is $f_c = 172\text{Hz}$. The bottom plot in Figure 5 shows that the frequency of the maximum amplitude fluctuations measured by the downstream sensors is close to the expected value, and does not vary significantly with the carrier frequency. However, the middle plot shows that the amplitude of the fluctuations associated with the column mode is sensitive to the frequency. In this case we observe local maxima, with magnitudes which increase with increasing carrier frequency. For reference, dashed lines are drawn at frequencies which correspond to $2^n f_c$ for $n = 1, 2$ and 3 . We observe that the local amplitude maxima roughly correspond to the locations of the dashed lines, indicating a coupling between the carrier (shear layer) modes and the column mode. This is further demonstrated by the coherence, which is an indication of the phase locking. This shows the highest phase locking occurs at the intervals in the frequencies where the carrier frequency is $2, 4$ and 8 times f_c . These results are representative of the full range of tested Reynolds numbers, from $30,000$ to $70,000$, although the preference to the 2^n frequency coupling between the shear layer and column modes was more acute as the Reynolds number increased. In all the cases, the highest column mode amplitudes occurred with $n = 3$, or the shear layer frequency being 8 times the column mode frequency.

3 Results with Feedback Control

The majority of the results focussed on $Re_D = 55,000$. Figure 6 documents the effect of the carrier frequency on the coupling between the shear layer and column modes in the manner of Figure 5. This again shows preferred frequencies which correspond to $f_s = 2^n f_c$ with $n = 1, 2$ and 3 . In this case, $f_c = 130\text{Hz}$ for $S_t = 0.44$.

The results in Figure 6 correspond to an axisymmetric shear layer mode at a single frequency. As the schematic in Figure 4 indicates, the shear layer mode can be a combination of axisymmetric and helical modes at different frequencies. These combinations were investigated in terms of the effect it would have on the coupling between the shear layer and column modes. The results are shown in Figure 7.

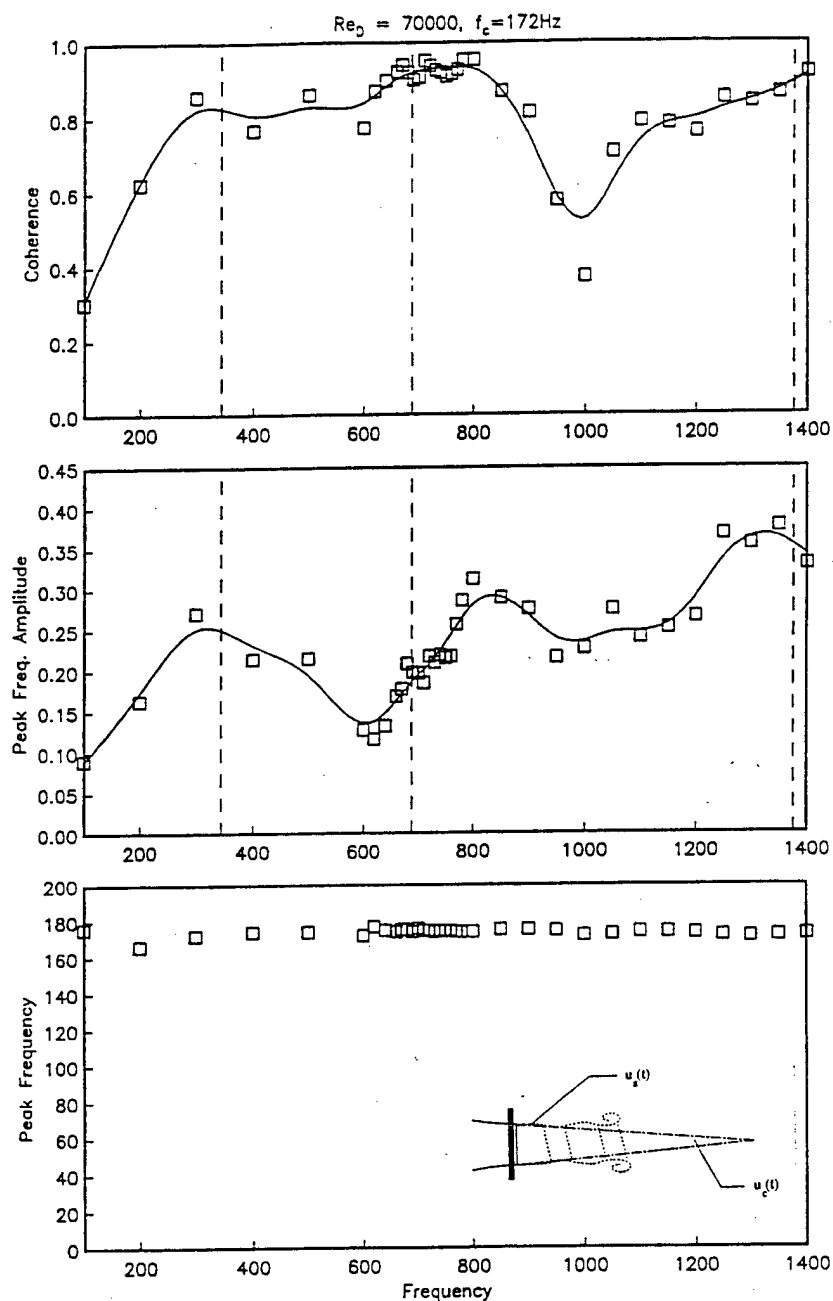


Figure 5: Response of column mode frequency, amplitude, and coherence with different input shear layer (carrier) frequencies in the arrangement shown in Figure 4. The vertical dashed lines correspond to $2f_c$, $4f_c$ and $8f_c$. $Re_D = 70,000$

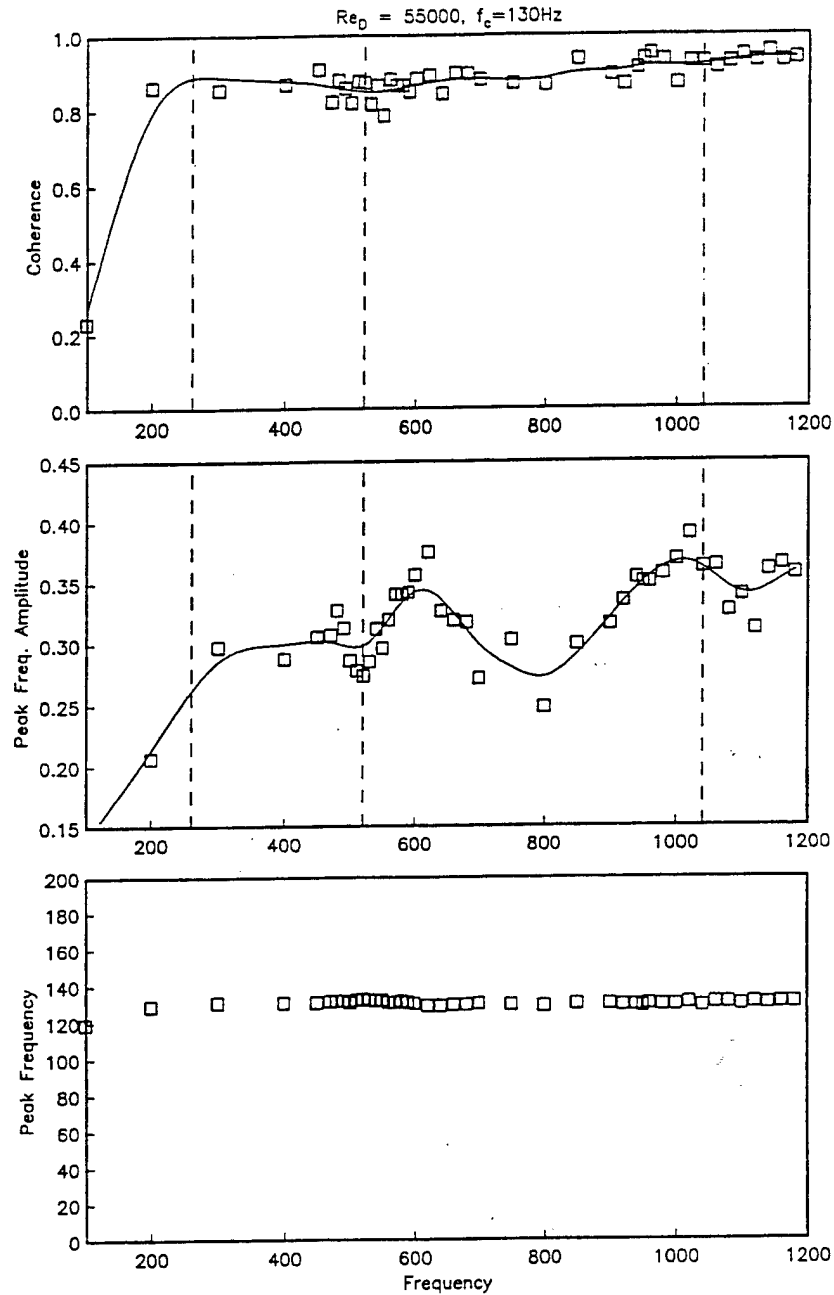


Figure 6: Response of column mode frequency, amplitude, and coherence with different input shear layer (carrier) frequencies in the arrangement shown in Figure 4. The vertical dashed lines correspond to $2f_c$, $4f_c$ and $8f_c$. $Re_D = 55,000$

Figure 7 shows the coherence between the streamwise velocity fluctuations measured on the centerline at $x/D = 4$, and in the shear layer just downstream of the jet exit. The column mode frequency in this case is 130 Hz. Based on the results in Figures 5 and 6, the shear layer frequency was set to be 8 (2^3) times f_c . The results are divided into two sets. In the top set, a single shear layer frequency is used. The different curves then correspond to different azimuthal mode numbers ($0 \leq m \leq \pm 6$). The bottom set uses two frequencies. For these, $m = 0$ has a frequency set at 8 times f_c . The different curves then correspond to helical modes with different azimuthal mode numbers, at the shear layer subharmonic frequency. This was intended to produce a helical mode, subharmonic resonance of the type studied by Corke and Kusek (1993).

In either case, we are seeking a high coherence between at the shear layer and column mode frequencies. In almost all the cases for a single frequency shear layer mode, in the top part of Figure 7, the coherence for the column mode is high, regardless of the shear layer azimuthal mode number. The coherence at the shear layer frequency varies, but the best for these cases occurs for $m = \pm 4$.

Adding a subharmonic helical mode to the shear layer excitation results in near perfect coherence at the shear layer frequency. This however lowers the coherence at the column mode frequency. However, the coherence nearly matches that of the case with $m = 0$ alone, as m of the subharmonic mode increases. In particular, subharmonic modes with $m = \pm 4$ and ± 3 result in a coherence at the column mode frequency which is just slightly lower than those without the subharmonic mode added. This combination of modes does the best to phase locking all of the principle frequencies in the shear layer, and at the end of the potential core. It therefore has the best possibility to have an impact on the global properties of the jet flow many diameters downstream.

The previous results correspond to measurements taken at one location in the shear layer. Depending on the frequency, this may not be at the location of the highest amplitude or coherence. Therefore a detailed study was done using an additional hot-wire sensor which was traversed throughout the jet flow. For these, we chose to concentrate on one case corresponding to closed-loop feedback with a combination of shear layer modes with $m = 0$ at $8f_c$ and $m = \pm 2$ at $4f_c$.

The results for this investigation started with cross-spectra of time series sampled throughout the jet. An example of this is shown in Figure 8. These correspond to measurements at $x/D = 0.375$. The left column corresponds to the jet without forcing. The right column corresponds to the jet with closed-loop forcing described in the previous paragraph. The top row shows contours of constant spectral amplitude with normalized levels in percent u'/U_j . The bottom row shows coherence levels in the standard range, although only values above 0.5 are plotted. The measurements were taken within the shear layer. The radial position is normalized by the local momentum thickness θ .

In the unforced jet, the principle frequencies, f_c and f_s are indicated. It is interesting to note that fluctuations at the column mode frequency are very evident in the shear layer near the exit of the jet. This is seen as both a local peak in the spectrum, and in the coherence at the location just inside of the shear layer centerline. This is undoubtedly due to pressure feedback from the end of the potential core. This suggests that sensors that monitor the amplitude of the column mode could be located at the exit of the jet, rather than on a sting which reaches to $x/D \simeq 4$, as was proposed in Figure 1.

In the jet with closed-loop forcing, the largest spectral peak corresponds to the subhar-

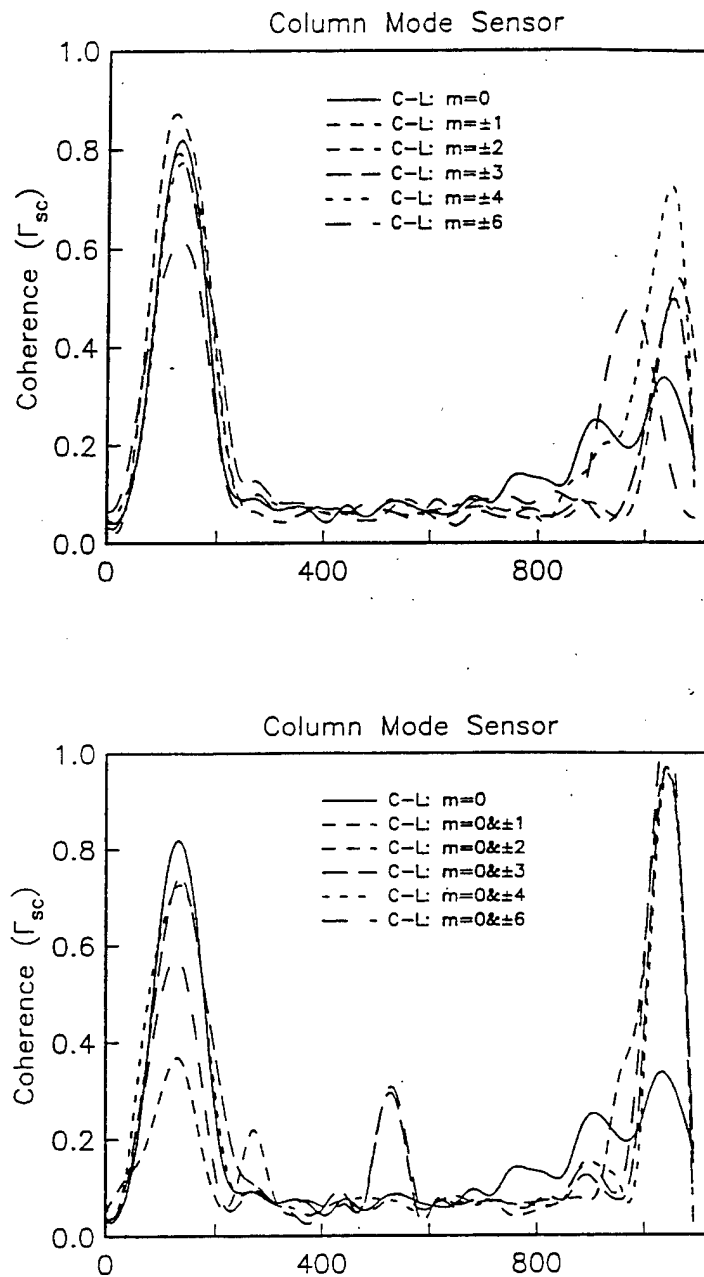


Figure 7: Coherence measurements between shear layer and column mode sensors . $Re_D = 55,000$

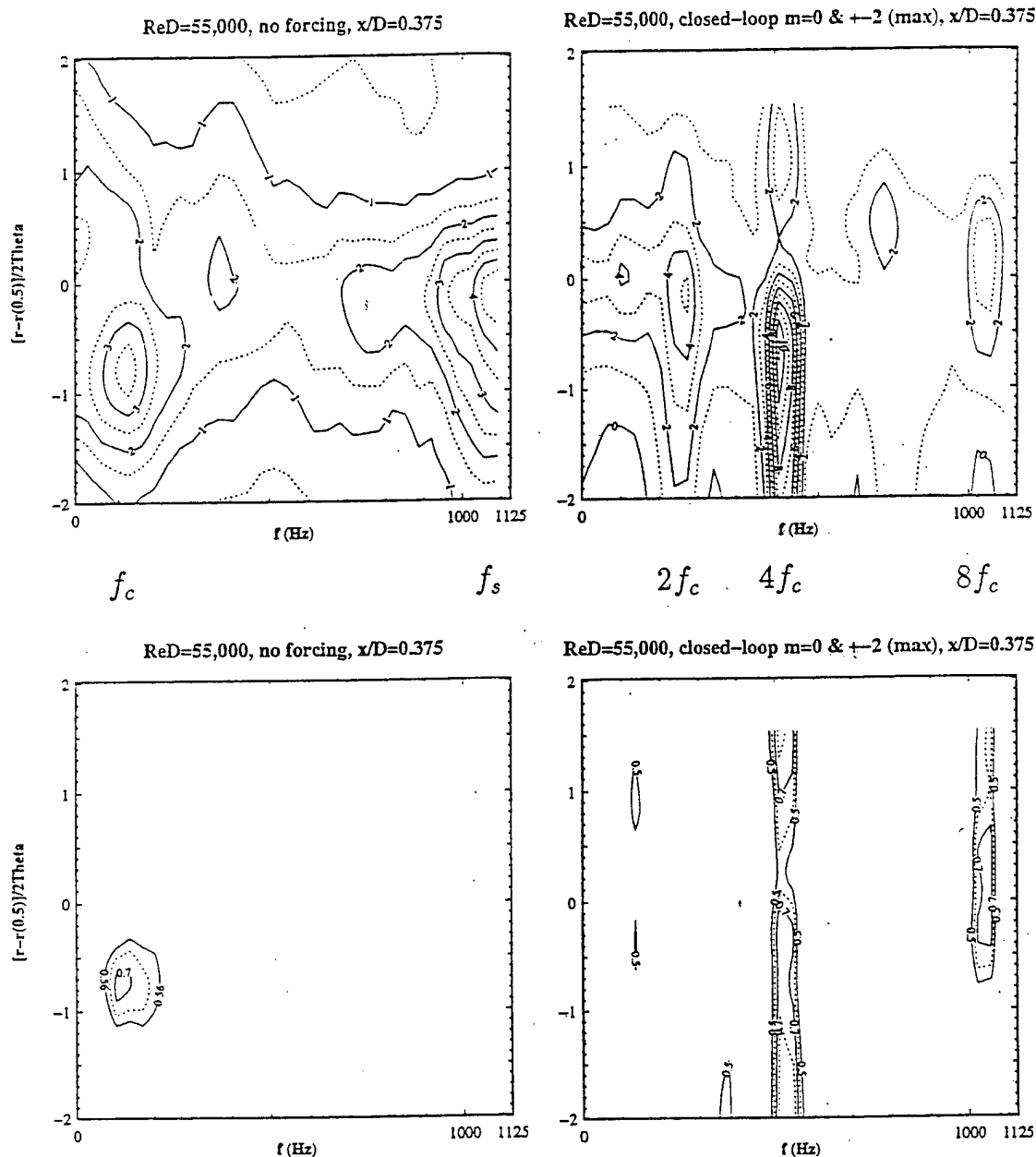


Figure 8: Contours of the spectral amplitude and coherence across the shear layer at $x/D = 0.375$ for unforced (left) and close-loop forced (right) conditions. $Re_D = 55,000$

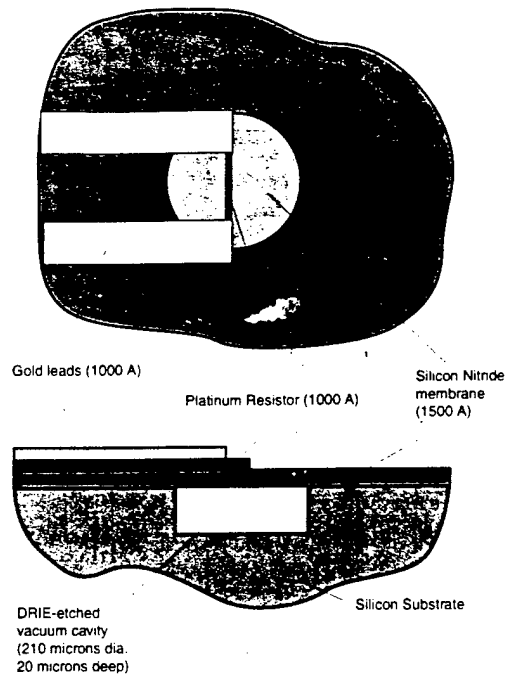


Figure 16 Schematic of Thermal Shear sensor/temperature sensor design. The sensor element is mounted on a thin membrane, which covers a vacuum cavity.

The cavity thickness and diameter were sized to optimize the trade-off between conduction losses and membrane deflection and fracture strength. Thermal isolation dictates that the membrane be as large and as thin as possible so that heat generated at the sensing element experiences a high thermal barrier in leaking to the substrate. Placing the membrane over a vacuum cavity ensures that no energy is lost directly. However, the pressure difference across the membrane between the vacuum and the ambient pressure above results in a severe bending stress which can lead to fracture. In particular, Silicon Nitride, while strong, is also brittle and deposits under considerable tensile strength. Thus, membrane fracture strengths limit the membrane diameter and thickness. These considerations lead to a membrane diameter of 210 microns and 1500-Å thick.

To minimize the direct thermal mass of the Platinum, the resistors are fabricated as small as possible, limited by lithography. Line widths of 3, 5 and 10 microns were attempted although it was found that 3 microns was not reliable. Since the leads to the resistor serve as a parasitic loss, their resistance was minimized by increasing their cross-sectional area and by depositing 5000-Å of gold on top of the platinum used as the resistor. In the end, the resistance of each lead was 2% of the sensing resistor.

The temperature sensors are effectively the same sensors. However, they are operated in a four-point manner in which a small current (not large enough to create Ohmic heating) is passed through the sensor through a first set of leads. The voltage drop across the sensor is read off via a second pair of leads. This method eliminates lead resistance effects. However, but when large arrays of temperature sensors are fabricated, the number of leads becomes a significant issue, particularly for packaging.

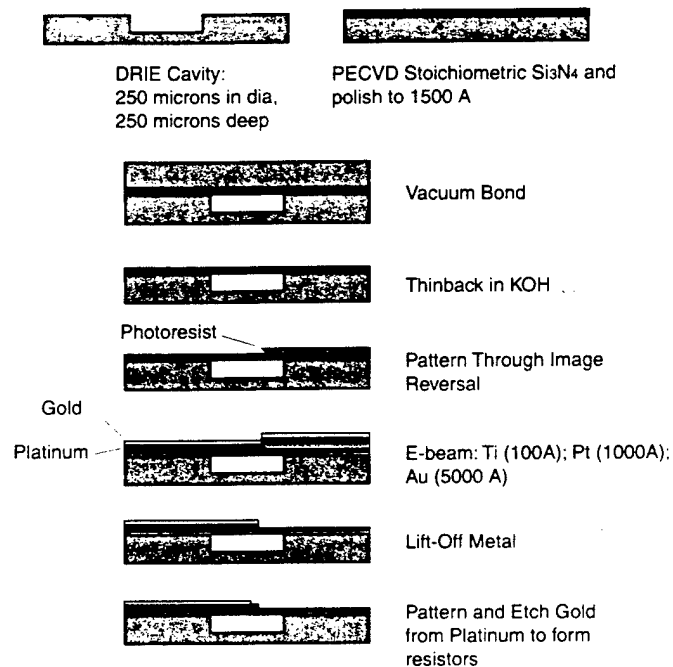


Figure 17: Shear Stress and Temperature Sensor Process Flow.

SENSOR FABRICATION PROCESS

The shear stress sensor and the temperature sensor are identical in all but the geometry and are thus fabricated in parallel. Figure 17 details the process flow in cross-sections. The following steps characterize the process:

- The “device” wafer is patterned with the cavity holes, and etched by DRIE to a depth of 20 microns. This wafer is then coated with 7000-Å of thermal oxide which serves as a stress relief between the silicon wafer and the nitride membrane.

- A second "capping" wafer is coated with 1900-Å of stoichiometric silicon nitride. In order to assure uniformity across the wafer, this layer is chemically-mechanically polished back to 1500-Å. This results in less than 50-Å deviation in the nitride thickness across the wafer.
- The device and capping wafers are fusion bonded at 1100°C for 3 hours. This can be achieved at an arbitrary pressure, thus controlling the cavity pressure. In the current process Nitrogen at 1atm and vacuum (10^{-3} Torr) were used.
- After removing the nitride from the back of the capping wafer, the bonded pair is mounted with the device wafer face down on a glass plate coated with canuba wax. The mounted pair (capping wafer facing up) is placed in a 20% KOH solution at 64 C for 20 hours which etches away the capping wafer leaving only the device wafer, now covered by the nitride film. There is no detectable etch rate of KOH on nitride, thus over-etching is not of concern.
- After an RCA clean, the device wafer is patterned for the metal layer using image reversal photolithography. This was chosen because the developed features in the photoresist have negative sloping sidewalls. That is, a slight overhang is created.
- The metal layers are deposited using e-beam deposition. A 100-Å layer of Titanium is used as an adhesion layer for 1000-Å of Platinum. Finally, 5000-Å of gold is deposited on top of the Pt/Ti. All three metals are deposited sequentially without breaking the vacuum on the e-beam chamber. This greatly improves device yield and layer adhesion.
- The sensors and electrical leads are defined by dissolving the photoresist under the metal layer (lift-off). The negative sidewalls in the photoresist are used to our advantage because they create a stress concentration in the metal and form a clean break with the metal on the resist.
- The sensors are defined by patterning and etching (in Potassium Iodide) the top layer of Gold in selected areas to reveal the Pt/Ti layer below.
- The final step is to sinter the wafer at 450 C for 1 hour. This reduces the contact resistance between the Gold-Platinum interface and stabilizes the sensor during operation.

COMPLETED DEVICES

Completed devices are shown in Figure 18 and Figure 19, which show optical micrographs of shear and temperature sensors respectively. The sensing element is the thin line crossing horizontally across the vacuum-backed membrane, which is visible as the light-colored circle.

The deflection of the cavity under the atmospheric pressure loading is clearly visible. The lower frame of Figure 18 shows an array of sensors, each comprised of a pair of hot wires oriented at ± 30 degrees to the oncoming flow. In this manner, the sensors can detect the direction of the shear in the horizontal plane. Figure 19 shows the four-wire temperature sensor. In this case, the sensing element is very small since there is no directional nature to the sensing element and it is desirable to keep the sensing element as small as possible so as to minimize its thermal mass.



Figure 18. Optical Microscope photo of shear stress sensors. The white line is the exposed platinum of the sensing resistor due to the gold being etched away. The light colored circle is the 1500-Å nitride membrane over the vacuum cavity. The left frame shows a single sensor while the right frame shows an array of three two-dimensional sensors, each of which enable a directional measurement of shear.

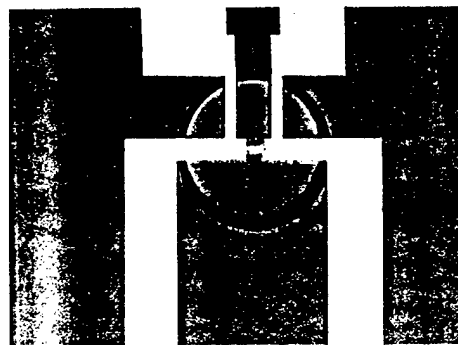


Figure 19. Optical micrograph of a fabricated temperature sensor. The sensing resistor (10 microns wide) is oriented horizontally. The two leads from the bottom supply a small (fixed) current. The leads above are at a floating potential and used to measure voltage drop across the sensor resistor which changes as the sensor resistance changes with temperature.

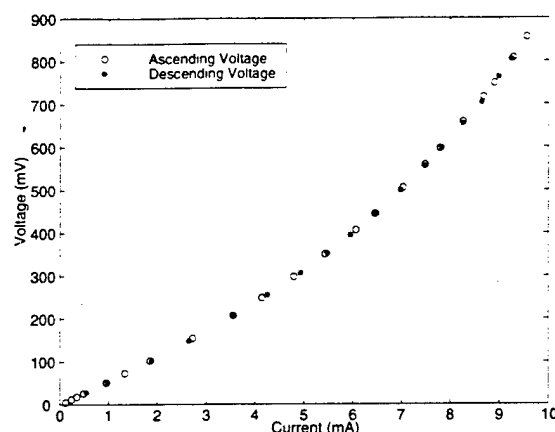


Figure 20: Voltage-Current behavior of hotwire sensors (5 μm x 100 μm long) sensor on a vacuum cavity. The positive curvature indicates self-heating due to Ohmic losses.

Figure 20 illustrates the response of the current-voltage characteristics for a 100-micron resistor long 5-micron wide shear sensor. Both ascending and descending applied voltages are plotted demonstrating the lack of hysteresis. The positive curvature illustrates the Ohmic heating at high current which results in an increase in the sensor temperature (the effect that is used to operate the wire as a fluid sensor). In this case, the (DC) resistance changes by a factor of two, rising from approximately 50 Ohms to about 90 Ohms at 10 mA (approximately 9mW power dissipation). This range of resistances is very comfortable for most commercial anemometer systems, making operation quite convenient.

As discussed earlier on, a desirable goal in the design of any shear sensor is the minimization of thermal losses to the substrate. This has two deleterious effects on the sensor performance. The first is a loss of sensitivity which is enhanced by ensuring that as much thermal energy as possible is lost through the convective cooling to the test fluid and as little thermal energy is lost via the parasitic losses to the substrate. A second undesirable effect of parasitic heat losses is an increased effective thermal mass of the sensor. This is due to the fact that the heated substrate has a temperature above that of the ambient test fluid and thus acts as a sensor itself. Thus the

effective thermal mass of the sensor includes not only the actual sensor element, but also the surrounding heated substrate.

The effectiveness of the vacuum cavity and the thin membrane were assessed by imaging the operating sensor with an InfraRed camera. A typical image, with no ambient flow, is shown in Figure 21. The resolution of the image is not ideal and is approximately 20 microns/pixel. At this resolution, the sensor element (which is only five microns wide) is below the resolution of the camera and we only see the temperature of the silicon nitride that forms the membrane and covers the surrounding silicon substrate.

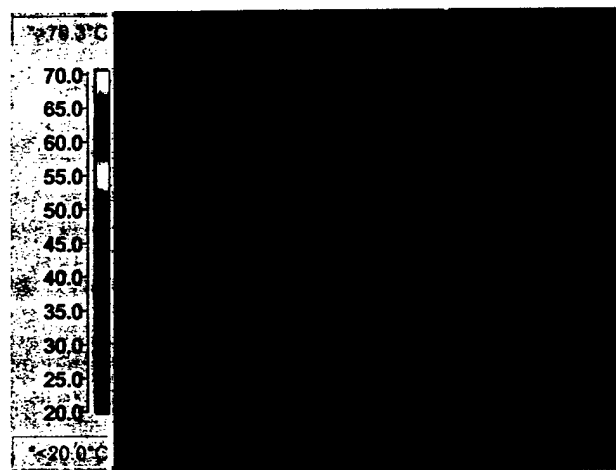


Figure 21: Infrared image of sensor operating at 336 milliVolts and 7 milliamps in still air, which represents a resistive overheat of 1.4. The image indicates that the sensor becomes much hotter than the surrounding substrate, and there is no perceptible temperature rise in the leads.

The gold leads, which are clearly visible in black, appear to be five degrees cooler than the surrounding substrate. This, however, is misleading since the calibration of the IR image is for the emissivity of the silicon nitride surface, not the gold leads. In fact the nitride surface and the gold leads are at the same temperature of approximately 24 degrees Celsius (room temperature). In contrast to this, the membrane and sensor element rise to approximately 70 degrees and confirm that excellent thermal isolation has been achieved, as evidenced by the fact that the temperature at the edge of the membrane has fallen to within a few degrees of the ambient and that the small effective thermal mass is preserved. The images with an ambient flow confirm this point even more pointedly.

Having illustrated the device's basic functionality, the sensor was operated as a shear sensor in a fully turbulent boundary layer. This test provided valuable information on the sensor's mechanical and electrical stability and robustness as well as its performance as a thermal fluid sensor.

The sensor was operated using a constant temperature anemometer circuit at a resistive overheat of 1.4. Initial testing revealed that the sensor tended to drift due to the cold resistance of the wire decreasing as a function of time. However, the drift disappeared after some hours of operation as the wire resistance stabilized. The source of this drift was not immediately evident but might be due to either some annealing of the metal layers as they were operated, or the burning off of some residual materials remaining from the processing and packaging operations.

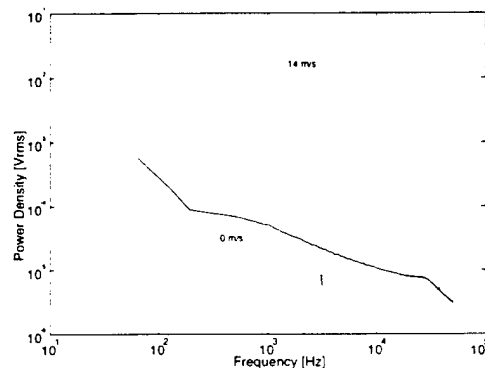


Figure 22: Power spectrum of Shear Sensor measured in a fully turbulent boundary layer. Note the high signal-to-noise ratio achieved and the good frequency response of the sensor.

The sensors showed excellent performance with good frequency response (square-wave response test was limited by the anemometer circuitry which rolled off at 40 kHz). Figure 22 shows a typical power spectrum taken with no flow and then under a turbulent boundary layer at approximate Reynolds number (based on distance from the leading edge of the flat plate) of 1 million. An excellent signal-to-noise ratio is observed, and this could probably be improved further by using more sensitive anemometer electronics or perhaps a greater overheat ratio.

CONCLUSIONS

We have demonstrated the design, fabrication and testing of new shear stress and temperature sensors. The sensors have been found to be robust and to have good sensitivity for measurements in air. Measurements in other fluids, such as water, should be possible, although an insulating layer, might need to be deposited over the sensor element to prevent electrical shorts in a conducting medium. The use of microfabrication techniques is not completely new in the fabrication of shear sensors and at many other groups have demonstrated shear sensors using MEMS-based anemometers. What makes the current devices somewhat distinct is that the supporting membrane in the present case is very thin (1500-Å). This substantially reduces the heat lost to the surrounding substrate. A second distinction is the use of Platinum as the sensor element. Platinum has some advantages over polysilicon in that the Platinum sensor resistance is typically much lower and the metal has a higher temperature coefficient of resistivity. All of these effects contribute to a sensor with improved sensitivity and lower noise characteristics. For example, Kälvesten reports power dissipation of approximately 42 mW and a thermal time constant of 7 ms (~140 Hz) compared with the present results of approximately 8 mW and less than 1 ms respectively.

REFERENCES

- Kälvesten, E., Lofdahl, L & Stemme, G. 1996. "An Integrated Silicon Based Wall Pressure-Shear Stress Sensor for Measurement in Turbulent Flows". *Sensors and Actuators*.
- Lui, C, Tai, Y-C, Huang, J-B, & Ho, C-M. 1994. "Surface Micromachined Thermal Shear Stress Sensor". In *Application of Microfabrication to Fluid Mechanics*. Ed Bandyopadhyay et al. ASME FED 197.
- Padmanabhan, A. Goldberg, H.D. Breuer, K.S. & Schmidt, M.A. 1995 . "A Silicon Micromachined Floating-Element Shear-Stress Sensor with Optical Position Sensing by Photodiodes". *Proceedings of Transducers '95*. Stockholm.

Pan, T., Hyman, D. Mehregany, M. Reshotko, E. & Willis, B. 1995. "Characterization of Microfabricated Shear Stress Sensors" *16th International Congress on Instrumentation in Aerospace Simulation Facilities*. Dayton, OH.

Schmidt, M., Howe, R.T., Senturia, S.D. & Haritonidis, J.H. 1988. "Design and Calibration of a Microfabricated Floating-Element Shear-Stress Sensor". *IEEE Transactions on Electron Devices*. ED-35 pp.750-757.

Final Report
AFOSR Grant F49620-97-1-0526

**MEMS-BASED CONTROL FOR AIR BREATHING PROPULSION:
EXTERNAL JET FLOW**

by

Thomas C. Corke

University of Notre Dame
Aerospace & Mechanical Engineering Department
Hessert Center for Aerospace Research
Notre Dame, IN 46556

Summary

This work was aimed at the use of an azimuthal array of actuators, placed around the nozzle of an axisymmetric jet, to control the unsteady initial condition of instability modes which affect jet spreading and radiated acoustic tones. The jet control was designed to couple the shear layer instability modes with the jet column mode. The shear layer modes included both axisymmetric and helical modes in different combinations. Closed-loop control utilized arrays of sensors placed near the end of the potential core, and in the shear layer. The optimum locations and configurations of these were investigated. Instantaneous time series are constructed from these and used as input to the actuators to produce an electronic feed-back. We documented the results of different feedback configurations which involved excitation at the most unstable column mode frequency, f_c and shear layer frequencies which correspond to $2^n f_c$, for axisymmetric or helical modes alone, or $2^n f_c$ and $2^{n-1} f_c$ to promote shear-layer-mode resonance. In these cases, n , was an integer in the range from 1 to 3. The concept was that the excitation frequency to the shear layer could lead to the frequency of the column mode through a subharmonic cascade (sequence of pairings). The excitation involved helical modes with azimuthal numbers from 1 to 8. Two types of actuators were used. The first which was meant to demonstrate the conceptual approach, consisted of an azimuthal array of miniature speakers. The second approach used an azimuthal array of phased plasma actuators. The actuators and methods were able to couple the shear layer and column modes. In terms of the mean flow, this could produce faster spreading depending on the mode combinations. For example, although higher azimuthal mode numbers produced an initially faster spreading ($x/D \leq 1$), further downstream where the column mode amplitude was a maximum, these became less effective compared to axisymmetric modes. The results lead to a strategy for coupling the two types of jet modes which could affect the jet down to the end of the potential core.

1 Background

Passive approaches to modify jets have been used in the past to control jet spreading. These have included protrusions or "tabs" which extend into the flow at the exit plane of the jet. Ahuja & Brown (1989) found a substantial increase in spreading with tabs in a supersonic jet. Such tabs were also found to reduce screech noise as was documented by Zaman, Samimy & Reeder (1991). The primary effect of the tabs is to produce a distortion of the mean flow which persists for many diameters downstream. In the flow visualization of Zaman, Samimy & Reeder (1991), the distortion produced by each tab resulted in the formation of a streamwise vortex. The tabs are typically placed in even azimuthal increments around the exit face of the jet (for example every 180° or 90°). These result in a nonaxisymmetric spreading of the jet in a pattern in which the jet cross-section varies as $\cos(2\pi m)$, where m is the number of tabs.

The effect of such tabs on the azimuthal variation of the jet spreading is similar to that produced by introducing pairs of helical modes in round jets. An example of this was performed by Corke & Kusek (1993). They used an azimuthal array of 12 speakers, located on the exit face of the jet. The speakers were operated to introduce a periodic pressure fluctuation at a prescribed frequency, with an amplitude which varied around the jet as $A(\gamma) = \cos(m\gamma)$, where γ is the azimuthal coordinate angle and m is the azimuthal mode number of pairs helical modes. In their experiment, $0 \leq m \leq \pm 6$, with $m = 0$ referring to an axisymmetric mode, and ± 6 being the upper limit for 12 speakers.

Corke & Kusek (1993) focused on conditions where disturbances to excite $m = \pm 1$ modes were introduced separately as well as simultaneously with an $m = 0$ mode. In the latter, the $m = \pm 1$ mode was at the subharmonic frequency of the $m = 0$ mode. In either case, the helical mode was amplified. In combination with the fundamental axisymmetric mode, its spatial amplification was double-exponential, e^{e^x} , because of a resonant interaction. The growth of the helical modes resulted in nonlinear interactions, one of which was a mean flow distortion not unlike that produced by the passive tabs. Starting with linear amplitudes, the resonant growth of the helical modes lead to a 300% increase in the jet spreading over the unexcited jet. This is an example of how natural instability mechanisms can be exploited to maximize control authority in flows.

This same experimental setup was later used by Ahn (1994) in order to develop low-dimensional amplitude models for the growth and interaction of azimuthal modes in round jets. This involved an artificial pressure feedback to control the flowfield and convert the instabilities from local convective to global temporal. This "enhanced feedback" resulted in a steady limit cycle growth of the modes which was not unlike the feedback-resonance condition of jet screech. This work focussed on large azimuthal mode numbers, $m \geq 4$, which were found to interact and lead to non-deterministic switching between modes of a type observed in natural jets (Corke, Shakib & Nagib, 1985). Such switching could account for the types of "regular" and irregular motions observed in the shock cells in the numerical simulations of screeching jets by Zhang and Edwards (1994).

In jets with core Mach numbers, $M_j < 1.2$, the most amplified azimuthal modes are axisymmetric ($m = 0$). Although if the exit shear layer is thin compared to the jet radius, $r_s/\theta_i > 100$, the amplification rates of helical modes with azimuthal mode numbers $1 \leq m \leq 6$, are essentially indistinguishable. At larger jet Mach numbers (> 1.2), helical modes with three possible angles can occur. At a given Mach number, there is a helical angle which

maximizes the mixing (Nixon, 1994). Conversely, there are angles at which mixing can be suppressed.

For helical modes, the acoustic Strouhal number is

$$S_t = \frac{fD}{U_j} = \frac{U_c D}{U_j \lambda} \quad (1)$$

where λ is the streamwise wavelength. The wavelength is related to the helical mode angle θ as

$$\lambda = 2\pi r_{.5} \tan(\theta) \quad (2)$$

where $r_{.5}$ is the radius of the initial shear layer defined where $U/U_j = 0.5$. In terms of the frequency and azimuthal mode number,

$$\tan(\theta) = \frac{U_c m}{r_{.5} f} \quad (3)$$

therefore,

$$S_t = \frac{r_{.5} f}{\pi U_j m} \quad (4)$$

The most amplified Strouhal number is given by the stability characteristics of the shear layer and jet core. For higher flow rates, $S_t = fD/U_j$ is a constant equal to 0.44 (Kibens, 1981 and Drubka, 1981). To force a jet at frequencies away from the most amplified Strouhal number requires more energy. However, Eq[4] indicates that one can maintain the most amplified Strouhal number and change the frequency by simultaneously changing the azimuthal mode number, m .

1.1 Control Approach

Our overall objective was to control instability modes in order to modify the unsteady characteristics of jets that affect mixing and sound generation. Evidence in the literature points to the primary sound generation sites to be near the end of the potential core. Therefore our focus included the the jet column mode instability. Because this instability scales with the jet diameter, its most amplified band of frequencies is an order of magnitude smaller than the most amplified shear layer mode frequency, which scales with the shear layer thickness. The column mode is most amplified in the downstream region approximately 4-5 diameters from the jet exit.

In a jet, the only feasible location for an actuator array is at the jet exit. Past experience demonstrates that it is not efficient to excite the shear layer at the lower, column mode frequency, since it is generally well outside the most amplified range. However, there are instances in natural jets (Drubka, 1981) when the shear layer mode couples efficiently with the column mode. This occurs when the shear layer frequency is related to the column mode frequency by an integer power of 2 (2^n). Thus, the shear layer frequency can reach the column mode frequency through a succession of vortex pairings (usually three). When this condition exists, there is a strong pressure feedback to the point of receptivity, which is the exit edge of the jet. In this way there is a degree of self-forcing which leads to a weak resonance. Under this condition, the jet instability is extremely organized.

monic ($4f_c$) helical mode. The second highest peaks are at the second subharmonic ($2f_c$), and the column mode frequency. $2f_c$ is an interacted mode which is not directly seeded. We note that the spatial location of the amplitude peak for the f_c has moved to the center of the shear layer with the forcing, and it is very sharp. A significant coherence (phase locking) was found for the three modes at f_c , $4f_c$ and $8f_c$.

Spectra at different streamwise locations in the shear layer were combined to produce 2-D spatial eigenmode mode plots. An example of these for the unforced jet is shown in Figure 9. These show contours of constant amplitude in percent u'/U_j for the four frequencies of interest, f_c , $2f_c$, $4f_c$ and $8f_c$.

For the column mode, near the jet exit, we observe a central peak on the shear layer centerline, and two higher amplitude lobes on either side of the centerline. Any of these would be ideal locations to monitor the energy in the column mode with sensors mounted close to the jet exit. In a heated jet, the location outside the centerline may be preferable since it would be further from the hotter core air (a constraint for some MEMs sensors).

In general, the streamwise locations of the amplitude peaks increases as the frequency decreases. Thus $8f_c$ reaches a maximum the closest to the jet exit. At this Reynolds number, this is at $x/D = 0.5$. The exact location scales with the shear layer frequency, and generally corresponds to three wave lengths of the fundamental shear layer mode. The subharmonic mode generally reaches its maximum at four wave lengths of the fundamental mode (two of the subharmonic) from the jet exit. This is at $x/D \simeq 0.6$ in the present case.

The two lowest frequency modes, $2f_c$ and f_c , reach their maximum amplitudes much further downstream, at $x/D \simeq 2$ and 2.5 , respectively. In the unforced jet, the largest streamwise fluctuations correspond to the column mode. This is true both for the peak values as well as for a spatially integrated value.

The 2-D eigenmodes for the four modes with close-loop forcing are shown in Figure 10 and 11. Because this case involves a $m = \pm 2$ helical mode at the frequency $4f_c$, the amplitude periodically varies in the azimuthal direction in a standing pattern (such as in Figure 2). In order to present this, the 2-D eigenfunctions are shown for two azimuthal locations corresponding to the amplitude maximum and minimum. The azimuthal variation is evident in the maximum amplitudes of the eigenfunctions for $4f_c$ in the top part of Figure 10b, where at the maximum, u'/U_j is approximately three times higher than at the minimum.

As expected with the forcing, the amplitudes of the four modes are all higher than in the unforced case. This is especially true of $4f_c$, $2f_c$ and f_c . This was part of the objective in the control approach because the lower frequencies are less amplified and generally more difficult to force than the most amplified shear layer mode. The shear layer mode in this case, $8f_c$, is at nearly the same amplitude as in the unforced case. This reflects the difficulty in controlling the jet by this mode alone, because its amplitude quickly saturates due to nonlinear effects.

Considering the column mode, the forcing at f_c was axisymmetric. However, the top part of Figure 10a reveals that there is an azimuthal variation in its amplitude. In fact, the highest amplitude levels occur at the azimuthal location where the excited $4f_c$ helical mode amplitude was a minimum. Compared to the unforced case, these levels are approximately 1.5 times larger past $x/D = 2$. This demonstrated the ability of the control approach to excite higher column mode amplitudes further downstream, while using actuators at the jet exit.

A further assessment of the effect of the closed loop forcing on the four frequencies

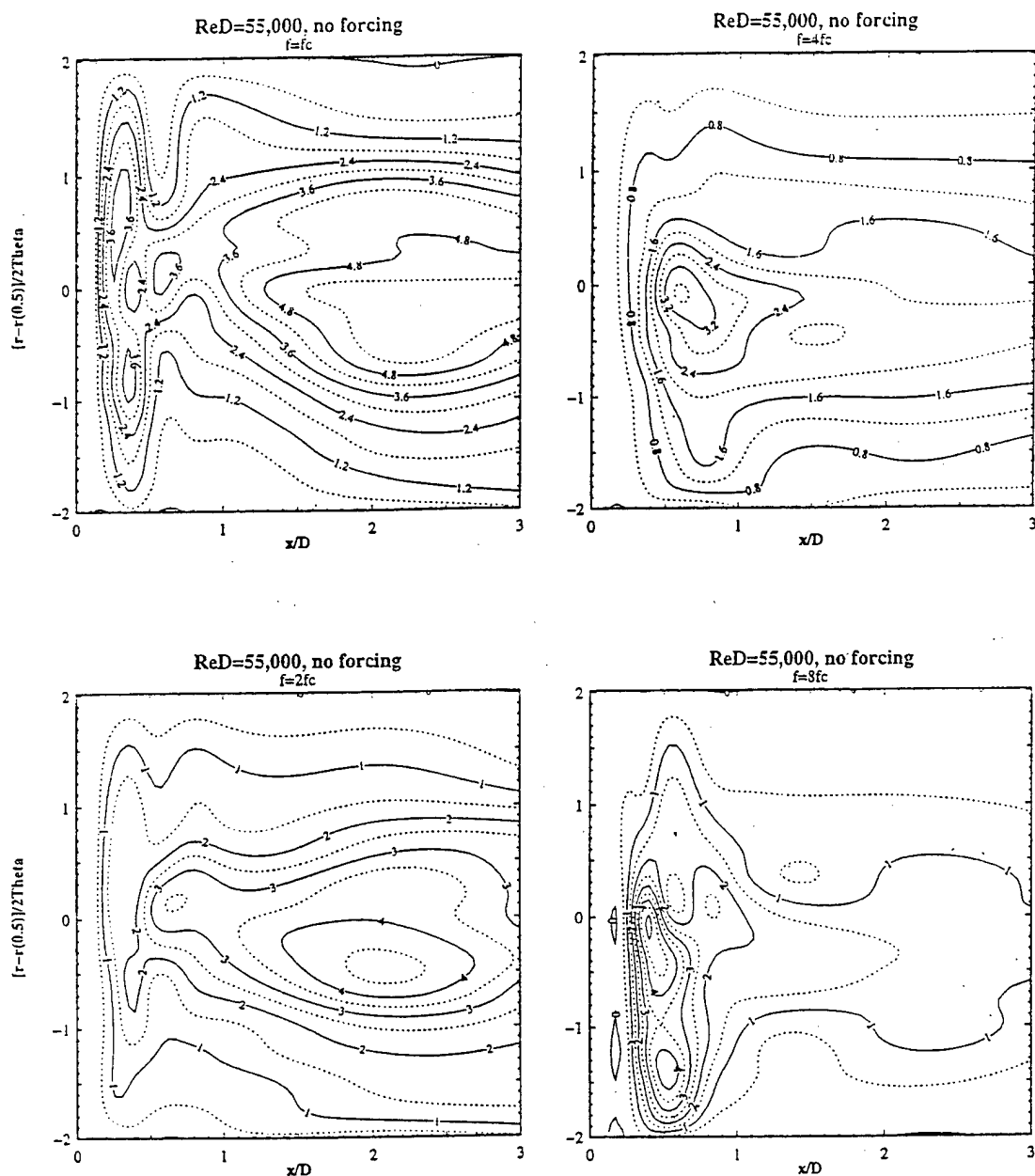


Figure 9: Contours of the 2-D spatial eigenfunction for the four modes f_c , $2f_c$, $4f_c$ and $8f_c$. $Re_D = 55,000$, no forcing.

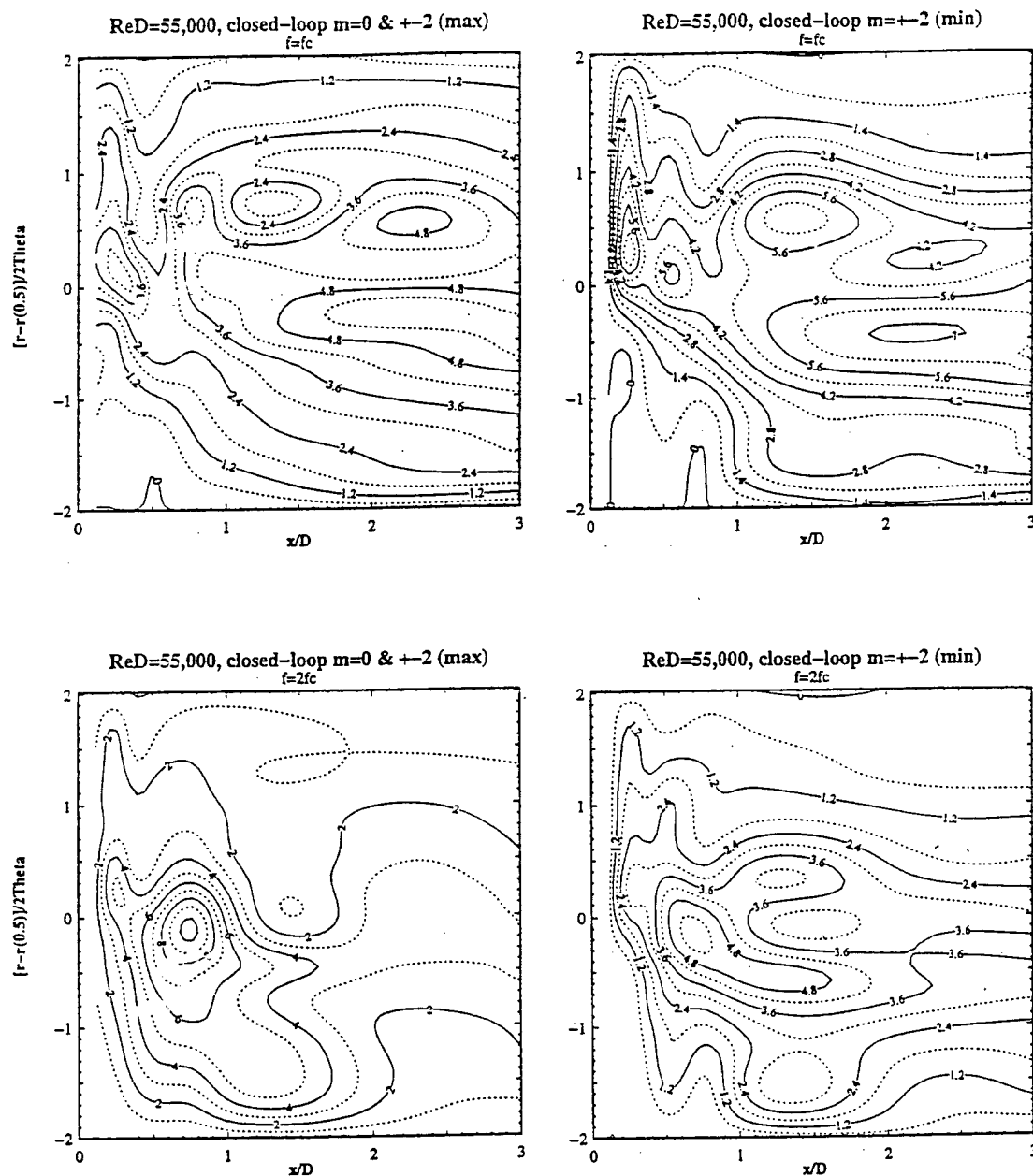


Figure 10: Contours of the 2-D spatial eigenfunction for the two modes f_c and $2f_c$ at two azimuthal positions corresponding to the amplitude maximum and minimum of the helical mode at $4f_c$. $Re_D = 55,000$, closed-loop forcing.

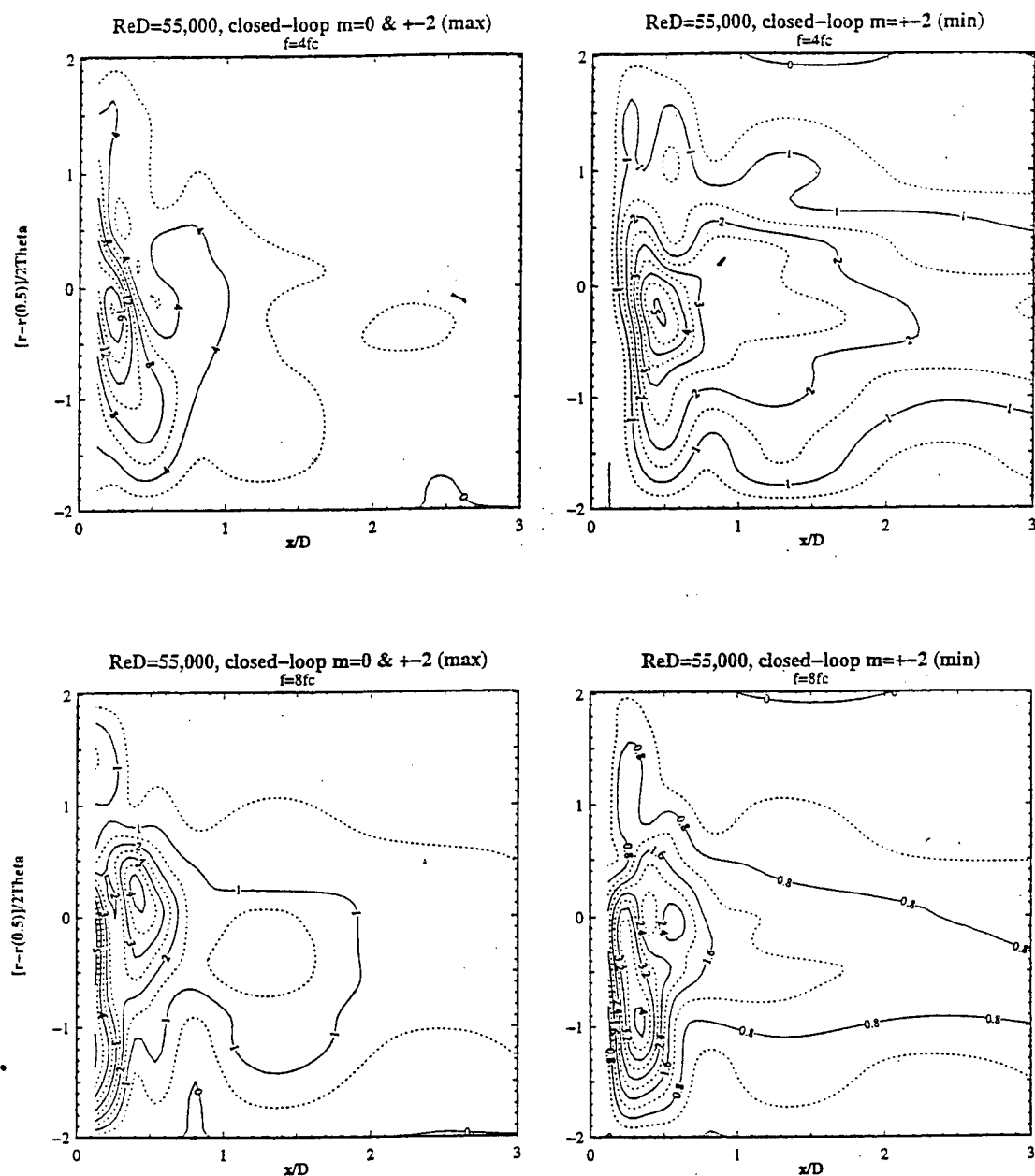


Figure 11: Contours of the 2-D spatial eigenfunction for the two modes $4f_c$ and $8f_c$ at two azimuthal positions corresponding to the amplitude maximum and minimum of the helical mode at $4f_c$. $Re_D = 55,000$, closed-loop forcing.

comes from examining the streamwise development of their amplitude and phase locking (coherence). This is presented in Figure 12. In this figure, the amplitude at a given x/D corresponds to the maximum amplitude at that location in the shear layer. The left column corresponds to the azimuthal location of the $4f_c$ amplitude minimum. The right column corresponds to the $4f_c$ amplitude maximum. The top row in Figure 12 corresponds to the coherence between two hot-wires in the shear layer. One of the hot-wires is at the exit of the jet. The other moves in (x, r) space. The coherence value at any x/D corresponds to the maximum value irrespective of the radial position in the shear layer.

Focusing first on the amplitudes in the bottom part of Figure 12, far downstream, the amplitudes are always higher for the lower frequency modes. Near the exit of the jet, at the azimuthal location where $4f_c$ is a maximum, the $4f_c$ mode starts with the largest amplitude, and then proceeds through a subharmonic cascade through $2f_c$ and finally f_c so that it is ultimately the largest in amplitude past $x/D = 1.5$.

The coherence at the top of Figure 12 reveals that the column mode at f_c has significant phase locking far downstream, especially at the azimuthal position where the amplitude of $4f_c$ is a minimum. The azimuthal location where $4f_c$ is a maximum significantly increases the extent of its high coherence. This eventually raises the coherence of the other modes, although the level of coherence for f_c is somewhat lower at the furthest downstream location for this azimuthal position.

The ultimate effect of the closed-loop forcing is documented through the streamwise development of the mean velocity. Figure 13 shows a comparison of iso-velocity lines, U/U_j , across the shear layer without and with closed-loop forcing. The radial position is normalized by the local momentum thickness. The degree to which the iso-velocity lines are parallel and smooth is an indication that the local momentum thickness is a representative measure of the shear layer spreading.

The effect of the different closed-loop mode combinations on the shear layer spreading is documented in Figure 14. The top plots correspond to cases where f_c , and $8f_c$ with different azimuthal mode numbers, were combined. The lower plots correspond to cases where f_c , $8f_c$ with $m = 0$, and $4f_c$ with different azimuthal mode numbers, were combined. For reference in both plots, the spreading with open-loop forcing, as well as for the unforced jet, are included. The distribution for the unforced jet is highlighted by the dashed curve for more easy reference to the other points.

Focusing on the top plot, upstream of $x/D = 1$, all of the forced cases (open and closed) spread at a faster rate than the unforced jet. Also in this upstream region, the cases with the higher azimuthal mode numbers generally spread faster (see inset). This is the region where the amplitude of the shear layer modes are increasing exponentially. As a result, the shear layer spreading is nonlinear with x/D .

For $x/D > 1$, in the top plot, a different pattern of development emerges. Here the highest spreading now occurs for the lowest azimuthal mode numbers ($m = 0$), and the close-loop $m = \pm 6$ case actually has less spreading than the unforced jet. We note however that except for the $m = \pm 6$ case, the spreading in all of the closed-loop cases exceeded that of the open loop forced case.

Focusing now on the bottom plot, the addition of the subharmonic helical modes substantially increased the initial ($x/D \leq 1$) spreading of the shear layer. One difference with the previous cases is that with the subharmonic helical mode present, there is very little dependence of the spreading on the azimuthal mode number in the initial region.

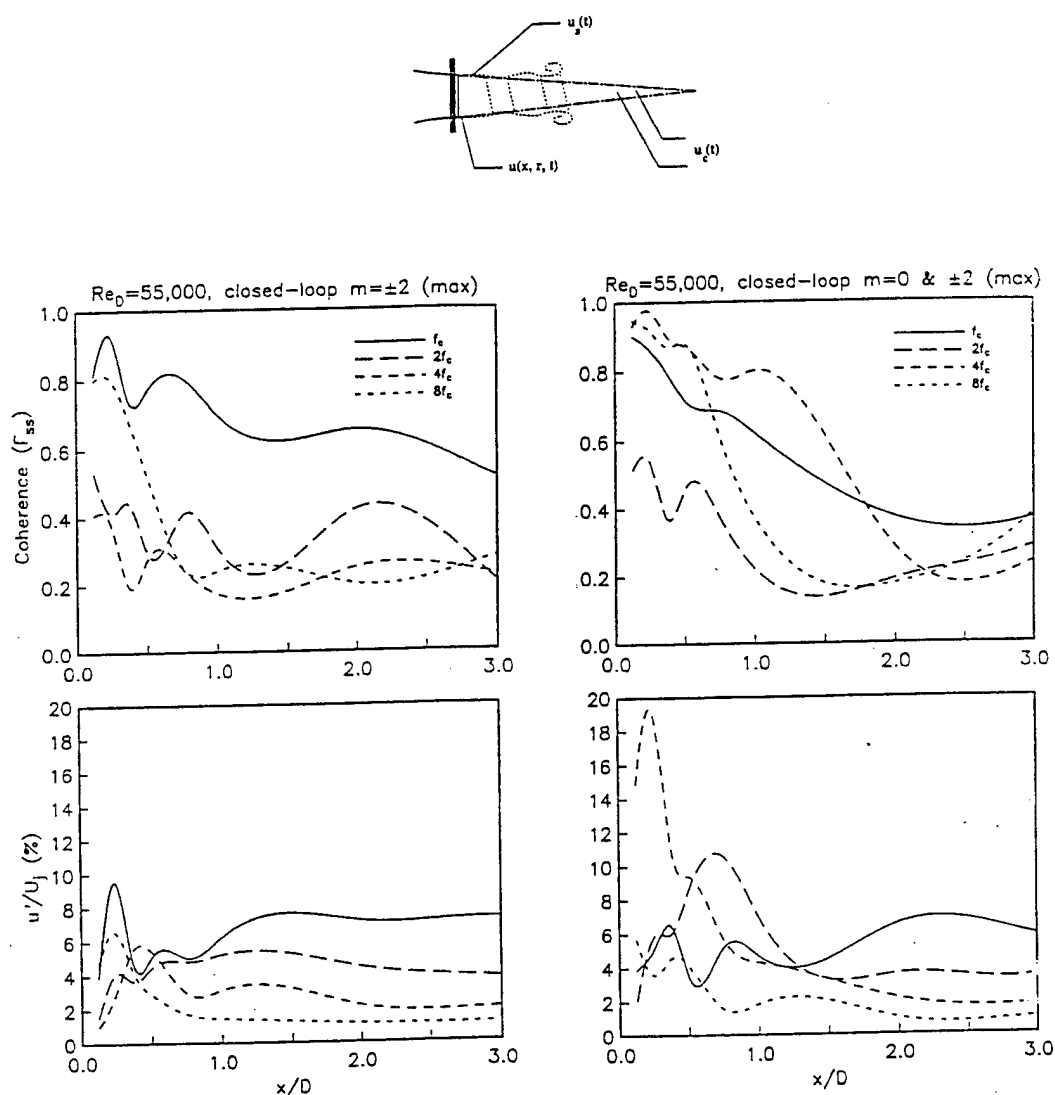


Figure 12: Streamwise development of coherence and maximum amplitude for the four frequencies at two azimuthal positions corresponding to the amplitude minimum (left) and maximum (right) of the helical mode at $4f_c$. $Re_D = 55,000$, closed-loop forcing.

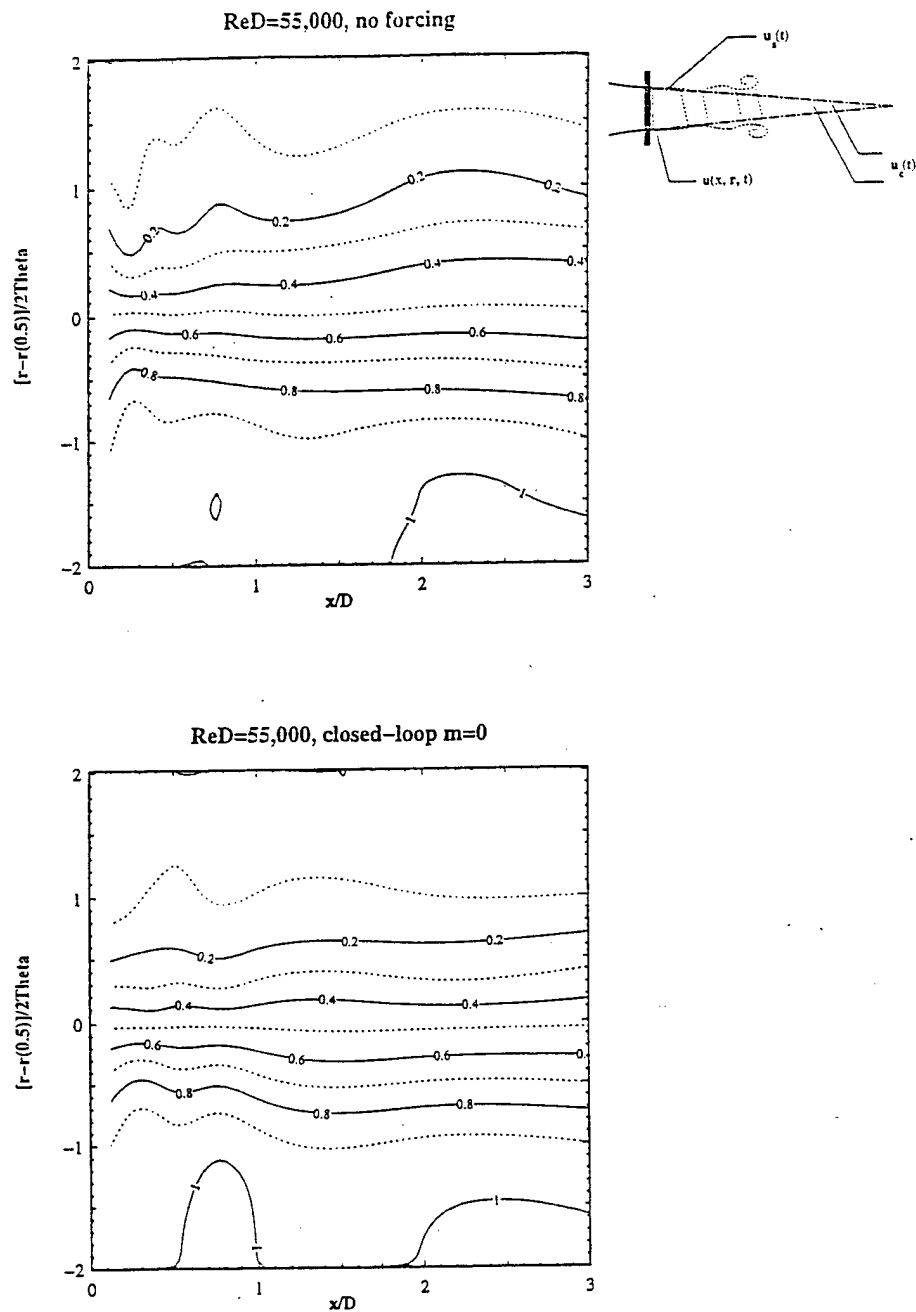


Figure 13: Iso-velocity contours of U/U_j for two representative cases.

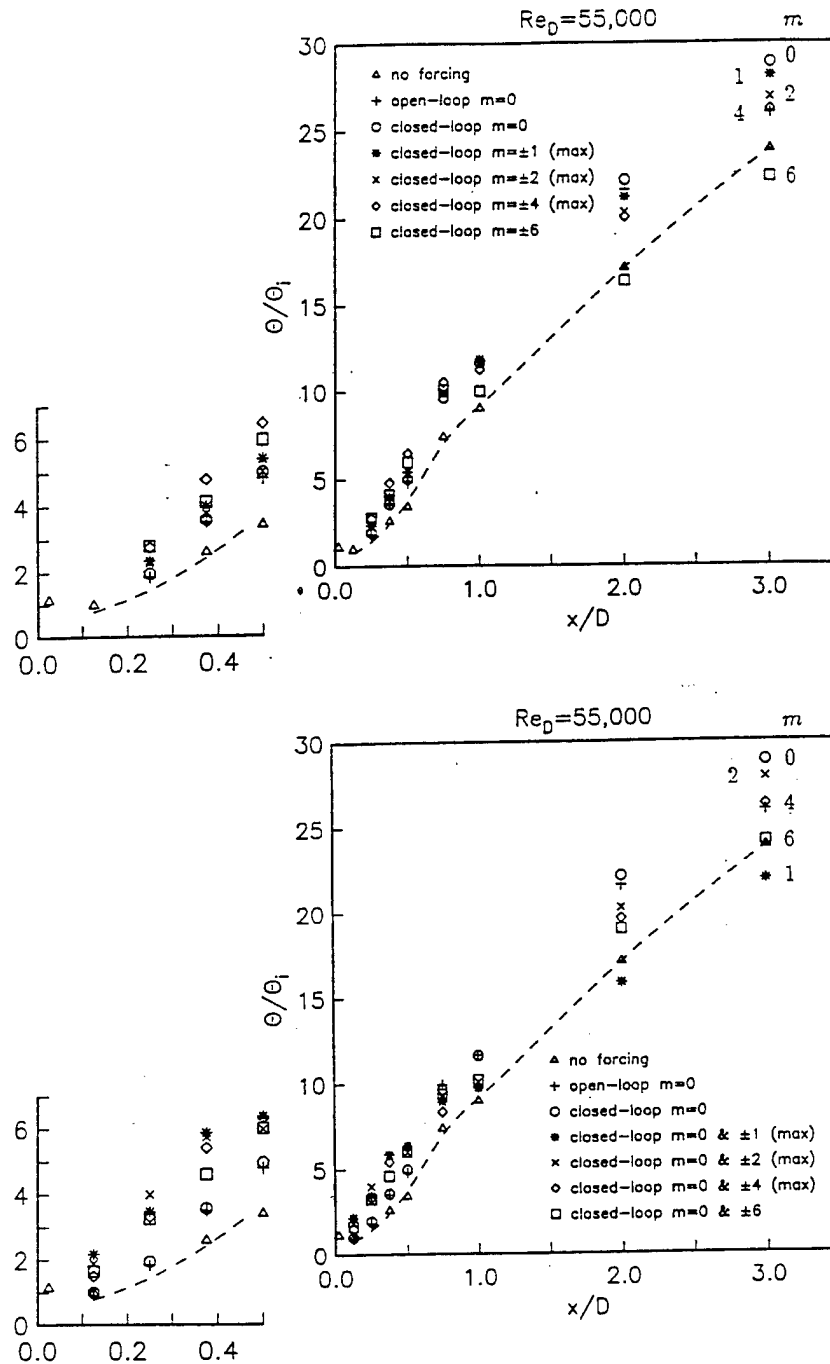


Figure 14: Effect of different mode combinations and azimuthal mode numbers on shear layer momentum thickness growth.

For $x/D > 1$, in the bottom plot, the final shear layer thickness is similar to the top plot with one exception. Here we find that rather than having one of the largest amounts of spreading, the case with $m = \pm 1$ now has the lowest spreading, below that of the unforced jet. The highest shear layer thickness at $x/D = 3$ corresponds in order, to $m = 0, 2$ and 4 . At this location, the shear layer thickness for the $m = \pm 6$ case is the same as the unforced jet.

Another global indication of the mean development of the jet is the centerline mean velocity decay. This is documented in Figure 15 for the two types of closed-loop forcing. As with Figure 14, the top plot corresponds to cases where f_c , and $8f_c$ with different azimuthal mode numbers, were combined. The bottom plot corresponds to cases where f_c , $8f_c$ with $m = 0$, and $4f_c$ with different azimuthal mode numbers, were combined. Also as before, the dashed curve corresponds to unforced jet.

The results for the two types of forcing are nearly the same. That is, we observe a faster centerline decay as the azimuthal mode number decreases. Except for $m = \pm 6$, the centerline decay of all of the other forced cases exceeded the unforced jet.

Overall, the fastest centerline decay occurs with $m = 0$. This is consistent with the previous results, which showed the largest shear layer spreading for $m = 0$. However in contrast to the previous results, for the centerline decay, there is little difference between the open-loop and closed loop forcing.

4 Phased Plasma Actuators

4.1 Background

An extensive effort has been made on the development of actuators which are based on the concept of producing a plasma in a localized region to generate unsteady vortical disturbances. The plasma is produced over electrodes which are located on a surface, where it can excite a boundary layer or separated shear layer. This type of actuator has been used by us in the past to excite instability modes in Mach 3.5 laminar boundary layers (Cavaliere, 1995; Corke et al., 1997, 2000).

Our approach in fluid flow control applications is based on radio-frequency (RF) glow discharge (Kanda *et al.*, 1991; Roth *et al.*, 1992.). This method applies an a.c. voltage potential across the electrodes. The frequency of the a.c. must be such that within a period, electrons can travel to the electrodes and generate a charge, but the heavier ions cannot. The condition on frequency (given by Roth, 1995) is

$$f_0 \simeq \frac{(e/m)_e V_{rms}}{\pi \nu_{ce} d^2} \quad 6$$

where d is the electrode spacing, V_{rms} is the root-mean-square of the a.c. voltage potential, ν_{ce} is the collision frequency for electrons, $(e/m)_e$ is the electron charge-to-mass ratio, and the frequency f_0 has units of Hertz.

The RF glow discharge exhibits all the phenomenology of classic d.c. glow discharge (Gadri and Roth, 1998). In addition, it operates at the minimum breakdown (Stoletow) point. The properties of a dielectric barrier (Massines *et al.*, 1998) adds another element which can be used to enhance the efficiency of producing uniform plasmas over large surfaces.

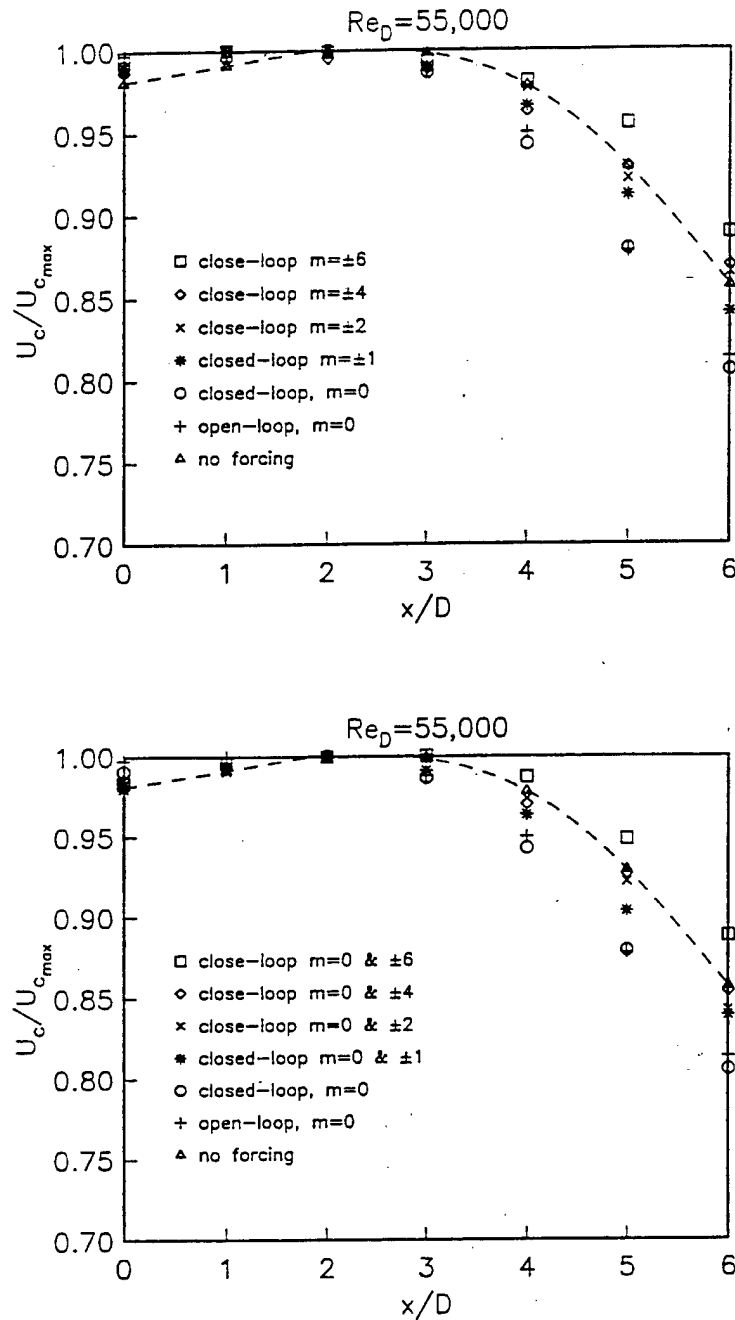


Figure 15: Effect of different mode combinations and azimuthal mode numbers on the centerline velocity decay.

The polarization electric field causes charges and plasma to move to regions of increasing electric field gradients. In the process, the neutral gas is “dragged” along due to Lorentzian collisions. Roth, Sherman and Wilkinson (1998) formulated this effect as an “electrostatic body force” given as

$$B_E = \frac{1}{2} \epsilon_0 \nabla \cdot E^2 \quad 7$$

where ϵ_0 is the permittivity of free space (8.854×10^{-12} F/m), and E is the electric field strength (V/m). In one-dimension,

$$B_E = \frac{d}{dx} \underbrace{\left(\frac{1}{2} \epsilon_0 E^2 \right)}_{P_E} \quad 8$$

where the term in the bracket has units of pressure. Therefore, B_E represents a pressure gradient which is induced by the plasma. Roth, Sherman and Wilkinson (1998) demonstrated this effect by the bending of a smoke stream above a pair of electrodes which were producing a plasma.

4.2 Phased Plasma Array

With the speaker array used in the earlier work, helical modes pairs of equal but opposite wave numbers (angles) were excited by using a periodic time series with an amplitude which varied azimuthally according to $\cos(2m\pi)$. This worked well with the speakers, because they have a large amplitude range. For the plasma actuators, the amplitude range is not as large. Therefore for the plasma actuators, the helical mode excitation was produced by time series which were phase shifted in the azimuthal direction around the jet nozzle.

The problem of phase shifting an array of plasma actuators has only recently been solved by us in DARPA sponsored research. Our approach is illustrated in Figure 16. This uses an array of lower electrodes (cathodes), which are labeled $1, 2, \dots, N$. Rather than ground the cathode as is typically done, an a.c. voltage is applied such that

$$V = V_0 \sin(\omega t - kx) \quad 9$$

where k is the x wave number given as

$$k = \frac{2\pi}{\lambda} = \frac{2\pi}{(N)L} \quad 10$$

Here N is the number of cathodes corresponding to one period of the sine input, and L is the total distance spanned by N cathodes of width, w , and spaced s apart.

Generally, there is an optimum a.c. frequency for generating a plasma which is dependent on the gap between electrodes and the properties of the dielectric insulator material. It may only be fortuitous that this frequency corresponds to the desired actuation frequency, which for the jet, depends on the most amplified Strouhal numbers. Therefore it is necessary to decouple the actuation frequency from the a.c. frequency which optimally produces the plasma. The method to achieve this is illustrated in Figure 17.

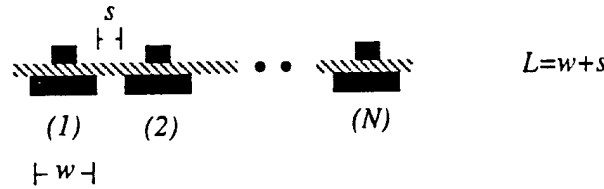


Figure 16: Schematic showing elements of phased-plasma-array.

In Figure 17 each of the time series corresponds to a short-duty square wave. The electrodes on the lower side of the insulator are labeled (2) through (6). These are supplied with the correspondingly numbered time series. Each of these are phase shifted by an equal amount ($2\pi/N$ radians) so that τ_1 corresponds to one full period.

The electrodes on the upper side of the insulator are all electrically connected and supplied by the single time series labeled (1). The period of that time series is τ_2 where $\tau_2 \neq \tau_1$. For the conditions shown, $\tau_2 < \tau_1$. However in general, both frequencies, $f_1 = 2\pi/\tau_1$ and $f_2 = 2\pi/\tau_2$ will be close to the optimum to produce plasmas.

The plasma forms on either side of the electrode on the upper surface where the potential is large enough. In Figure 17, this occurs where there is a conjunction of the high and low states at a particular electrode, such as (3) and (6). Because the frequencies are different between the time series supplied to the upper and lower electrodes, the location of the plasma moves. The phase velocity at which it moves is equal to

$$v_p = 2\pi(f_2 - f_1)L. \quad 11$$

The advantage of this arrangement is that the velocity and direction are controllable through the frequency difference.

The arrangement in Figure 17 is designed to translate the plasma in one direction. In the circular jet, this would excite helical waves with either positive or negative azimuthal mode numbers. In order to produce helical modes of both signs simultaneously, the pattern used in the time series for the lower electrodes in Figure 17 is combined with an identical pattern, which is reversed in time.

4.3 Application for Jet Control

We have applied this concept towards exciting helical modes in an axisymmetric jet. A schematic is shown in Figure 18. In this case the dielectric insulator, made from fiberglass reinforced epoxy sheets, was molded to fit along the inside wall of a straight nozzle extension. Eight (8) electrodes on the outside (labeled 2-9), have inputs with different phase shifts, to excite different helical mode numbers. The time series to excite an $m = 4$ mode is shown in the figure. The plasma forms on the flow-side of the dielectric, on either side of the electrodes labeled (1). The implementation of this concept in a straight extension on the exit of the jet nozzle is shown in the photographs in Figure 19.

The azimuthal position of the plasma travels around the nozzle based on the phase shift between neighbor electrodes, and the frequency difference between the time series supplied to the inner and outer electrodes. This is documented in Figure 20, which shows a movie

● Two-frequency Phased Excitation to Produce Unidirectional Wave.

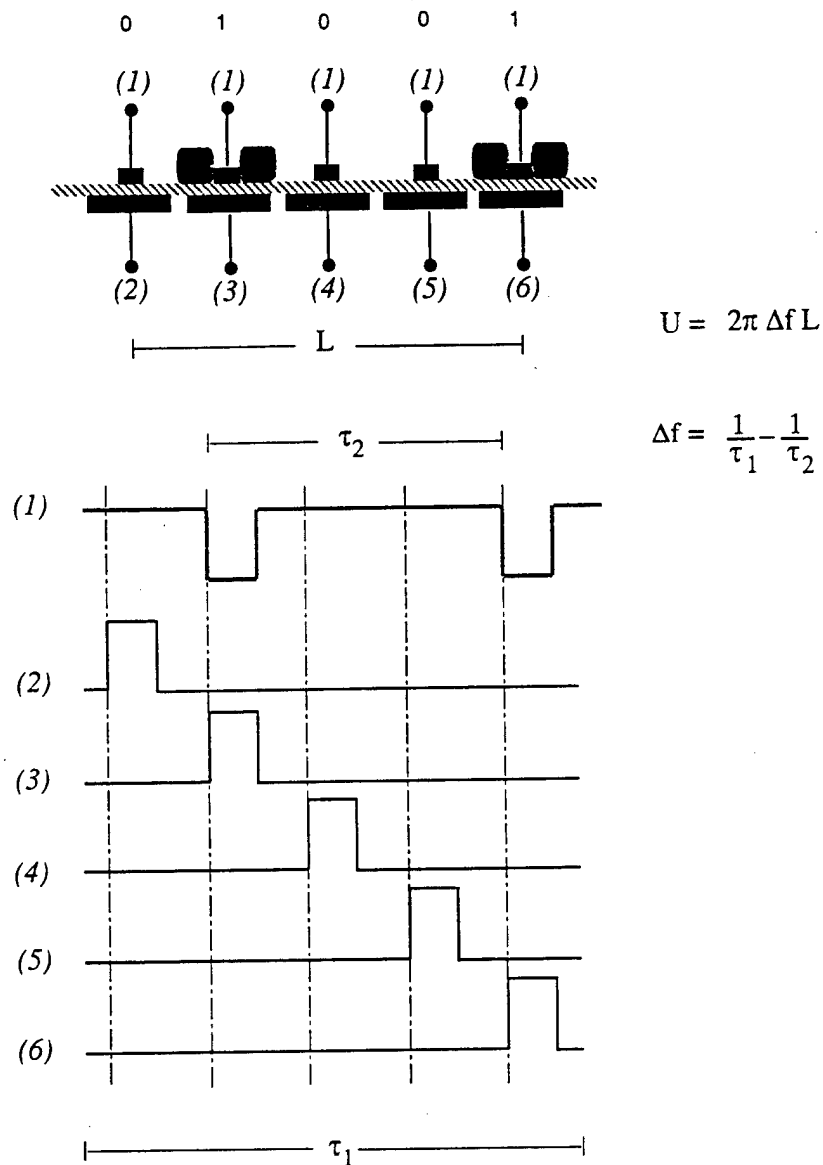


Figure 17: Schematic of two-frequency phased excitation.

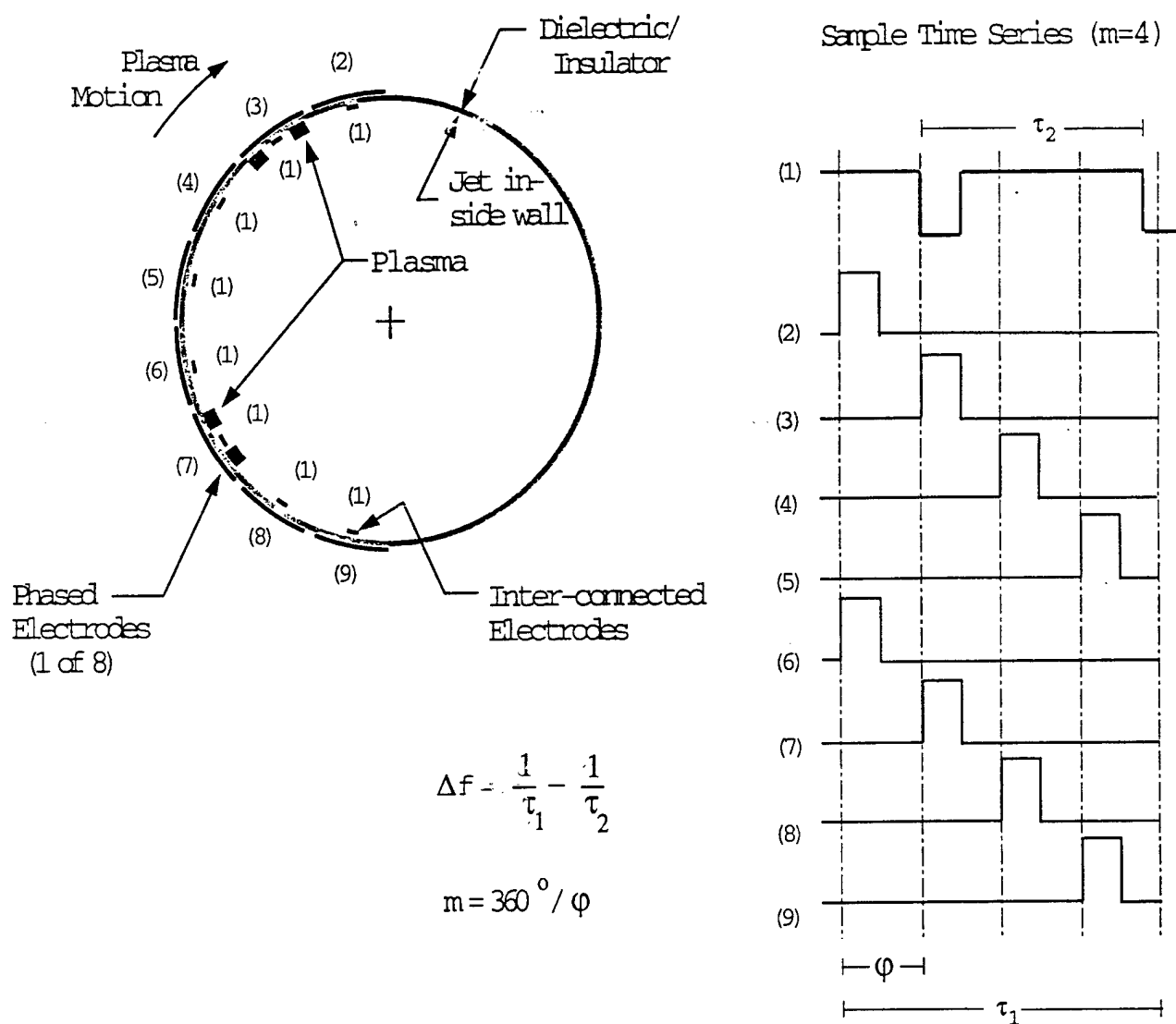


Figure 18: Schematic of two-frequency phased excitation to produce helical disturbances in a round nozzle. Time series at right will produce $m = 4$ mode.

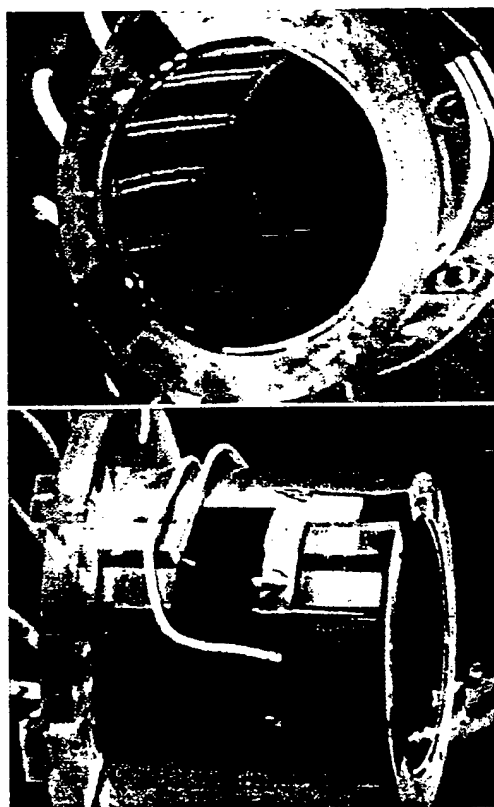


Figure 19: Photograph of nozzle extension showing internal (top) and external (bottom) electrodes.

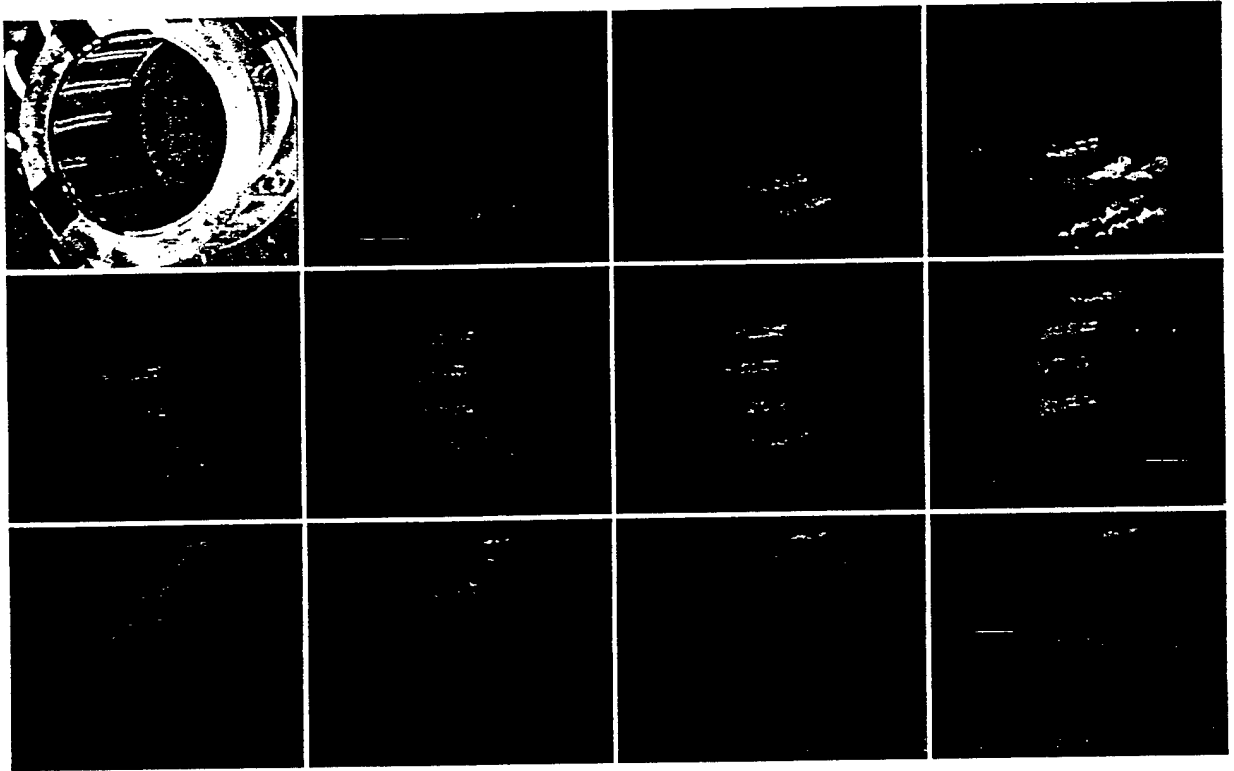
Movie Clip of Plasma Motion to Excite $m=1$ Mode

Figure 20: Sequential movie frames showing plasma motion to excite $m = 1$ helical mode. Time starts at upper left, and increases from left-to-right, and top-to-bottom.

frame sequence for conditions to excite a $m = 1$ helical mode. Time starts in the top-left frame, and increases in each successive frame going from left to right and continuing from the top to bottom rows. In this sequence, the plasma (bright lines) is seen to move around the nozzle, starting from the bottom.

4.4 Column Mode Excitation

The plasma actuator was used to excite the jet column mode at different azimuthal mode numbers in the range $0 \leq m \leq 8$. This investigation is the next step towards the combined excitation which couples the shear layer and column modes, that was presented in the earlier section. The experimental conditions are summarized in Table 1. A schematic of the experimental setup is shown in Figure 21.

The excitation frequency was $f = 266\text{Hz}$, which corresponds to the most amplified $St_D = fD/U_j = 0.44$. The jet Reynolds number was $Re_D = 105,000$, which is approximately twice

that primarily documented with the speaker array in the previous sections. The velocity time series were obtained from a constant-temperature hot-wire, which were digitally sampled. Discrete Fourier analysis of the time series was used to determine the amplitude of velocity fluctuations of the excited mode.

Table 1. Jet experimental conditions.

D	5.08cm
U_j	30.6m/s
Re_D	1.05×10^5
Excitation Frequency	$f = f_c = 266Hz$
Excitation Strouhal No., St_D	0.44 (most amplified)
Excitation Azim. Mode No.	$0 \leq m \leq 8$
Measurement Range	$0.2 \leq x/D \leq 5$ $-0.5 \leq r/D \leq 1.0$

The azimuthal mode number of the actuation ranged from $0 \leq m \leq 8$ with the plasma actuator. In all these cases, velocity time series were acquired across the shear layer, from the jet centerline to the ambient flow, in the range from $0.2 \leq x/D \leq 5.0$. We chose to present representative results for the case with $m = 4$. This case was expected to be interesting because it consistently had the largest global impact on the mean and unsteady properties of the jet in the closed-loop control experiments.

Figure 22 shows spectra without (top) and with (bottom) actuation with $m = 4$ at different downstream locations on the jet centerline. For the unforced jet, the amplitude levels increase systematically with downstream position. At the most upstream location, $x/D = 0.2$, the velocity fluctuation levels are very low, and discrete peaks in the spectrum are due to background electronic noise. These are identical in the unforced and forced jet, and are not due to the actuator.

With the plasma actuator, the excitation frequency was 266Hz, which corresponded to the most amplified column mode Strouhal number of 0.44. The dashed line in both spectra denote that frequency. With the actuator on, there is a clear peak in the spectrum. Other figures to follow will verify this better, but the spectral peak is observed to grow (exponentially) with downstream distance, and ultimately decay. This characteristic alone indicates that the spectral peak is not due to electronic noise, but is fluid-dynamic based.

In addition to the sharp spectral peak at the excitation frequency, we also observe an overall increase in the energy in the band about the excitation frequency. This is especially evident in the lower frequency band at the further downstream locations.

Figures 23 through 25 show the results of velocity measurements from the jet centerline, through the shear layer to the ambient air at different x/D locations for conditions without

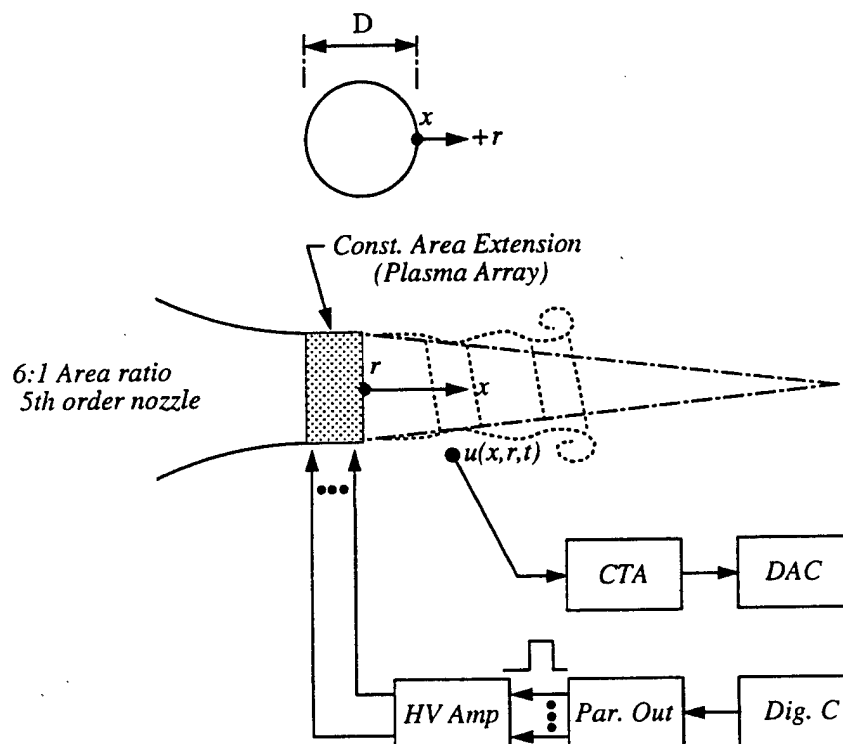


Figure 21: Schematic of setup and coordinates for jet excitation using phased-plasma-array.

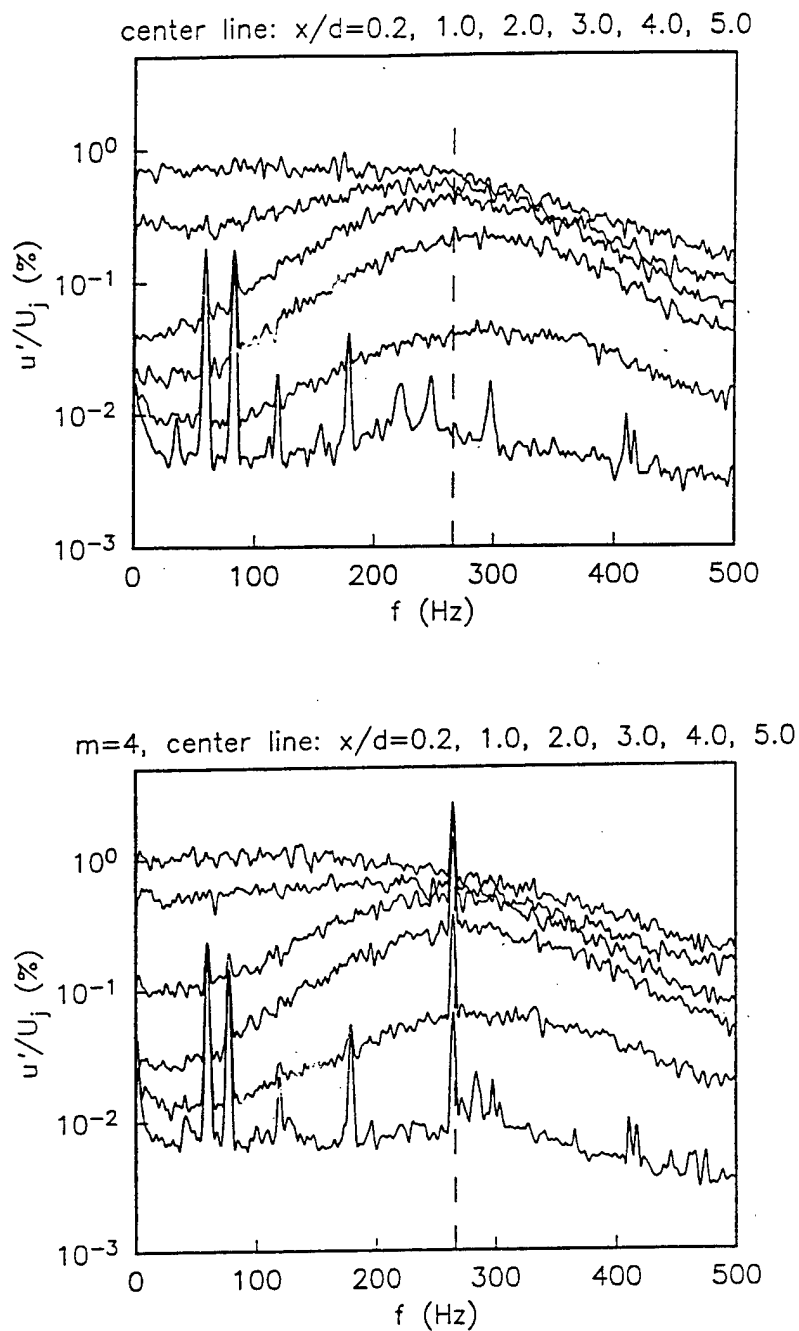


Figure 22: Spectra for the unforced (top) and forced jet (bottom) at different x/D locations on the jet centerline. Forcing conditions are $f = 266\text{Hz}$ and $m = 4$.

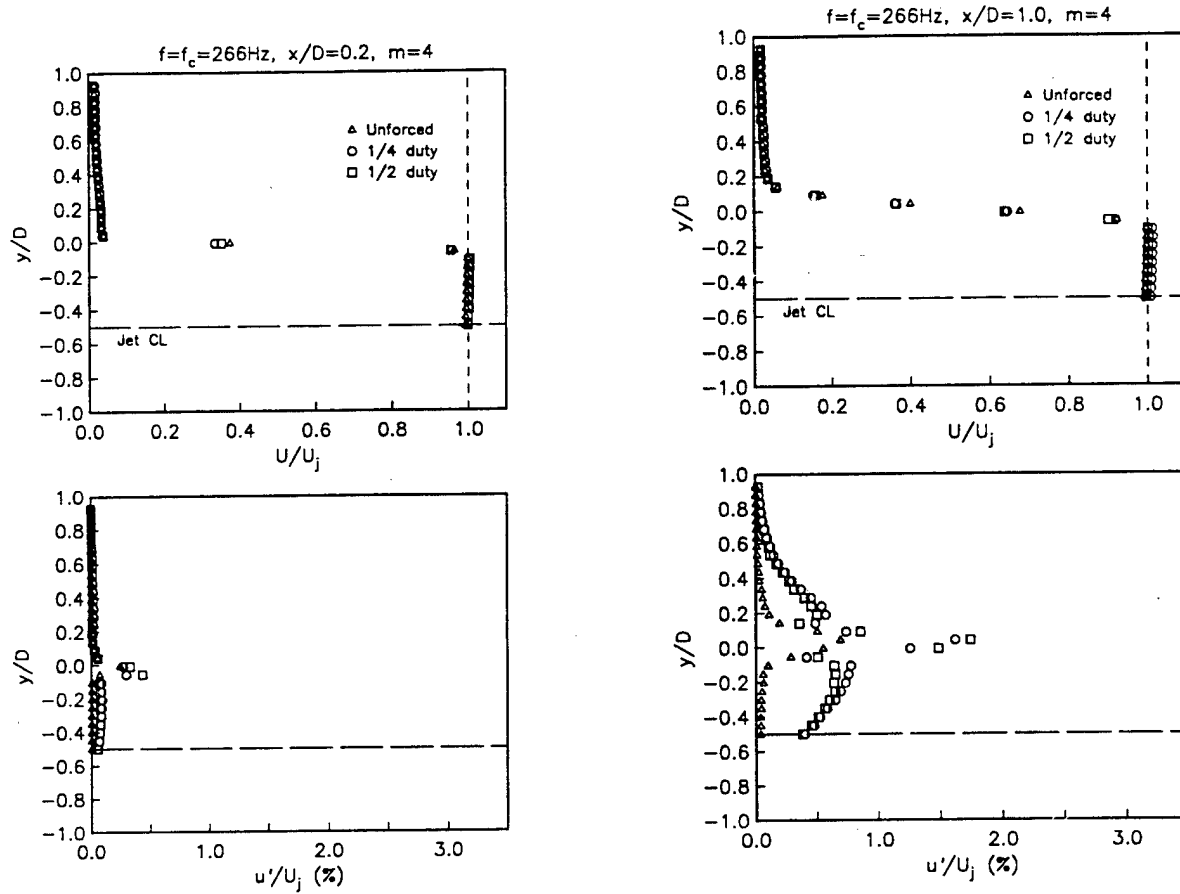


Figure 23: Mean velocity profiles (top) and eigenfunction distributions at the column mode frequency (f_c) without excitation, and with $m = 4$ excitation (two cases). $x/D = 0.2$ (left) and 1.0 (right)

and with actuation with $m = 4$. In these, the top plot corresponds to the mean velocity, \bar{U}/U_j . The bottom plot corresponds to the r.m.s. fluctuations at the column mode frequency, f_c . With the bottom plot, the unexcited (natural) jet case corresponds to the triangle symbols. Two cases with excitation at f_c using the plasma array correspond to circle and square symbols. The difference between them is the duty cycle, which was not expected to have any effect. More significantly, the span of time between measurements represents approximately three months of continual operation of the actuator. The excellent overlap of the data reflects the repeatability of the actuator.

With excitation, there was a significant increase in the amplitude at the column mode frequency. For example, at $x/D = 2$, the peak values increased by approximately 350%. This is normally very difficult to achieve with other actuators, for example, the speakers used in the previous sections.

We note that the amplitude distribution developed a double-peaked shape. This is a

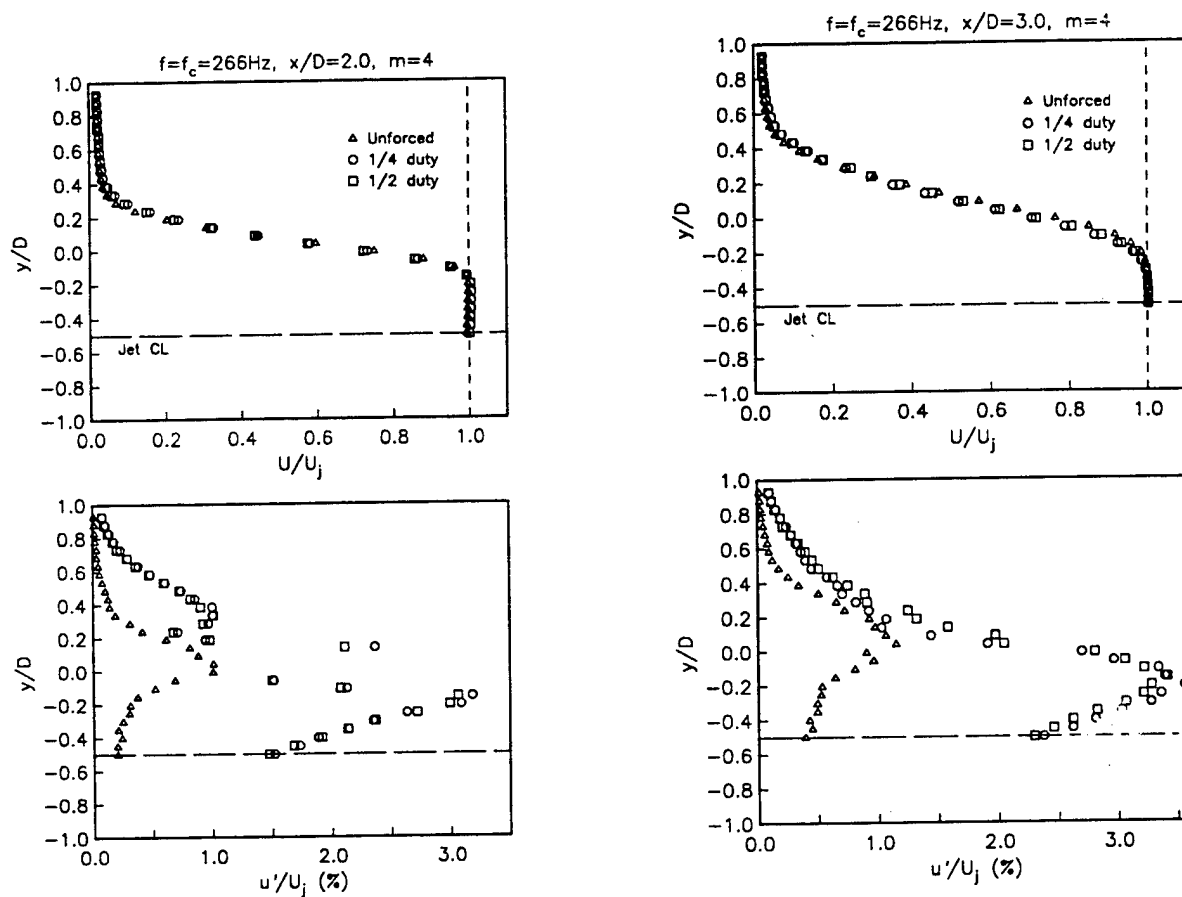


Figure 24: Mean velocity profiles (top) and eigenfunction distributions at the column mode frequency (f_c) without excitation, and with $m = 4$ excitation (two cases). $x/D = 2.0$ (left) and 3.0 (right)

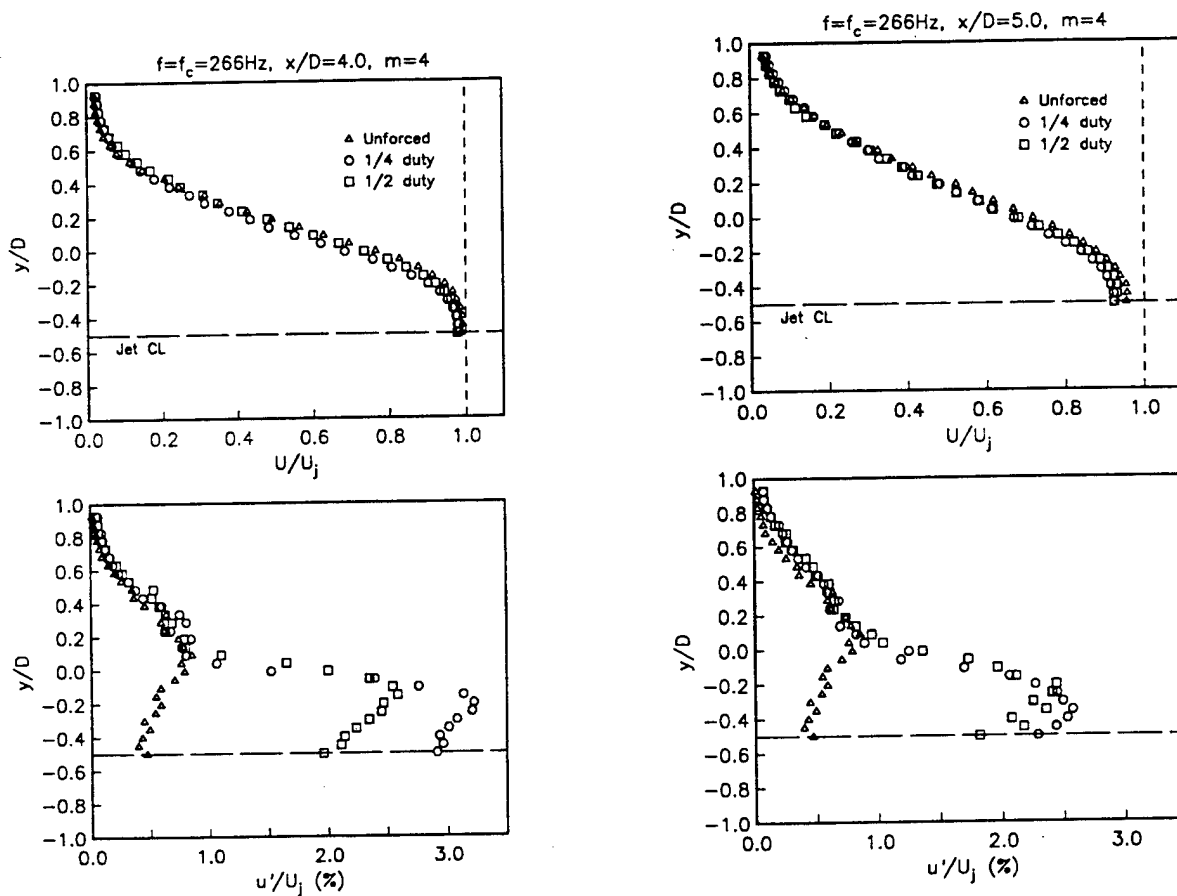


Figure 25: Mean velocity profiles (top) and eigenfunction distributions at the column mode frequency (f_c) without excitation, and with $m = 4$ excitation (two cases). $x/D = 4.0$ (left) and 5.0 (right)

result of nonlinear development since the linear eigenfunction should have a single peak. This is consistent with the streamwise distribution of the mode amplitude, which begins to saturate at $x/D = 2.0$.

The streamwise amplitude development of the excited column mode is presented in Figure 26 for all of the cases. The top part of the figure documents the streamwise development of the velocity fluctuations at the centerline. The bottom part corresponds to the development of the total streamwise fluctuation amplitude, which is found by integrating the radial distributions in the previous figures. In both figures, the upward triangles correspond to the natural (unforced) jet. The solid line indicates the linear growth rate based on the natural jet.

In all the cases, the amplitude increases as a result of the helical mode excitation. The centerline measurements at the top of Figure 26, reflect only the column mode. These show a linear growth region with approximately the same growth rate, independent of the azimuthal mode number of the forcing.

The integrated amplitudes in the bottom part of Figure 26, reflect both the column and shear layer modes. The solid line corresponds to the growth rate of the unforced jet. In this case, we observe some change in the amplification rate with azimuthal mode number. For a shear layer, where the ratio of the shear layer thickness to jet radius is small (quasi 2-D), the amplification characteristics for azimuthal mode numbers between 0 to 4 should be nearly the same. The results here support this. The higher azimuthal mode numbers, 6 and 8, have a slightly lower growth rate, which is consistent with linear theory predictions.

At the point of energy saturation, at $x/D = 2$, the $m = 4$ case reaches the highest amplitude, followed by the other lower azimuthal mode numbers. These are substantially above the amplitude of the unforced jet. At the furthest downstream location, $x/D = 5$, the rank order of azimuthal mode numbers giving the highest amplitude is the same, although the variation is less. All however exceed the unforced case.

This effect of azimuthal mode number on the centerline and radially integrated velocity fluctuation amplitudes is further demonstrated in Figure 27. The top plot shows the centerline u'/U_j level as a function of m at different x/D locations. Again this result should only be sensitive to the column mode. At the upstream locations, $x/D \leq 3$, we observe that the largest column mode amplitudes occur for $m = 0, 4$ and 8 . Further downstream, $m = 0$ and 2 are more favored, which signals a shift towards lower azimuthal mode numbers of the preferred condition.

The lower plot in Figure 27 shows the integrated u'/U_j levels as a function of m at the different x/D locations. Again this is sensitive to both the shear layer and column modes. In this case at the upstream locations, $x/D \leq 3$, the largest amplitudes occur for $m = 4$. Again, further downstream, the optimum azimuthal mode number shifts to favor lower values $m \leq 2$.

Based on this result, with regards to both the shear layer and column modes, $m = 4$, is probably the most optimum condition for the unsteady excitation.

The mean profiles indicated an effect of the excitation on the mean flow. This is better quantified in Figure 28, which documents the effect of the azimuthal mode number on the centerline mean velocity decay. For reference, the result for the unforced jet is shown as the upward triangle symbols.

At the upstream locations, the streamwise amplitude growth of the modes is linear, and there is an insignificant change in the mean flow. The centerline velocity decay occurs past

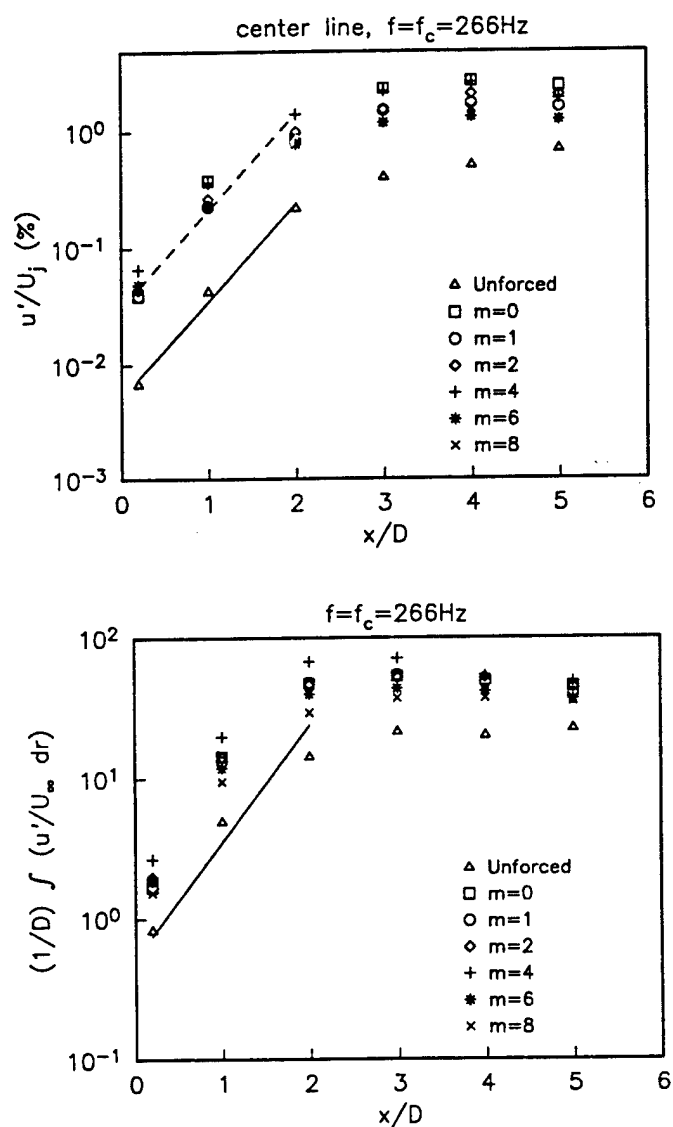


Figure 26: Streamwise development of centerline u'/U_j level (top), and of radially integrated u'/U_j level at the column mode frequency for different azimuthal mode numbers.

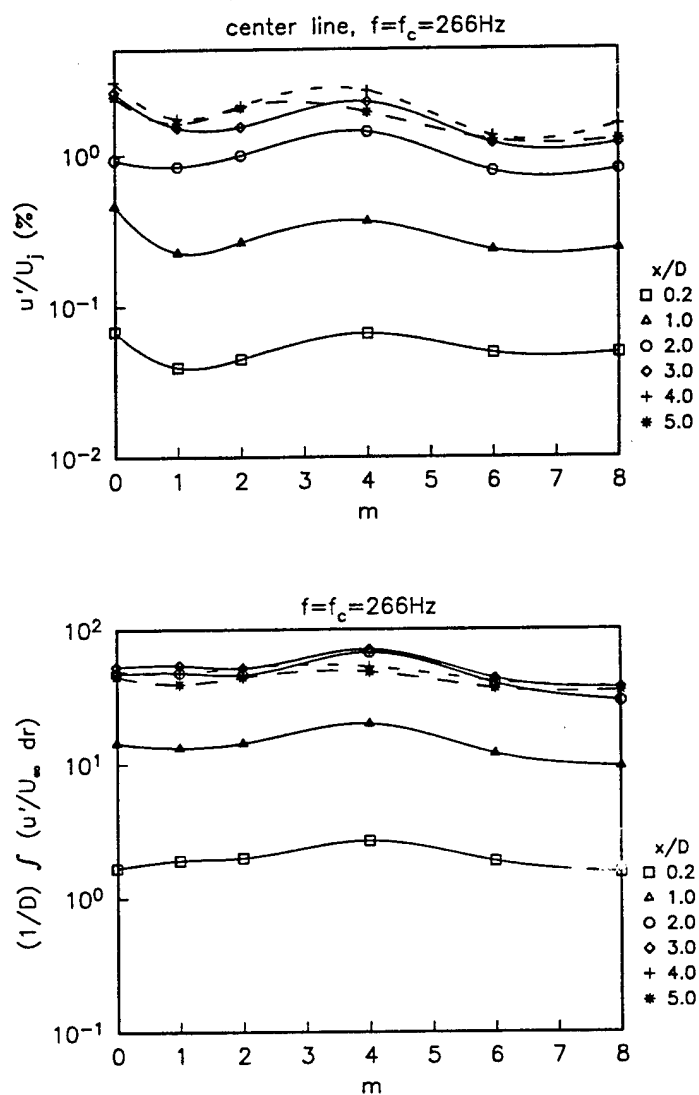


Figure 27: Centerline u'/U_j levels (top) and radially integrated u'/U_j levels (bottom) as a function azimuthal mode number, at different x/D locations.

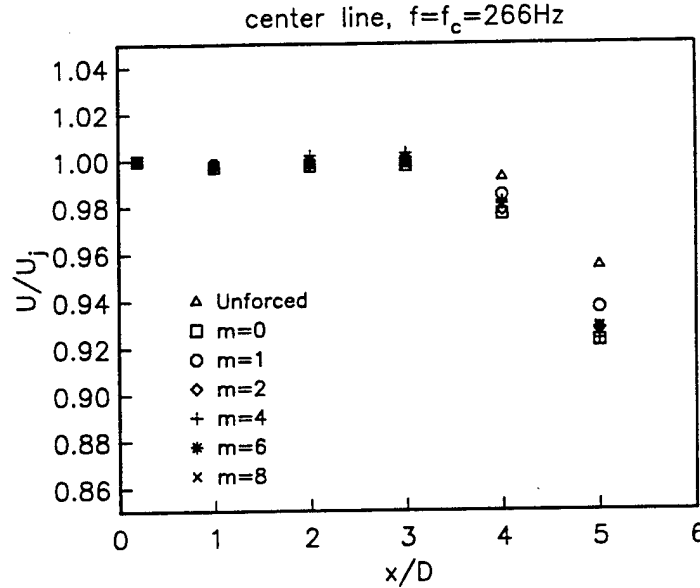


Figure 28: Streamwise development of centerline mean velocity for different azimuthal mode numbers.

$x/D = 3$. In this downstream region, all of the excitation cases are observed to result in a faster centerline velocity decay than that of the unforced jet. Most of the cases are clustered near the same value, although close inspection of the results indicates a preference towards $m = 0$ and 4. This result is consistent with the previous figure which indicated these to be two of the most preferred azimuthal mode numbers, based on fluctuation amplitude levels.

5 Conclusions

5.1 Closed-loop Coupled Mode Control

This work covered two basic elements for the control of the jet instabilities which affect mixing and acoustic generation. The first was on a method of closed-loop forcing which would couple the shear layer and jet column instability modes. This was important because the jet column mode is a global mode which influences the flow many diameters downstream of the jet exit. In contrast, the influence of the jet shear layer mode is confined to the initial region near the jet exit. However, since the most practical location for flow actuators is at the jet exit, they need to act on the shear layer if they are to benefit from natural instability amplification mechanisms. In the jet, under most circumstances, there is an order of magnitude difference in the most amplified frequency of the shear layer and column modes. The control approach

used here, generated an actuator signal which would transfer energy from the most amplified shear layer frequency to the column mode frequency through a subharmonic cascade. This proved to be very effective in coupling the two types of jet modes. The control approach had the ability to excite shear layer modes with different azimuthal mode numbers up to $m = \pm 6$. In addition, conditions which would lead to the subharmonic resonance growth of helical shear layer modes were also investigated. These experiments led to the following conclusions:

1. We found that the highest phase locking between the shear layer and column modes occurred in intervals in their frequencies where the shear layer frequency was 2, 4 and 8 times f_c . These results were representative of the full range of tested Reynolds numbers, from 30,000 to 70,000, although the preference to the 2ⁿ frequency coupling between the shear layer and column modes was more acute as the Reynolds number increased. In all the cases, the highest column mode amplitudes occurred with $n = 3$, or the shear layer frequency being 8 times the column mode frequency.
2. Adding a subharmonic helical mode to the shear layer excitation resulted in near perfect phase locking at the shear layer frequency. This however lowered the phase locking at the column mode frequency, although the effect with $m = 4$ and 3 subharmonic modes was only slightly lower than cases without the subharmonic mode added. Overall, this combination of modes did the best to phase lock all of the principle frequencies in the shear layer, and at the end of the potential core. It therefore has the best possibility to have an impact on the global properties of the jet flow many diameters downstream.
3. With regards to the shear layer spreading:
 - (a) Upstream of $x/D = 1$, all of the forced cases (open-loop and closed-loop) spread at a faster rate than the unforced jet. Also in this upstream region, the cases with the higher azimuthal mode numbers generally spread faster. This is the region where the amplitude of the shear layer modes are increasing exponentially. As a result, the shear layer spreading is nonlinear with x/D .
 - (b) For $x/D > 1$, a different pattern of development emerged. Here the highest spreading occurred for the lowest azimuthal mode numbers ($m = 0$), and the close-loop $m = \pm 6$ case actually had less spreading than the unforced jet. We note however that except for the $m = \pm 6$ case, the spreading in all of the closed-loop cases exceeded that of the open loop forced case.
 - (c) The addition of the subharmonic helical modes substantially increased the initial ($x/D \leq 1$) spreading of the shear layer. One difference with the previous cases is that with the subharmonic helical mode present, there was very little dependence of the spreading on the azimuthal mode number in the initial region.
 - (d) For $x/D > 1$, the final shear layer thickness was similar to the top plot with one exception. Here we found that rather than having one of the largest amounts of spreading, the case with $m = \pm 1$ had the lowest spreading, below that of the unforced jet. The highest shear layer thickness at $x/D = 3$ corresponded in order, to $m = 0, 2$ and 4. At this location, the shear layer thickness for the $m = \pm 6$ case was the same as the unforced jet.

4. With regards to the centerline decay:
 - (a) Overall we observed a faster centerline decay as the azimuthal mode number decreased. Except for $m = \pm 6$, the centerline decay of all of the other forced cases exceeded the unforced jet.
 - (b) Overall, the fastest centerline decay occurred with $m = 0$. This was consistent with other results which showed that far downstream, the largest shear layer spreading was for $m = 0$. However in contrast to the shear layer spreading, there was little difference between the open-loop and closed loop forcing on the centerline velocity decay.
5. For the column mode, near the jet exit, we observed a central peak on the shear layer centerline, and two higher amplitude lobes on either side of the centerline. Any of these would be ideal locations to monitor the energy in the column mode with sensors mounted close to the jet exit. In a heated jet, the location outside the centerline may be preferable since it would be further from the hotter core air (a constraint for some MEMs sensors).

5.2 Plasma Actuator Mode Control

The work with the phased plasma actuator was designed to demonstrate its ability to directly excite the column instability mode in the jet. With this, we focused on different azimuthal mode numbers in the range $0 \leq m \leq 8$. Overall it worked well, and complimented the work on the closed-loop control. These experiments led to the following conclusions:

1. With excitation, there was a significant increase in the column mode amplitude. For example, at $x/D = 2$, the peak values increased by approximately 350%. This is normally very difficult to achieve with other actuators, such as the speakers used in our closed-loop control experiments.
2. With regards to the column mode streamwise development:
 - (a) Based on the centerline u'/U_j levels which reflect only the column mode, at the upstream locations, $x/D \leq 3$, the largest column mode amplitudes occurred for $m = 0, 4$ and 8 . Further downstream, $m = 0$ and 2 were more favored, which signaled a shift towards lower azimuthal mode numbers for the preferred condition.
 - (b) Based on the radially integrated u'/U_j levels, which reflect both the shear layer and column modes, at the upstream locations, $x/D \leq 3$, the largest amplitudes occurred for $m = 4$. Further downstream, the optimum azimuthal mode number again shifted to favor lower values $m \leq 2$.
 - (c) Based on these results, with regards to both the shear layer and column modes, $m = 4$, is probably most optimum condition for the unsteady excitation.
3. With regards to the centerline decay:
 - (a) In the downstream region, $x/D \geq 3$, all of the excitation cases were observed to result in a faster centerline velocity decay than in the unforced jet.

- (b) The effect of azimuthal mode number was not too significant at $x/D = 5$, however the results did indicate a preference towards $m = 0$ and 4. This was consistent with the unsteady measurements.

6 References

- Ahn, S. 1994. Low dimensional dynamics of azimuthal modes in an axisymmetric jet with enhanced feedback. Ph.D., Illinois Institute of Technology.
- Ahuja, K & Brown, W. 1989. Shear flow control by mechanical tabs. AIAA 89-0994.
- Brown, S. 1966. Introduction to Electrical Discharges in Gases. John Wiley and Sons Publishers.
- Cavalieri, D. 1995. On the Experimental Design for Instability Analysis on a Cone at Mach 3.5 and 6 Using a Corona Discharge Perturbation Method. M.S. Thesis, Illinois Institute of Technology.
- Corke, T. C. and Cavalieri, D. 1995. Spark-generator method for introducing controlled disturbances in shear layers of high-speed jets. Interim NASA report.
- Corke, T. C. & Cavalieri, D. 1997. Controlled experiments on instabilities and transition to turbulence in supersonic boundary layers, *AIAA 97-1817*.
- Corke, T. C. and Chang, A. 1998. Mode-coupled feedback excitation in an axisymmetric jet, Physics of Fluids Annual Meeting of the American Physical Society, abstract appears in APS Bulletin.
- Corke, T. C., Cavalieri, D. & Matlis, E. 2000. Boundary layer instability on a sharp cone at Mach 3.5 with controlled input. In review *AIAA J*.
- Corke, T. & Kusek, S. 1993. Resonance in axisymmetric jets with controlled helical-mode input. *J. Fluid Mech.*, **249**, p. 307.
- Corke, T., Shakib, F. & Nagib, H. 1985. Effects of low amplitude forcing on axisymmetric jet flows. *J. Fluid Mech.*, **223**, p. 253.
- Chang, A. 1998. Mode-coupled feedback excitation in an axisymmetric jet. M.S. Thesis, Ill. Inst. Tech.
- Drubka, R. E. 1981. Instabilities in near field of turbulent jets and their dependence on initial conditions and Reynolds number. Ph.D. Thesis, Ill. Inst. of Technol.
- Gadri, R. and Roth, J. R. 1998. Glow discharge-like characteristics of a OAUGDP revealed by computer modeling. 25th IEEE International Conference on Plasma Science.
- Kanda, N., Kogoma, M., Jinno, H., Uchiyama, H. and Okazaki, S. 1991. Proc. 10th Symp. on Plasma Chem., Vol. 3, *Paper 3.2-20*.

- Kibens, V. 1981. The limit of initial shear layer influence on jet development. AIAA Paper No. 81-1960.
- Lachowicz, J., Cavalieri, D. and Corke, T. 1994. Instabilities introduced by a point source on a conical body at Mach 6. "Instability, Transition and Turbulence", Springer-Verlag.
- Mankbadi, R. 1992. Dynamics and control of coherent structure in turbulent jets. *App. Mech. Rev.*, **45**, 6, p. 219.
- Massines, F. Rabehi, A., Decomps, P. Gadri, R. Segur, F. & Mayoux, C. 1998. Experimental and theoretical study of a glow discharge at atmospheric pressure controlled by a dielectric barrier, *J. App. Physics*, **83**, 6, pp. 2950-2957.
- Meek, L. and Craigs, J. 1978. Electrical Breakdown of Gases. John Wiley and Sons Publishers.
- Nixon, D. 1994. A theory for the mixing of a compressible round jet. AIAA 94-2193.
- Roth, J. R. 1995. Industrial Plasma Engineering. Institute of Physics Publishing.
- Roth, J. R. Laroussi, M. and Liu, C. 1992. Experimental generation of a steady-state glow discharge at atmospheric pressure. Proc. 19th IEEE Int. Conf. on Plasma Sci.
- Roth, J. R., Sherman, D. & Wilkinson, S. 1998. Boundary layer flow control with one atmosphere uniform glow discharge surface plasma. *AIAA-98-0328*.
- Zaman, K. Samimy, M & Reeder, M. 1991. Effect of tabs on the evolution of an axisymmetric jet. NASA Tech. Mem. 104472.

User: corke
Host: fabian2
Class: fabian2
Job: standard_input